Atmospheric Pressure Chemical Vapor Deposition of Fluorine-Doped Tin Oxide and Tin-Germanium Oxide: Photovoltaic and Energy Storage Applications

Atmospheric Pressure Chemical Vapor Deposition of Fluorine-Doped Tin Oxide and Tin-Germanium Oxide: Photovoltaic and Energy Storage Applications

A dissertation presented

by

Lauren Ann Hartle

to

The School of Engineering and Applied Sciences

in partial fulfillment of the requirements

for the degree of

Doctor of Philosophy

in the subject of

Applied Physics

Harvard University

Cambridge, Massachusetts

April 2018

Dissertation advisor: Professor Roy Gordon Lauren Ann Hartle

Atmospheric Pressure Chemical Vapor Deposition of Fluorine-Doped Tin Oxide and Tin-Germanium Oxide: Photovoltaic and Energy Storage Applications

Abstract

This dissertation addresses renewable energy in two ways: energy storage technology that eases the integration of large-scale wind and solar power into the electric grid, and an earth-abundant solar cell layer intended to increase cell efficiency.

Flow batteries employing bromine-hydrobromic acid positive electrolytes are promising energy storage options, but the destruction of graphite flow plates by bromine limits battery lifetimes. Accordingly, atmospheric pressure chemical vapor-deposited (APCVD) SnO_2(F) protective coatings were developed to stabilize stainless steel flow plates against attack by bromine and hydrobromic acid. By varying the ratio of bromotrifluoromethane to tetramethyltin delivered during deposition, the cell resistance contribution of SnO_2(F) was minimized. The considered SnO_2(F) film was stable in heated electrolyte, with suitable resistance for flow batteries, and continuous films were achieved on sufficiently smooth substrates.

Metal nitride films were also explored as a protective flow plate coating: the considered VN, WN, and TiN films had cell resistance contributions competitive with those of SnO_2(F) and graphite, but insufficient chemical stability to bromine and/or hydrobromic acid. The chemical stability of other battery components was studied by extended exposure to heated bromine/hydrobromic acid electrolyte. Nafion proton exchange membranes showed a possible

decrease in conductivity. The dry cell resistance and appearance of carbon paper electrodes and pyrolytically sealed graphite flow plates were stable.

Finally, tin-germanium oxide alloys were evaluated as electron transport layers (ETLs) for solar cells. A $(Sn,Ge)O_2$ APCVD method was developed using tetramethyltin, tetramethylgermanium, and oxygen at nominal deposition temperatures of 475-520 °C. Up to 8 at. % germanium incorporation was achieved. Resistivity decreases with increasing germanium incorporation, due to increasing carrier concentration. Optical absorption spectra are consistent with crystalline-direct and amorphous-direct optical transitions. Optical and XRD data suggest crystalline films with a decreasing fraction of well-ordered material with increasing germanium incorporation. For the first time, the band structure of $(Sn,Ge)O_2$ is reported. Modest tuning of the conduction band position (ca. 0.6 eV) was observed at low germanium concentrations. The high carrier concentration and likely presence of defects tailing into the bandgap may preclude the use of this deposition method for $(Sn,Ge)O_2$ ETLs for all but the lowest germanium concentrations.

Table of Contents

Abstract ..... **iii**

Table of contents ..... **v**

Acknowledgements ..... **viii**

1 Fluorine-doped tin oxide as a protective coating for redox flow battery components **1**

1.1 Chapter abstract 1

1.2 Introduction 2

1.3 Materials and methods 7

1.3.1 Atmospheric pressure CVD of SnO_2(F) 7

1.3.2 Physical properties 21

1.3.3 Electrical properties 24

1.3.4 Chemical stability 31

1.4 Results and discussion 32

1.4.1 Characterization of SnO_2(F) on silicon thermal oxide substrates 33

1.4.2 Electrical properties in flow battery cells 41

1.4.3 Chemical stability 53

1.4.4 Film continuity 55

1.5 Conclusions 61

2 Stability and performance of metal nitride protective flow plate coatings and other flow battery components **67**

2.1 Chapter abstract 67

2.2 Introduction 68
2.3 Materials and methods 70
2.3.1 Deposition of metal nitride films 70
2.3.2 Dry cell resistance measurements 74
2.3.3 Physical properties of V(N,O), V(N,C), Ti(N,O), and W(N,O,C) films 75
2.3.4 Stability of V(N,O), V(N,C), Ti(N,O), and W(N,O,C) films 77
2.3.5 Flow plate, carbon electrode, and membrane stability tests 78
2.4 Results and discussion 80
2.4.1 Magnetron sputtering of Ti(N,O) and V(N,O) 80
2.4.2 Composition of considered films 84
2.4.3 Material screening by dry cell ASR 86
2.4.4 Evaluation of metal nitride stability to bromine and hydrobromic acid exposure 88
2.4.5 Stability of Entegris sealed flow plates 99
2.4.6 Carbon paper electrode stability 101
2.4.7 Membrane stability 103
2.5 Conclusions 104

3 Alloying of germanium into tin oxide by atmospheric pressure chemical vapor deposition 109
3.1 Chapter abstract 109
3.2 Introduction 110
3.3 Materials and methods 114
3.3.1 Atmospheric pressure deposition of $(Sn,Ge)O_2$ 114
3.3.2 Physical properties 116

3.3.3 Electrical properties 124

3.3.4 Band structure 126

3.4 Results and discussion 144

3.4.1 Deposition of $(Sn,Ge)O_2$ 144

3.4.2 Electrical properties 150

3.4.3 Band structure 152

3.5 Conclusions 165

Acknowledgements

My time at Harvard has been transformative personally, intellectually, and professionally in more ways than I could hope to describe in a few paragraphs. I have had the good fortune of knowing some truly remarkable people, and I will be forever grateful for that gift.

I have been privileged to work with my advisor, Prof. Roy Gordon. Scientifically speaking, his intellect, curiosity, patience, and wealth of knowledge has served as an inspiration for me. I am immensely grateful to have played a small role in fulfilling his scientific vision, which spans decades and is motivated by the desire to explore and understand, but also to advance human welfare. (After all, "there is no planet B".) Many thanks to my thesis committee (also my qualifying committee). Prof. Michael Aziz provided incisive feedback and guidance throughout my graduate career. Prof. Frans Spaepen, who taught my first materials science class (AP 282), has also lent his careful, critical eye to evaluating my work.

The Gordon group was a second home and family to me—thanks to that wonderful collection of human beings, I leave Harvard with clearer eyes, sharper wits, and many fond memories. I want to thank Ashwin, Aykut, Bobby, Christina, Dan, Emily K., Eugene, Harbing, Helen, Jun, Rachel, Tamara, Xian, and Xizhu for their help and support. I worked closely with Dr. Luke Davis for large portions of the work presented here. His support, advice, and endless, endless (endless) patience as a mentor were instrumental to my success in graduate school. I would also like to call out the women of the Gordon group: their talent astounds, their sense of whimsy and humor lightens the darkest (and most vibration-isolated) rooms. Thanks also to Teri Howard, our group's administrator, whose professionalism and efficacy are unparalleled.

My collaborators the Aziz and Aspuru-Guzik groups have been a pleasure to work with. Thanks to Dr. Diana De Porcellinis (a kind friend and membranes expert, to wit), Dr. Michael

Gerhardt (for patiently teaching me about flow battery measurements), Dr. Qing Chen (for CV advice and acid wit) Dr. Brian Huskinson (for sharing his encyclopedic knowledge of electrochemistry, catalysis, and flow battery literature when I first joined the group), Prof. Michael Marshak (for providing much needed advice), Dr. Eugene Beh (for his joie de vivre and our numerous, baroque conversations about things scientific and not), and many others. My participation in this collaboration has improved the quality of my research and enriched my Harvard experience.

I would also like to thank the staff of Harvard's Center for Nanoscale Systems. Dr. Stephan Kraemer provided invaluable assistance by performing the FIB cross-sections used in Chapter 3. Arthur McClelland and Greg Lin lent their time and expertise as I pursued the UV-Vis and XPS experiments described in this work. The reactor used in Chapter 1 and Chapter 3 was built partly from custom-machined parts produced by the excellent, and eternally cheerful machinists at the SEAS instrumentation shop. I owe Mike, John, and Al a debt of gratitude for answering my questions, and keeping me updated on the Patriots. Thanks also to the community at the Harvard University Center for the Energy and the Environment for providing a place to explore the broader implications of energy research. Outside Harvard, Dr. Ryan Thorpe of Rutgers University is gratefully acknowledged for performing the RBS measurements reported in these pages.

To my friends, near and far—thank you. AJ, Anna, Ben, Brenna, Christina, Emily R., Jocelyn, Jon, John, Naveen, Rachel, Zsofia, and so many others—the world is a brighter place with you in it.

My family has been, and will always be, a wellspring of love and support. We are separated by oceans, continents, and hundreds of miles, but in an instant, I can call to mind the explosions

of laughter, the crashing of dishes—all those warm, wonderful sounds that feel like home. I feel privileged to have shared this journey with you.

1 Fluorine-doped tin oxide as a protective coating for redox flow battery components

1.1 Chapter abstract

Flow batteries are a promising energy storage option for integrating variable renewable energy sources, like wind and solar, into the electric grid. Flow batteries using bromine-hydrobromic acid positive electrolytes have shown high power densities,[1] but the destruction of graphite flow plates by bromine limits the working lifetime of these devices. Accordingly, atmospheric pressure chemical vapor-deposited SnO_2(F) protective coatings were developed to stabilize stainless steel flow plates against chemical attack by bromine and hydrobromic acid. SnO_2(F) is an n-type semiconductor whose carrier concentration can be tuned by fluorine doping. By varying the delivery rate of the dopant source, bromotrifluoromethane, the protective layer's resistance in a mock "dry cell" test assembly was minimized. Films of SnO_2 and SnO_2(F) were immersed in aqueous electrolyte (3 M hydrobromic acid and 1.5 M bromine) held at 58 °C for over two months. The cell resistance contribution and chemical stability are assessed and found to be suitable for flow battery applications. The films were found to be continuous on silicon thermal oxide substrates, but when deposited on stainless steel, etching experiments revealed pinholes in the films. The lack of film continuity is thought to be due to excess surface roughness—potential solutions are briefly examined.

1.2 Introduction

Growing academic and commercial interest in energy storage technology stems in part from the need to smooth power output from variable renewable energy sources like wind and solar energy.[2] Renewable energy comprised two-thirds of new power capacity in 2016, and the IEA predicts that solar, followed by wind energy, will be the dominant renewable energy source by 2022.[3] If this trend continues, current issues with variability of these sources will be magnified. Efficient, inexpensive energy storage technology offers the potential to utilize the full capacity (energy output) of solar and wind installations and maintain grid reliability while achieving a lower carbon emissions rate than dispatchable fossil fuel-based alternatives. The analysis of the United States Department of Energy places the desired cost for a scalable energy storage technology at $100/kWh.[4] Existing energy storage technologies (e.g., pumped hydroelectric storage, compressed air storage, and lithium-ion batteries,) face a number of obstacles to commercialization and widespread implementation, including expensive components, a lack of scalability, or geographic restrictions.[5] Flow batteries are a promising energy storage alternative—with high efficiencies, flexible siting, and scalability.[2]

Figure 1.2.1 shows a schematic of a flow battery. The electolytes are anthraquinone and bromine/hydrobromic acid—chemistries addressed by this work. On each side of the flow battery, liquid electrolyte is pumped into the main unit (called the cell in this work), and is guided by channels to flow or diffuse through a porous electrode before exiting the unit through the flow channels. The two sides are in physical contact, separated by a proton-exchange membrane. During charging in this configuration, a potential is applied to the electrodes via the flow plates, and an electrochemical reaction occurs on each side, and a two-electron/two-proton pair is consumed by the oxidation of anthraquinone disulfonate on one side, and produced by the reduction of bromine

on the other. During discharge, these reactions are reversed. Electrolyte is stored in tanks external to the main unit. Because the electrically active material is stored externally to the electrodes, it is possible to optimize the energy and power capacity independently.

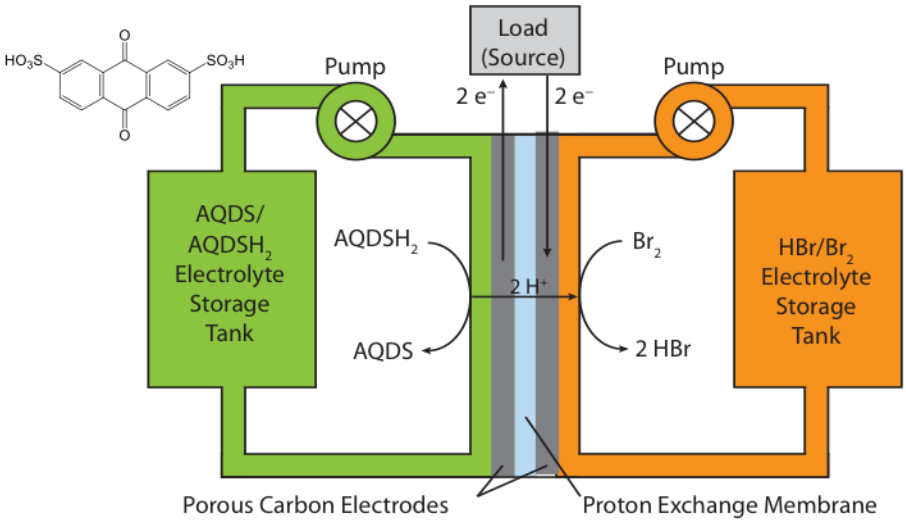

Figure 1.2.1: Organic-Halogen flow battery featuring bromine and hydrobromic acid negative electrolyte. Figure reproduced with permission from Huskinson, B., Marshak, M. P., et al. (2014).[6]

Commercial flow batteries use predominantly vanadium oxide electrolyte, but electrolyte costs must be reduced substantially to the expansion of such technology.[7] To that end, a collaboration between Prof. Aziz, Gordon, and Aspuru-Guzik and researchers at Sustainable Innovations was established to develop inexpensive, efficient flow battery chemistry and designs.[1, 6, 8-14] The chemistry shown in Figure 1.2.1 was a result of these efforts. Bromine-hydrobromic acid electrolytes are inexpensive, require no catalyst, and flow batteries combining this chemistry with organic negative electrolytes have achieved power densities of ca. 1 W/m^2—competitive with vanadium-based batteries.[1]

Challenges remain in achieving long lifetimes for bromine-based flow batteries. As one of the few materials that are electrically conductive and relatively chemically resistant, graphite

electrodes and flowplates (shown in Figure 1.2.2) are commercially available and in widespread use for flow batteries. However, bromine-based chemistries are particularly destructive to graphite; the process of bromine intercalation into graphite[15, 16] can cause swelling, fracture, and pulverization of exposed parts. In fact, an aqueous solution of bromine can be used to facilitate exfoliation of graphene sheets from bulk graphite.[17] We have observed cracking and degradation of graphite flow plates after a few months of daily use in a research setting. Replacing graphite plates is a challenge: bromine-resistant materials are typically poor conductors, such as fluorocarbon polymers. One potential solution is to coat a convenient substrate with a chemically-resistant, conductive coating. Stainless steel is inexpensive, widely available, and can be machined or stamped with custom flow channel designs.[18] The latter fabrication method is amenable to industrial-scale production.

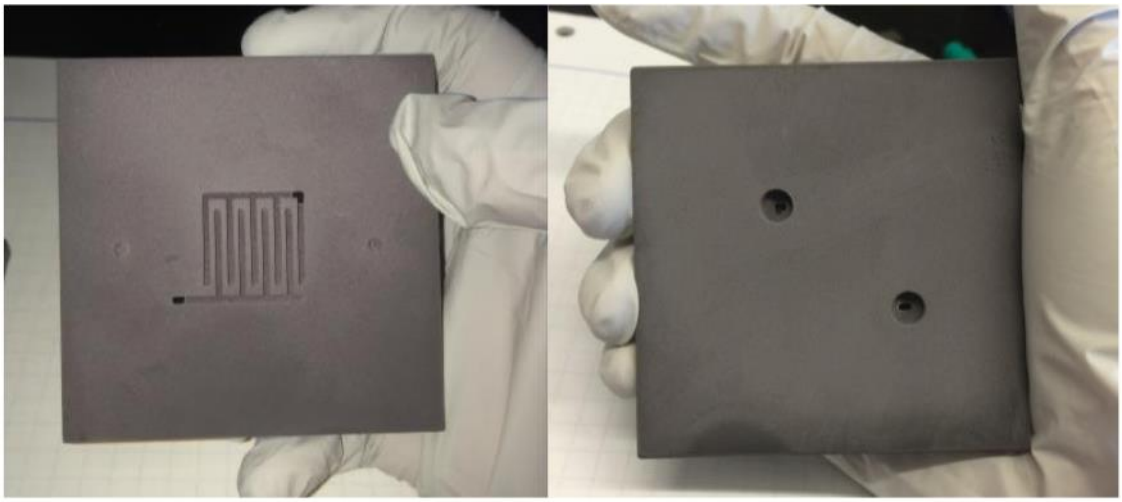

Figure 1.2.2: The fluid-facing front side of an interdigitated graphite flow plate and the back side, with fluid inlets and outlets visible. Image provided by Dr. Michael Gerhardt.

A suitable protective coating must have low contact resistance, continuous surface coverage, and adequate corrosion resistance. Since bromine and hydrobromic acid are essentially confined to the posolyte side of the battery, plates need not be taken to reducing potentials.

Tantalum nitride coatings are commercially available[i] and nominally resistant to bromine, but were found to be are highly resistive in a cell, likely due to a surface oxide layer. Other metal nitrides, e.g. VN or TiN, are promising and generally considered chemically resistant; Chapter 2 will address these materials. Here, to combat highly oxidizing conditions, a stable, conductive metal oxide coating was selected. Fluorine-doped tin oxide, $SnO_2(F)$, is an n-type semiconductor that is inert to highly oxidizing and acidic solutions. The addition of fluorine reduces film resistivity by increasing the carrier concentration, and might reasonably be expected to reduce the contact resistance between the protective coating and the adjacent interfaces of the flow battery cell. Indeed, Park, et al. showed $SnO_2(F)$ deposited by electron cyclotron resonance-metal organic chemical vapor deposition (ECR-MOCVD) with tetramethyltin and sulfur hexafluoride to be a suitable protective coating for bipolar plates in fuel cells.[19]

$SnO_2(F)$ is prized as a top-surface current collector in solar cell applications; its advantages include high transparency, high conductivity, and ease of fabrication. Nanostructured morphologies have found use in sensing technology for gases such as ammonia, oxygen, carbon dioxide, and nitrogen dioxide.[20] $SnO_2(F)$ coatings are also used in displays and energy efficient windows[21]. $SnO_2(F)$ can be deposited by numerous methods: sol-gel,[22] sputtering, atomic layer deposition (ALD), atmospheric-[23-28] and low-pressure[19, 27, 29] chemical vapor deposition (CVD), electron beam evaporation,[30] and spray-pyrolysis[31-35]. Atmospheric pressure chemical vapor deposition (APCVD) of $SnO_2(F)$ can be seamlessly incorporated into a well-established deposition process used to coat millions of square meters of float glass per year.[36] This process was built on a method and chemistry similar to one outlined by Proscia and

[i] Please see Tantaline (https://tantaline.com/)

Gordon.[23] The latter method allows growth rates of up to 60 nm/min and affords resistivities as low as 10^{-3} Ω·cm with carrier concentrations up to 10^{20} cm^{-3}. CVD is also better-suited than PVD or spray pyrolysis to coating structured surfaces like flow battery electrodes and plates. Pure oxygen, ca. 1 % tetramethyltin vapor in nitrogen, bromotrifluoromethane, and purified nitrogen flow over a heated substrate, reacting in the gas phase and at the substrate surface to produce a high-quality, fluorine-doped tin oxide film. Bromotrifluoromethane was used as a fluorine source to tune the contact resistance of the tin oxide films. Essentially, the Sn-C bonds in tetramethyltin are cleaved, generating methyl and trimethyltin radicals that generate CF_3 radicals from bromotrifluoromethane ($BrCF_3$) and initiating a series of branching free radical gas phase reactions which incorporate oxygen.[37] The growth rate is driven in part by intermediate gas phase reactions. The flowrates of these gases can be adjusted to change the resulting film (e.g., morphology, contact resistance, deposition rate).

Thin films of SnO_2(F) were deposited by APCVD on silicon thermal oxide and stainless steel substrates. Films were pinhole-free on thermal oxide, and showed resistivity values consistent with literature. A SnO_2(F) film on silicon thermal oxide was stable to heated electrolyte exposure for over two months, though neat SnO_2 showed signs of degradation. By increasing the bromotrifluoromethane delivery rate, the dry cell resistance of different samples—a proxy for the contact resistance of the protective coating—was reduced from 2.5 Ω to 46 mΩ. The choice of carbon paper electrode increased the measured dry cell resistance by up to 8-fold, and increased the measurement error by up to a factor of 10. While electrolyte-stable, pinhole-free SnO_2(F) films were successfully deposited on silicon thermal oxide, continuous films on stainless steel substrates were not achieved. Surface roughness played a crucial role: SS surfaces that were smoothed by the machining process allowed coatings few to no pinholes, while surfaces that were made rougher

had many pinholes.

1.3 Materials and methods

1.3.1 Atmospheric pressure CVD of SnO_2(F)

Figure 1.3.1 shows a schematic of the atmospheric pressure CVD SnO_2(F) system. For the purposes of this discussion, the system can be divided into three parts: reagent sources, flow

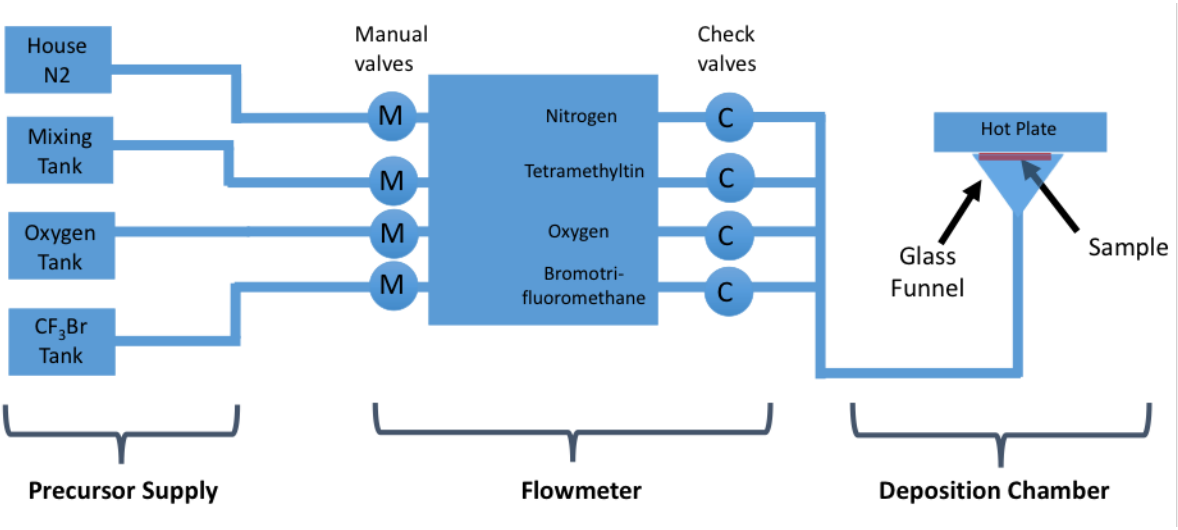

Figure 1.3.1: Schematic of atmospheric pressure chemical vapor deposition system for SnO_2 and SnO_2(F). All tanks include dual or single-stage regulators to control source pressure.

controllers plus mixing lines, and the deposition chamber. Reagent sources are nitrogen (house supply from liquid boil-off, oxygen and water removed by an Entegris inert gas purifier, model no. CE500KFI4RR, delivery pressure 7 psig), oxygen (Airgas, USP, delivery pressure 7 psig), bromotrifluoromethane (Pfaltz & Bauer, 99 %, delivery pressure 7 psig), and tetramethyltin (varying mol % in nitrogen, delivery pressure 7 psig). All gas lines pass through flow controllers (Matheson R7400, tube cube 610A/910A for TMT and CF_3Br, and tube cube 602 for oxygen and nitrogen) which regulate the reactant gas composition and flowrate. Check valves (Cambridge Valve and Fittings, 1/3 psig cracking pressure) downstream from the flow controllers reduce back

flow of gas during deposition. All gas lines combine in a series of tees, flowing through stainless steel tubing to the deposition chamber. The latter consists of a glass funnel which guides gas over the surface of a substrate heated by an inverted hotplate. Unreacted gas and by-products exhaust through the space between the funnel and sample holder. All components from the flow controllers to the deposition chamber are enclosed in a fume hood. All lines, valves, and machined parts are 316 stainless steel unless otherwise noted.

Tetramethyltin (TMT, Aldrich, 98%) was diluted in purified nitrogen before use. While it is possible to source this CVD reaction by drawing vapor from a reservoir of liquid TMT, we chose to utilize a pre-diluted, gaseous mixture for its enhanced reproducibility and control of delivery. TMT was loaded into a syringe or an evacuated stainless steel bubbler in a fume hood, and introduced into an evacuated gas cylinder that had been baked at 80 °C under vacuum overnight. The cylinder was then pressurized to 25 psig with purified nitrogen, closed, and the bottom wrapped with heating tape and held at 80 °C overnight to encourage convective mixing. Once cool, the cylinder was connected to the flowmeters. When the cylinder pressure dropped below 7 psig due to use, the tank was re-pressurized with purified nitrogen to reach 15–25 psig, then again convectively mixed overnight. The new concentration was calculated by determining the dilution factor upon re-pressurizing. Note that TMT is highly toxic and volatile, and great care should be taken in handling it, even in dilute form.

Gas flow for each reagent is regulated by a flow controller consisting of an inlet valve and a flow meter tube, which reads the flow rate in the line. The flow tubes are calibrated for nitrogen gas at 0 psig, hence use with other gases and/or at other pressures requires correction factors for gas density and pressure. In this system, the bulk of the pressure drop occurs at the flowmeter valves, which are upstream from the flow tubes. Therefore, the pressure in the flow tubes should

be at or near 0 psig.[ii] This assumption is supported by tests over the full range of operating flow rates and pressures; in all cases, a pressure reading of 0.0 psig was obtained at the intersection of the gas lines immediately after the check valves (see Figure 1.3.1). Thus, no pressure correction factor was needed. The density correction factor can be calculated as per equation 1.3.1,

$$Q_{gas} = Q_{N_2}\sqrt{\frac{\rho_{N_2}}{\rho_{gas}}} \qquad [1.3.1]$$

where Q_{gas} and Q_{N_2} indicate the volumetric flow rate, in sccm, of the gas to be calibrated and nitrogen, respectively. The densities of the two gases are represented by ρ_{N_2} and ρ_{gas}. For a mixed gas, e.g. 1.1 mol % tetramethyltin in nitrogen, the molar concentration of that gas can be used to calculate the appropriate mixed gas density, as shown in equation 1.3.2 below.

$$Q_{mix} = Q_{N_2}\sqrt{\frac{\rho_{N_2}}{\rho_{gas}C_{gas}+(1-C_{gas})\rho_{N_2}}} \qquad [1.3.2]$$

The accuracy of the gas flow controllers is ±5 % of full scale, or ±20 sccm nitrogen for tube 602 (used for oxygen and nitrogen), and ±5.4 sccm nitrogen for tube 610A (used for tetramethyltin and bromotrifluoromethane). To ascertain the variability for the delivery of particular reagent, a density correction (described above) must be used. The repeatability, or run-to-run error of gas delivery, is 0.25 % of the scale reading, according to supplier specifications. Thus nominally identical tubes can vary substantially in output for the same flowmeter reading, but if a flow tube is used consistently for the same gas, depositions ought to be directly comparable. In this work, samples are only compared when the same set of flow tubes was used. In instances

[ii] The check valves downstream from the flowmeter have a cracking pressure of 1/3 psig, and hence are expected to have a minimal effect on downstream pressure. An interpolation of Matheson's provided delivery pressure calibration predicts a difference of 1%, which is dwarfed by the absolute tube accuracy.

where a flow tube has been changed, it is noted in the text and relevant figure caption.

The deposition chamber, depicted in Figure 1.3.2, is consists of a glass funnel (short stem, 150 mm diameter funnel with beveled tip removed, Sigma Aldrich, BR145550) connected at the narrow end to a stainless steel gas port with ultra-torr fittings (Cambridge Valve and Fittings), and

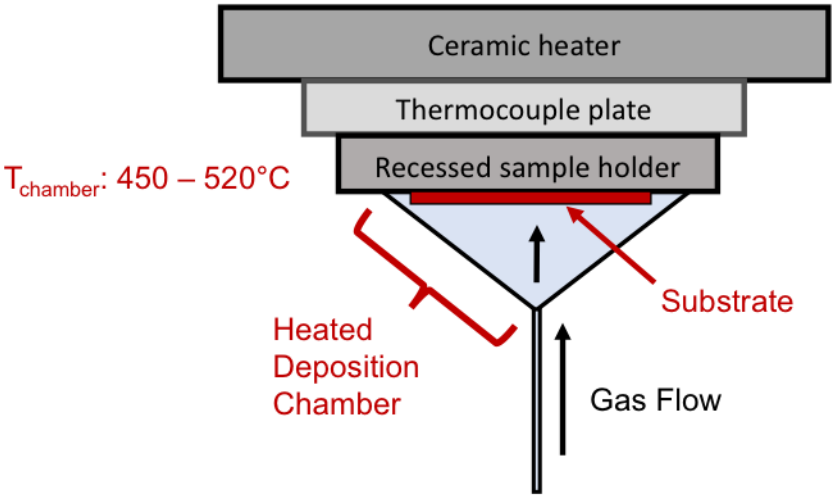

Figure 1.3.2: Side view of deposition chamber

clamped at the wide end to the sample holder (SS 316, in-house fabrication) and hot plate (Corning, model no. PC 420) by a stainless steel collar. A flexible stainless steel hose connects the combined reagent tubing to the deposition chamber line—this addition permits sample loading and unloading without disassembling the tubing. The funnel remains upside-down during deposition; placing the heater at the top of the chamber avoids the formation of convection currents between the heated surface and cooler funnel wall. If powder is produced during a reaction, it typically drops to the funnel walls and remains there, rather than contaminating the sample surface.

Figure 1.3.3 shows a schematic of the collar and funnel assembly. The collar is clamped around the funnel and attached to the sample holder with stainless steel screws.

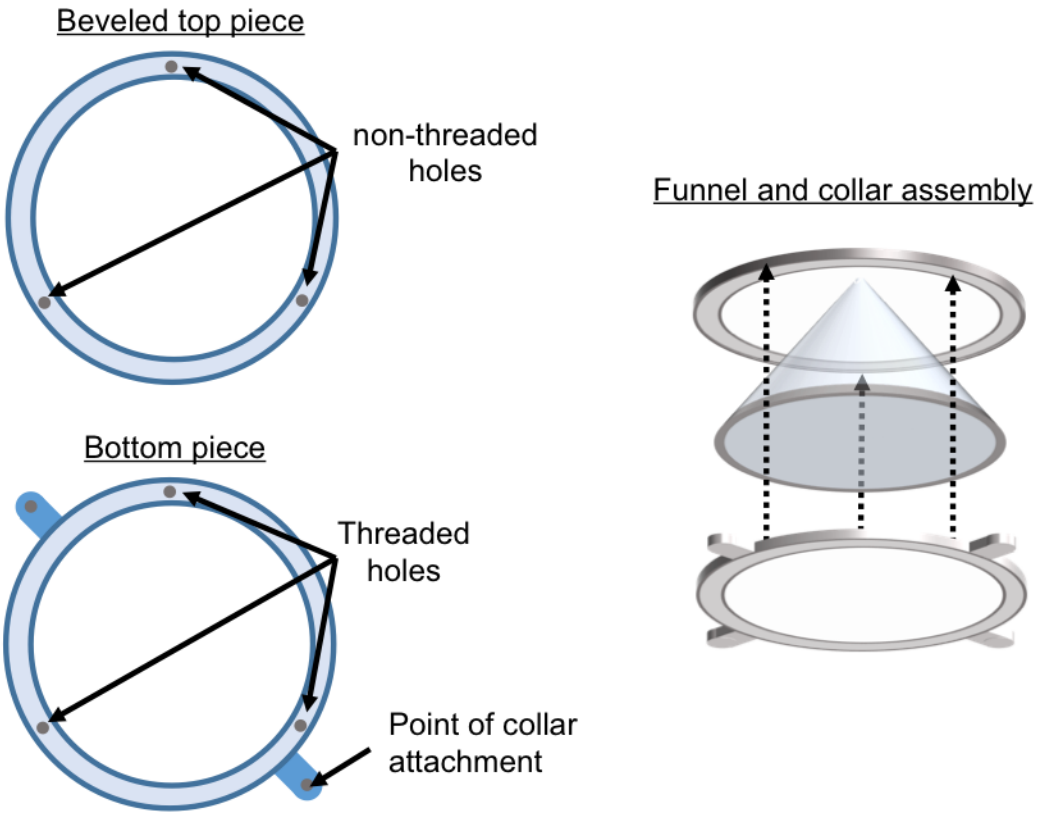

Figure 1.3.3: Plan and 3-D view of funnel and collar

A benefit of this reactor configuration is the capacity to deposit on large samples: maximum substrate sizes are 3″ × 3″ for stainless steel plates up to half an inch thick, and 4″ × 4″ for thin (i.e., ca. 1 mm) samples. To secure a stainless steel substrate (typically 3″ × 3″ × 0.5″) for deposition, the piece is dropped into a 3″ × 3″ slot in the recessed sample holder, and held in place by three set screws. This set-up is pictured in Figure 1.3.4. For samples thinner than 0.5″, a 3″ × 3″ stainless steel plate can be placed underneath the substrate to bring the surface flush with the sample holder.

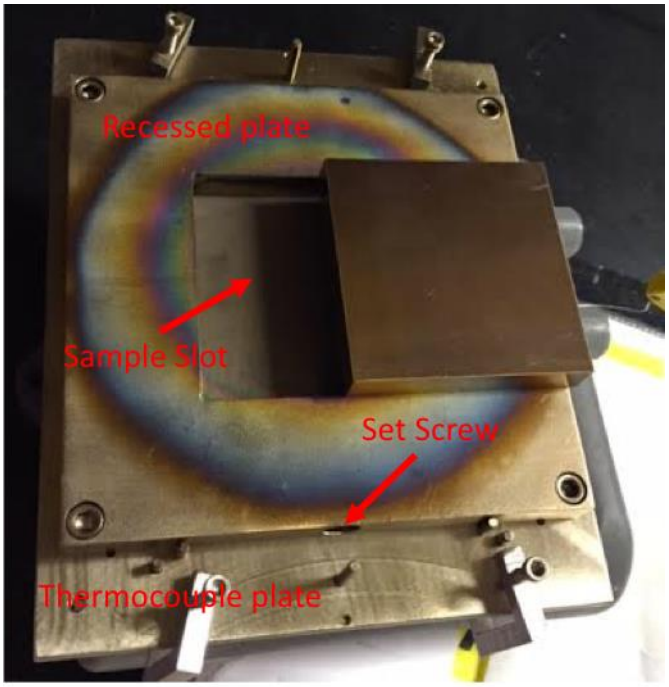

Figure 1.3.4: Loading of a stainless steel substrate. A label indicates one of the three set screws which hold the sample in place.

Thin substrates are held in place by vacuum, as shown in Figure 1.3.5 and Figure 1.3.6. A custom-made 316 stainless steel vacuum chuck is dropped into the sample slot and a threaded stainless steel vacuum line fitting is connected directly to the chuck through a hole in the side of the sample plate. This hole is blocked by a threaded bolt for depositions on stainless steel. Three set screws are used to hold the vacuum chuck in place during deposition. The vacuum chuck has four drilled holes connecting those locations on the chuck surface to the vacuum line, allowing up to four thin substrates to be supported simultaneously. Clips were initially used to attach thin samples, but they were found to disrupt gas flow patterns, causing powder accumulation and negatively affecting sample uniformity.

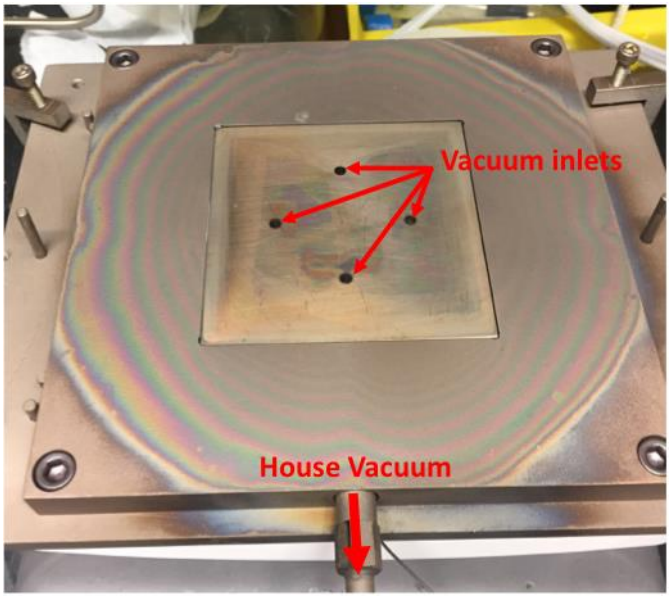

Figure 1.3.5: Vacuum chuck and sample holder. Labels indicate the points where samples can be attached by vacuum. Larger samples can use all available vacuum inlets.

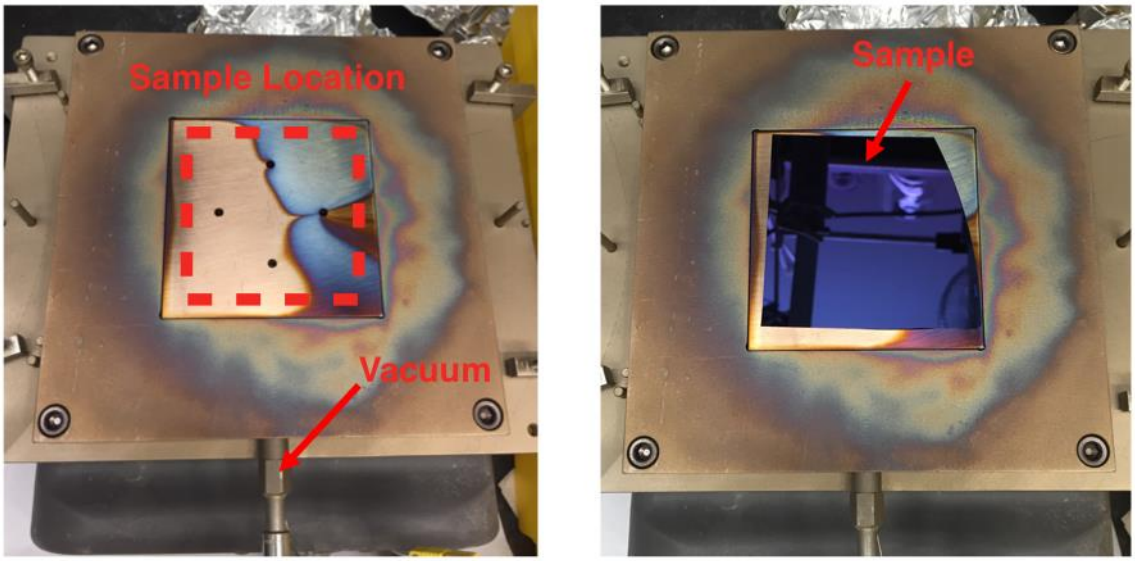

Figure 1.3.6: Loading of a thin sample, e.g., a silicon thermal oxide wafer piece.

A note on lubricants: high temperatures can negatively affect threaded connections, particularly those which must be undone and redone. High temperature lubricants (e.g., SAF-T-EZE anti-seize paste) solve the seizing problem, but volatilize in the chamber, causing extensive areas of retarded or erratic film growth. Instead, threads were made to a wider tolerance (i.e.,

looser), and holes were re-tapped as needed.

The nominal deposition temperature (typically 420–520 °C) is measured by a k-type thermocouple (Omega Engineering, Super OMEGACLAD® Grounded Thermocouple Probe, 6″ length, 1/32″ diameter, part no. KMQXL-032G-6) embedded in a machined groove on the side of the thermocouple plate facing the heater. The large thermal mass of the thermocouple and recessed plates are expected to reduce temperature fluctuations. It was not possible to measure the temperature of the substrate directly during deposition, but a thermocouple in physical contact with a dummy substrate during a simulated deposition (heating with nitrogen flow, but no reactant gas flow). Between 490 and 510 °C, the substrate surface was on average 89 ± 1 °C lower than the sample holder thermocouple reading. Temperatures reported in this work are uncorrected thermocouple readings from the sample holder.

Substrates included a) 316 stainless steel, precision ground 3″ × 3″ plates with a thickness of 0.5″ or 0.25″ (part no. 8896K133 or 8896K131 from TCI America via McMaster-Carr), b) 300 nm silicon oxide on (100) silicon wafers (University Wafers, made by wet oxidation), or c) quartz (GE 124 grade, Chemglass, CGQ-0640-03 and -01, 1″ square and 1″ × 3″ pieces). Unless otherwise noted, stainless steel pieces had a standard precision ground surface. Thick pieces of stainless steel (i.e., 0.25–0.5″) are preferable, as some thinner pieces warp substantially during heating. These substrates were cleaned before deposition by sonicating for 30 minutes in toluene (BDH, ACS grade), isopropanol (BDH, ACS grade), acetone (semiconductor grade, 99 %), and finally isopropanol (semiconductor grade, 99 %). Upon removal from the final isopropanol bath, the pieces were rinsed with semiconductor grade isopropanol, dried with nitrogen and immediately loaded into the deposition chamber and placed under nitrogen purge. Wafer and quartz substrates were rinsed in semiconductor grade acetone, and immediately rinsed with semiconductor grade

isopropanol, allowing no drying to occur in between. Isopropanol was removed from the substrate surface with nitrogen.

A typical deposition procedure is as follows: substrates were cleaned as detailed above, immediately loaded into the sample chamber and put under nitrogen purge. The heater was turned on, and the system was heated under nitrogen to the deposition temperature, typically 450–520 °C. When the thermocouple read the desired temperature, the system was left to further equilibrate for at least 20 minutes. The total heating time was typically 2-3 hours. Upon heating, the color of the stainless steel substrates took on a golden cast. When unpurified house nitrogen was used, this color change was far more intense, and was associated with a larger resistance change from unheated stainless steel. Hence, only purified nitrogen was used to purge the deposition chamber.

After the desired temperature was achieved, the reactant gases were rapidly adjusted (in less than 30 to 60 seconds) to the appropriate relative and absolute flow rates, targeting a total flowrate of ca. 100 sccm, unless otherwise noted. The deposition time was marked as beginning as soon as the gas streams were turned on. The system temperature was monitored and adjusted during the deposition, and kept to ±2 °C unless otherwise noted. The deposition was ended by shutting off the reagent gas streams and increasing the nitrogen flow rate to 400+ sccm.

Depositions in a system of this geometry, in which the gas flux begins perpendicular to the substrate, are distinct in appearance from those in tubular reactors in which the gas flux begins parallel to the substrate. The latter depositions are often more or less uniform perpendicular to gas flow and vary in properties along the axis of the tube. It is common in a CVD reaction to see thickness, and sometimes composition, change between the reactor inlet to outlet. If gas phase reactions, or substantial heating of the reactants, must occur before surface reactions deposit film, as is the case with the TMT reaction,[23] inlet films might be thinner than outlet films (particularly

at the lower end of the deposition temperature range). If reactions are rapid, or reagent concentrations low, certain reactants might be depleted towards the outlet, resulting in thinner films. The latter type of thickness gradient may also be associated with a compositional gradient.

Since this system cannot be modeled as simple one-dimensional gas flow, the resulting deposition patterns must be interpreted with caution. The system in this work has nominally radially symmetric gas flow, which might be expected to produce radially symmetric depositions, with a reduction in growth rate from the center to the edge. This is generally true; the concentric interference fringes displayed in Figure 1.3.7 indicate decreasing thickness with distance from the center of deposition. However, this funnel configuration introduces some sources of deposition variability that do not exist in typical tube configurations.

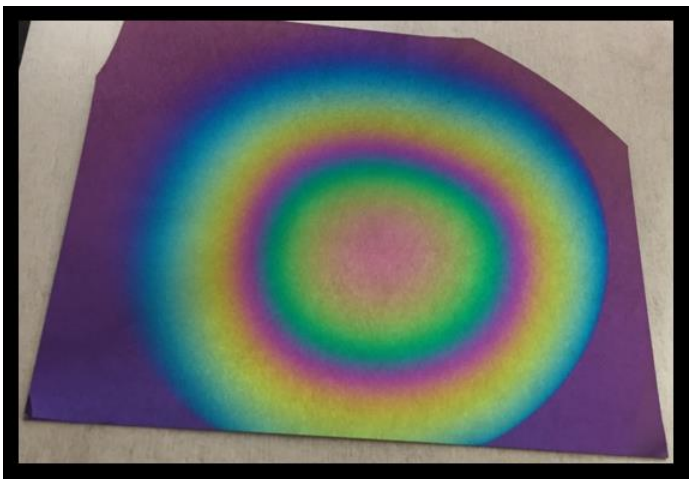

Figure 1.3.7: A example deposition on a 300-nm SiO_2 atop a ca. 6" × 6" (100) Si wafer piece. The edges of deposition match the funnel collar edges.

Unlike a flow-by tube reactor, the gas flow rate is not constant across the deposition chamber, for geometric reasons. Moving outward from the center of the sample, the increasing constriction of the funnel tends to increase the total flow rate. Simultaneously, the increasing perimeter tends to decrease the total flow rate by a factor of $2\pi r$, where r is the distance from the center of deposition. Depending on the balance of these two opposing trends, one might expect a

decrease, increase, or a transition in regimes in the growth rate moving from deposition center to edge. Higher thickness at the edge has never been observed in SnO_2 or SnO_2(F) deposition in this reactor, suggesting that funnel-related flow constriction does not dominate other factors. Furthermore, doubling the total flow rate (described in the Results section) produced no change in growth rate away from the very center of the deposition. Hence, reactions at the surface do not appear to be significantly affected by flow rate outside of the very center region.

Subtle variation in the positioning of the funnel and collar can lead to somewhat peculiar deposition patterns. Disentangling of these effects is possible with larger substrates that permit visualization of the deposition process across the entire chamber. Accordingly, substrates of at least 6″ × 6″ were used to perform neat SnO_2 depositions at 450 °C.[iii] One effect that is easily visualized by larger depositions is the influence of funnel and collar position on the deposition pattern. The location of the deposition center is mobile and subject to variations in funnel tilt and gaps between the funnel collar and the sample holder. This reactor exhausts through the space between the funnel collar and the sample holder. Therefore, if the funnel is in even contact over the entire perimeter, the resistance to flow should be equal around the funnel perimeter, resulting in a symmetric deposition. A subtle tilt of the funnel (leaving a gap of less than 0.5 mm) can drive gas flow preferentially out of this "open" side of the funnel, shifting the center of the deposition. Figure 1.3.7 shows the result of a very slightly tilted funnel. The deposition edge is sharp where contact with the substrate is firm, and the deposition center shifts slightly towards the sharp edge. A higher growth rate in this region is consistent with slower-moving gas that is briefly trapped due to the lack of a nearby exhaust path. The edge is more diffuse in the region adjacent to where the

[iii] 5.7 μmol/min TMT, 780 μmol/min oxygen, with a balance of nitrogen to reach ca. 100 sccm.

funnel and substrate are separated. Deposition is slower in this region here because the gas velocity is higher closer to the gap. The tilt in the funnel creates a smooth variation in the amount of resistance to gas escape, hence, the deposition edges in this sample vary relatively smoothly from sharp to diffuse.

If a sufficiently large localized gap in the funnel occurs, the local increase in gas velocity can distort the deposition, resulting in a wedge of higher growth rate upstream from the gap. Figure 1.3.8 illustrates such a gap. In an earlier iteration of this reactor, the funnel was sized to match one

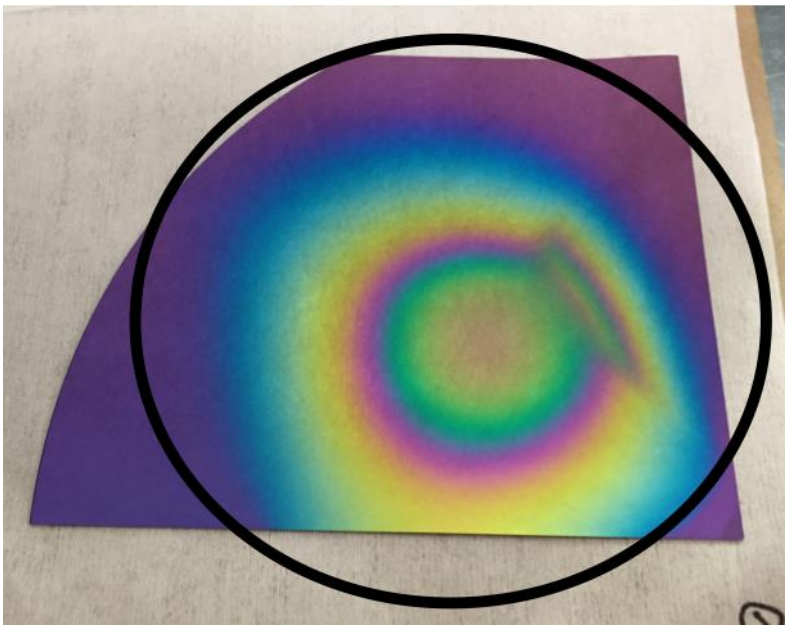

Figure 1.3.8: Deposition illustrating the impact of a large, localized gap. The black line marks the position of the funnel during deposition.

dimension of the heating plate, but the collar protruded slightly over the edge.[iv] As a result, the funnel-substrate gap visible at the bottom of the image resulted in much less flow disruption than the gap on the right side, where the sample holder ended before the funnel collar. In both cases,

[iv] The other dimension was sufficiently large to allow a half an inch to an inch on either side of the collar.

the gap is sufficiently large to pull the entire gas flow towards it. On the right side, the undersized sample holder created a sufficiently large and localized change in the gap that a step-change in thickness is visible in the interference fringes.

Awareness of these patterns is important to avoid more dramatic flow pattern changes from multiple gaps. In Figure 1.3.9, the center of deposition was pulled towards the largest gaps at the bottom of the image, and elongated to an almond shape due to competition between the smaller

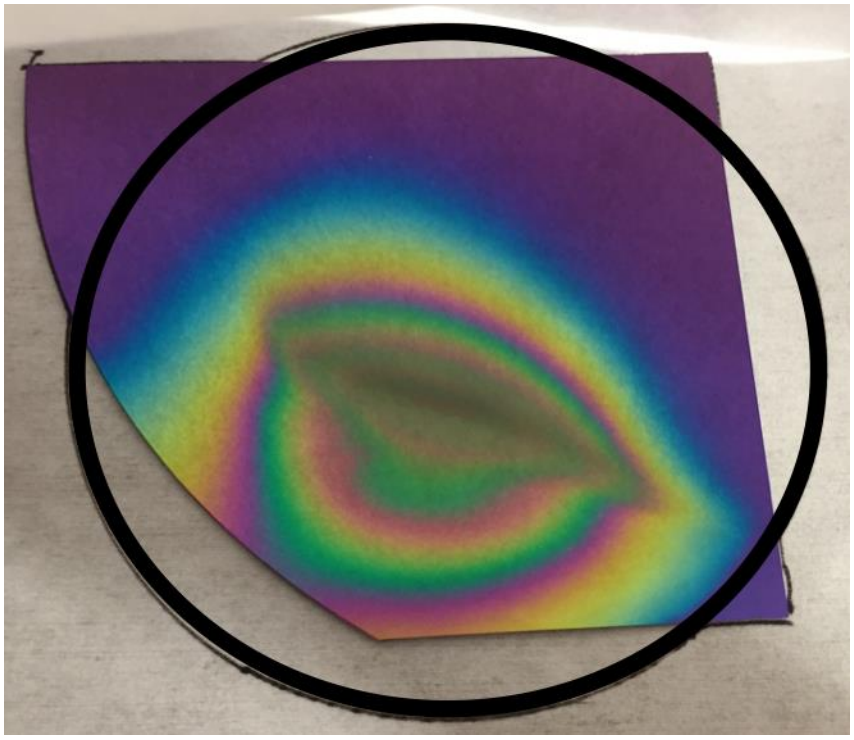

Figure 1.3.9: A deposition pattern resulting from multiple ca. 0.5 mm gaps between the funnel and substrate

gaps on the top and right and the larger gaps on the bottom and left. The deposition edges are diffuse over most of the pattern, save a sharp edge marking a small area of contact at the bottom right.

Combining the observations from Figure 1.3.7 through Figure 1.3.9, it appears that the shifts due to gaps represent potentially extreme (i.e., more than 2×) changes in flow rate, but that the impacted regions are outside the typical region of interest (ca. 3″ × 3″) for depositions. The

region of interest can still be influenced by shifts in the center of deposition. To that end, run-to-run variability was reduced by bolting the funnel and collar to the sample holder during depositions. The other effects were controlled by installing a larger sample holder plate, and ensuring that substrates fit inside the funnel collar. It was not possible to fully eliminate the shift in the deposition center—the addition of channels to the funnel collar or other methods of controlling gas exhaust may further reduce this effect.

As a final note on deposition repeatability, the anti-seize paste initially used in the threads of the sample holder, and sample clips (in an earlier iteration of the reactor) severely disrupted film deposition. It is thought that some component of the paste volatilizes as the reactor is heated, and this vapor interferes with gas phase and/or surface reactions. The roughening observed at elevated $BrCF_3$ delivery rates is observed at much lower $BrCF_3$ concentrations, including occasionally in neat SnO_2 depositions. Additionally, surface particles with surrounding regions of dramatically different film morphology are observed. If anti-seize paste is cleaned off the funnel, collar, and sample holder plates, non-reactive contaminated particles are still occasionally observed. These are often coated by CVD reactions, as shown in Figure 1.3.10 a. When anti-seize paste is re-introduced to the threads of the system, a new contaminant morphology appears: a region of thin, smooth film surrounds the particle in question, and the film is rough elsewhere. When the system is cleaned again, these particles are no longer observed. The sample holder adjustments described above avoid the need for anti-seize paste.

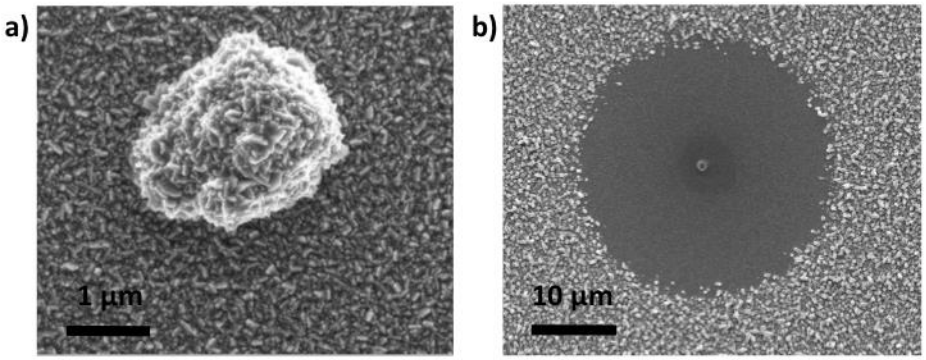

Figure 1.3.10: Example film contaminant before (a) and after (b) anti-seize paste contamination

1.3.2 Physical properties

Most characterization was performed on SnO_2(F)-coated SiO_2 samples, as the stainless steel substrates were too large for most instruments to accommodate. Film thickness and morphology were determined via scanning electron microscopy (SEM). The thickness of samples on SiO_2 substrates was ascertained by analyzing a freshly-cleaved cross-section surface. All SEM micrographs were collected using a Zeiss Supra 55 scanning electron microscope.

Ideally, the evaluation of a dopant includes an accurate assessment of the element's abundance in a given film. The quantification of fluorine concentration is an experimental challenge. Methods such as X-Ray Fluorescence (XRF) Spectroscopy are unable to detect such a light element consistently. X-Ray Photoelectron Spectroscopy (XPS) can detect fluorine, but three problems arise. First, below a concentration of ca. 1 at. %, fluorine peaks are difficult to detect, so the range of accessible compositions is limited. Second, fluorine is also vulnerable to preferential sputtering compared to the heavier element Sn, so even low-energy sputtering can impact the measured fluorine content of a film. Third, virtually all samples exposed to the air acquire carbon surface contaminants, and the peaks for F1s electrons bound to a metal have similar binding

energies to those bound to carbon. These carbon-bound fluorine atoms are not likely to be electrically active, and may simply be part of the surface contamination layer, and thus are not included in the film composition. Carbon contamination must therefore be reduced or eliminated to permit deconvolution of the peaks associated with metal- and carbon-bound fluorine. To remedy these problems, a longer dwell time was used on the fluorine scan to increase the signal to noise ratio.[v] The fluorine KL1 auger peak was used to confirm the presence of fluorine. Low-energy (2 keV) cluster sputtering was used to clean the surface before measurement, and composition scans were performed before and after sputtering. Owing to difficulties in quantifying the fluorine content, XPS was used primarily to confirm the presence of fluorine in select films as part of validating the deposition process. XPS samples were measured using a Thermo Scientific K-Alpha spectrometer with a 12 kV electron beam and a monochromatized Al Kα X-ray source (1486.7 eV). Surface cleaning was performed in situ with an argon sputtering gun in cluster (2000 atoms) mode. Sputtering energies were 2 keV unless otherwise noted. The energy resolution was 0.1 eV for element scans. A pass energy of 50 eV was used for element scans. A dwell time of 25 ms was used for all element scans but fluorine, where 50 ms was used. To establish electrical contact between the sample stage and the film, a copper clip pressed onto the surface of the film was used to hold the sample in place. The center of each sample was targeted for analysis, and the clip was placed as near as possible to the region of interest. Elemental compositions were determined using high resolution scans performed in the energy ranges relevant to elements of interest. The C1s, O1s, F1s, and Sn3d peak areas were fitted with a "Smart" background and the built-in instrument calibrations were used for element quantification.

---

[v] XPS counts are reported as counts/second, so the slower scan is expected to reduce noise, not change the area of the peak. This was confirmed by an overlay of "slow" and normal F1s scans.

Assessing film continuity is crucial to evaluating the promise of a coating. SEM micrographs fail to expose small pinholes that nonetheless result in substrate exposure. A more efficient and effective method is to treat samples with an etchant that aggressively attacks the substrate material and leaves the film untouched. The etchant is able to reach the substrate through tortuous paths not visible in SEM micrographs. When a film with pinholes comes into contact with the etchant, the film beneath the pinholes is undercut by substrate etching. This causes the film to crack and lift off the substrate, eventually creating holes visible to the naked eye.

For films on SiO_2/Si substrates, 5:1 buffered oxide etch solution was used (J.T. Baker, CMOS/microelectronic grade). On bare silicon thermal oxide wafers, with an estimated etch rate of 100 nm/min,[38] the solution dissolves the 300 nm SiO_2 film, revealing the silicon layer beneath. The difference in wetting angle between SiO_2 and Si makes the transition all the more obvious: the contact angle approaches zero as the fresh Si surface is exposed. If no substrate is exposed to an extent visible by eye within the designated etchant exposure time, the film is determined to be pinhole-free in that region. SnO_2(F) films on stainless steel were tested using an aqueous solution of 20 % (v/v) hydrochloric acid (Sigma-Aldrich, ACS reagent grade, 37 %) and 5 % (w/v) iron (III) chloride (Sigma-Aldrich, reagent grade, 97 %).[39] Upon exposure to this mixture, bare stainless steel roughens visibly, produces bubbles, and dissolves.[vi]

Figure 1.3.11 shows SEM micrographs of a stainless steel surface before and after etching in $FeCl_3$/HCl etching solution at 40 °C. Maintaining an etchant bath at this temperature was impractical, and etching was sufficiently rapid that room temperature exposures were used instead.

[vi] Rao, et al. report an etch rate of 65 μm per 45 minutes for stainless steel 304 at 40 °C. This grade is in general less chemically resistant.

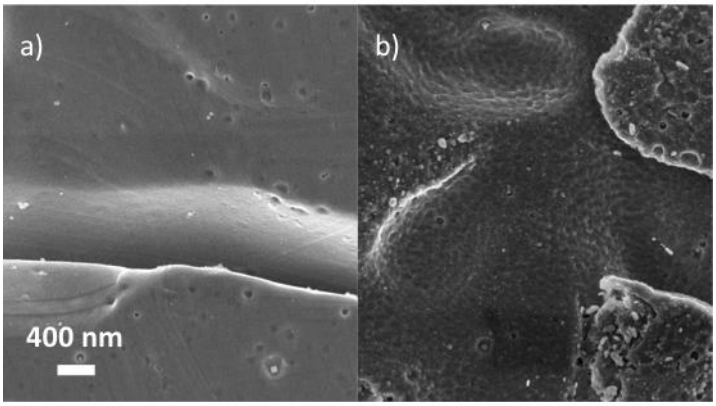

Figure 1.3.11: 316 stainless steel a) before and b) after iron chloride/HCl etching at 40 °C.

Since the actual stainless steel substrates were too large to examine by SEM, a small piece of much smoother stainless steel was used. An increase in surface roughness was visible by eye in this piece and other substrates that were etched at room temperature. The length of exposure varied based on the experiment, and is noted in the text where relevant. To test whether the $FeCl_3$/HCl etchant was likely to affect the films, commercial SnO_2(F) (12 Ω/sq nominal) was immersed in $FeCl_3$/HCl etching solution at 49 °C for 34.5 hours.[vii] The appearance of the film by eye, as well as the sheet resistance (11.8 Ω/sq), remained unchanged. In the same time period, a similarly exposed stainless steel piece lost ca. half of its volume.

1.3.3 Electrical properties

The electrical properties of films deposited on SiO_2 were evaluated to confirm the deposition of SnO_2 and SnO_2(F) and compare the properties with literature values. The sheet resistance of films, which can be multiplied by the film thickness to obtain its resistivity, was measured using a four-point probe (FPP-5000 Automatic Resistivity Meter or Creative Design

[vii] The container was unsealed, so some water was lost from the solution.

Engineering ResMap).

To determine the expected change in cell resistance when one graphite flow plate is exchanged for SnO2(F)-coated stainless steel, potential coatings were measured in a "dry cell" set-up. A flow battery cell is assembled without a membrane, and one graphite electrode is replaced with a SnO2(F)-coated stainless steel plate of comparable size. Figure 1.3.12 shows a diagram of the dry cell set-up. The membrane is omitted from the measurement because it does not contact

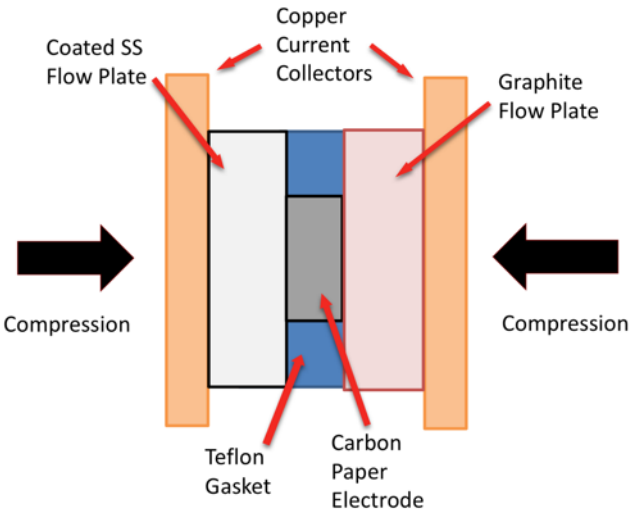

Figure 1.3.12: ASR "dry" cell set-up. Connection to the potentiostat is made through copper current collectors. A pair of electrically isolated stainless steel plates is used to compress the assembly, ensuring good electrical contact between the plates and the electrode.

the coated plate during cell operation, and the sensitivity of membrane resistance to external conditions is likely to confound, rather than improve, measurements of coating resistance. Values for cell resistances are also reported as area-specific resistances (ASR), defined as the resistance of the cell multiplied by the area of the electrode. The measurements are conducted without electrolyte to assess the resistance contribution of coatings independent of a perfectly continuous film. While less crucial for good through-plane conductivity and contact resistance, the presence of small pinholes could permit under-cutting and de-lamination of the coating, artificially raising the measured resistance.

When cell resistance is measured in this configuration, contact resistances at the interfaces of the cell, rather than materials' bulk resistances, are expected to be the dominant contributor to changes in resistance. This view can be illustrated by two simple calculations. Assuming, for example, a bulk resistivity of 0.2 Ω·cm for a one micron FTO film with a 5 cm^2 contact area (a thick film with a resistivity equal to the highest value measured for neat SnO_2 in this system), one could expect a contribution of 0.04 mΩ to the total resistance of the cell. For reference, a dry cell assembled with graphite plates and the typical carbon paper (SGL 39aa) has a total dry cell resistance of 9 ± 2 mΩ. All else equal, a resistivity increase of 50-fold from neat SnO_2 is required to for the bulk resistance to exceed the error of that measurement. In the case of the stainless steel substrate, a 0.5″ × 3″ × 3″ plate with a resistivity of 4.6×10^{-5} Ω·cm has a bulk resistance of 0.001 mΩ. A resistivity increase of 2,000-fold is required to match the listed dry cell resistance error.

The specific details of the dry cell resistance measurement are as follows: The graphite plate opposite the sample is a commercially-available unsealed graphite flow plate (Entegris, custom-made) with interdigitated flow channels (see Figure 1.2.2). The electrode is a single 5 cm^2 sheet of carbon paper (either Sigracet SGL-39AA, thickness 280 μm, or Sigracet SGL-10AA, thickness 390 μm), baked at 400°C in air for 24 hours. To control the amount of electrode compression during cell assembly and use, spacers were made of 3 × 3″ Teflon sheets with electrode-sized cut-outs. A total spacer thickness of 10 mils (0.254 mm) was used for SGL-10AA, whereas 8 mils (0.203 mm) was appropriate for SGL-39AA. Nine bolts (3/8″diameter, 16 threads/inch), arranged as shown in Figure 1.3.13, were used to connect the outer stainless steel compression plates. Upon assembly, all bolts were finger-tightened, then all were tightened with

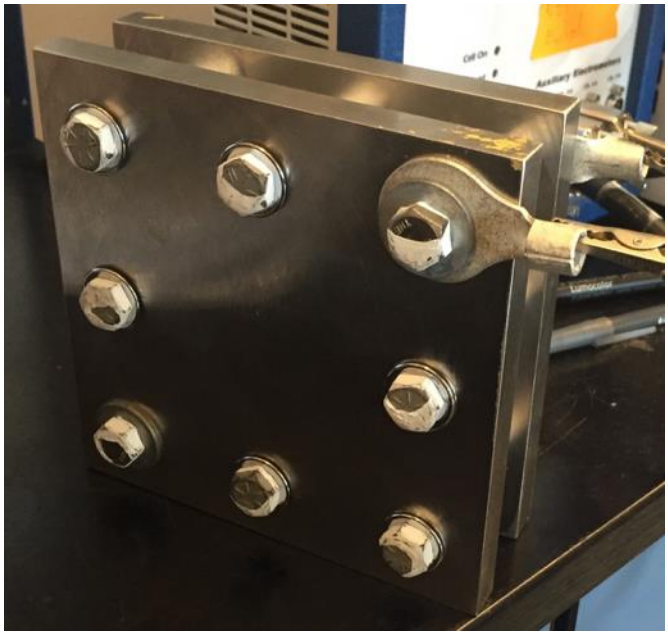

Figure 1.3.13: Arrangement of bolts for dry cell test apparatus.

a torque wrench to 30 in·lbs then 60 in·lbs, and finally 68 in·lbs.[viii] Electrical contact was made by bolting the potentiostat connectors to the copper current collectors, or using alligator clips. Both attachment methods provided equivalent results. The resistance of the cell was determined by scanning from -0.05 to 0.05 V, measuring the resulting current, and fitting the resulting trace to a line. The inverse of the current vs. voltage slope is the resistance. Typically, three resistance measurements were collected for each sample and averaged. The reported error is a 95 % confidence interval of these measurements. These scans were collected using a Gamry Instruments Reference 3000 potentiostat with 30k booster. With the exception of the omitted membrane and coated stainless steel plate, all components used were in the standard configuration for cell operation.[1]

Minimizing the resistance of this modified flow battery cell requires addressing the

[viii] The standard 6-bolt flow battery cell used 90 in·lbs per bolt. A torque of 68 in·lbs per bolt was chosen to achieve the same net compressive force using 9 bolts.

resistances of the new interfaces introduced by a SnO_2(F)-coated plate. Figure 1.3.14 displays the locations of the primary contact resistances in the dry cell set-up. The interfaces are 1) copper-SS 2) graphite-copper, 3) SS-SnO_2, 4) SnO_2-carbon, and 5) carbon-graphite. To establish the relative

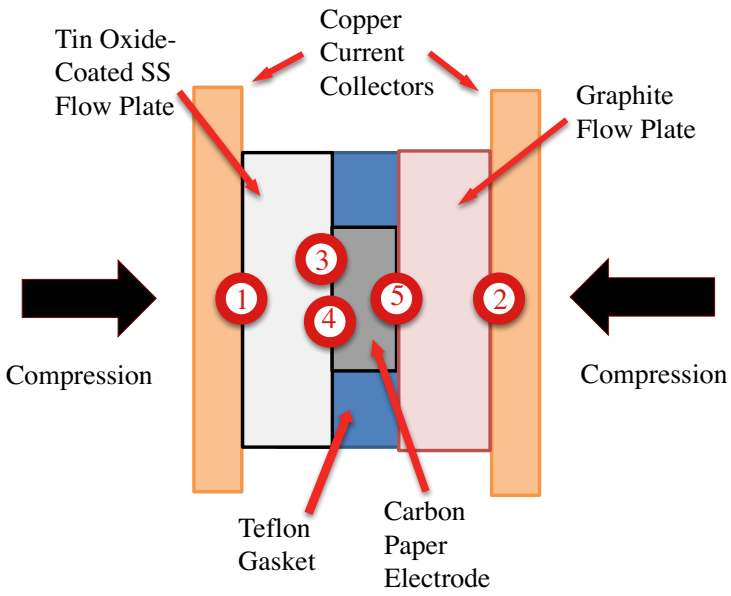

Figure 1.3.14: Interfaces contributing to cell resistance: 1) copper-SS 2) graphite-copper, 3) SS-SnO_2, 4) SnO_2-carbon, and 5) carbon-graphite

contributions of the different cell interfaces, and confirm whether doping targets the most resistive interfaces, a series of resistance measurements were performed in three different configurations of the dry cell measurement. Figure 1.3.15 a shows the "full" dry cell measurement (also displayed in Figure 1.3.12) used to ascertain the total resistance of a cell with a coated plate. Figure 1.3.15 b shows a "substrate only" measurement, which is used to ascertain the resistance of the interface of a substrate with the copper current collectors. Finally, Figure 1.3.15 c shows a "substrate-film" measurement, which targets the resistance of the substrate-film interface (and assumes that the substrate-copper interface is known from measurement b.

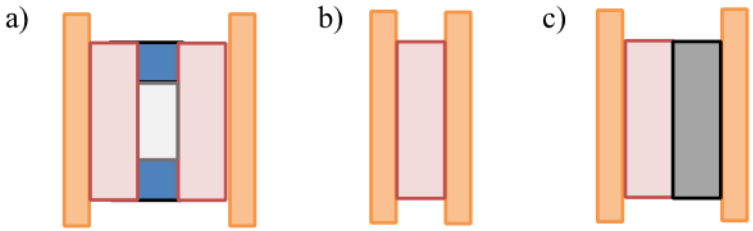

Figure 1.3.15: Variations on the dry cell measurement. a) full dry cell measurement, b) substrate-only and c) substrate-film

The resistance of interfaces 1 and 2 (Cu-SS and graphite-Cu, respectively), were measured by placing a substrate of either SS or graphite between the copper current collectors, and tightening the compression plates as usual. This arrangement is shown in Figure 1.3.15 b. Since the two nominally identical interfaces should be the dominant contributors to the resistance, half of the measured value was assumed to be equal to the resistance contribution of one interface. This technique was used to measure a graphite plate, an as-received SS substrate, a SS substrate heated under house nitrogen flow, and a SS substrate heated under purified nitrogen flow. The heating protocol matched a typical deposition protocol in time and temperature, but the SS substrates were never exposed to TMT, oxygen, or bromotrifluoromethane.

To determine the contact resistance of the SS-SnO_2(F) interface, the coated side of a sample was placed in contact with a stainless steel substrate heated under purified nitrogen flow, as demonstrated in Figure 1.3.15 c. Here, the resistance measured was assumed to be the sum of two SS-Cu interfaces and two SS-SnO_2(F) interfaces. By using this resistance and the previously determined SS-Cu interfacial resistance, one can calculate the sum of the two SS-SnO_2(F) interfaces. Half of this value is an estimate of the SS-SnO_2(F) contact resistance. These two SS-SnO_2(F) interfaces might differ in contact resistance for two primary reasons. First, the contact between the SS substrate and the SnO_2(F)-coated plate cannot be as complete and continuous as that of a coating atop a substrate. This suggests that the contact resistance of the opposing SS

substrate and SnO_2(F) coating would be higher than that of the coated SS substrate and its SnO_2(F) overlayer. The second distinction lies in the potential chemical modification of the surface of the coated SS substrate during the initiation of deposition. Until the SnO_2(F) overlayer is complete, any exposed SS is likely oxidized. This might further increase contact resistance with the overlayer. The most conservative estimate of this interfacial resistance is to use half the value as the lower end of the range, and the full value as the (potentially greatly overestimated) upper bound. For simplicity, the average of the two interfaces is used in interface resistance calculations. In the end, the intent is to determine the relative contribution of each of the interfaces on the total cell resistance. The SnO_2(F)-carbon paper interface resistance is sufficiently large to dwarf even the conservative estimate.

To ascertain whether heating the SS substrate before deposition impacted the SS-SnO_2(F) contact resistance, the test indicated in Figure 1.3.15 c was performed with the SS-SnO_2(F) sample against an as-received SS substrate, a SS substrate heated under purified nitrogen, and the same heated substrate polished on the SnO_2(F)-contacting side (to determine whether polishing restored this interface resistance to that of the unheated SS). Errors were calculated using the error propagation equation below, where σ_y is the error of the calculated value y, σ_{z_i} is the error of the ith independent variable z, $\frac{\partial y}{\partial z_i}$ is the partial derivative of the calculated value y with respect z_i.

$$\sigma_y = \sqrt{\sum_{i=1}^{n} \left(\frac{\partial y}{\partial z_i}\right)^2 \left(\sigma_{z_i}\right)^2} \qquad [1.3.3]$$

Finally, for the test sample, a full dry cell measurement was performed using Sigracet SGL 39aa carbon paper as the electrode. The resulting value was assumed to be the sum of one SS-Cu, SS-SnO_2(F), SnO_2(F)-carbon paper, carbon paper-graphite, and graphite-SS interface. Subtracting the previously calculated values for all interfaces but SnO_2(F)-carbon paper, that resistance can be

obtained. Here, half the full dry cell measurement of a graphite plate with SGL 39aa is assumed to be sum of one carbon paper-graphite and one graphite-SS interface.

1.3.4 Chemical stability

The chemical stability of $SnO_2(F)$ films was assessed through extended electrolyte exposure. Stability was monitored by measuring sheet resistance with a four-point probe (FPP-5000 Automatic Resistivity Meter), by visual inspection, and by SEM imaging. In the first type of test, a commercial sample of $SnO_2(F)$ was submerged for two weeks in a sealed container filled with pure bromine (Aldrich, reagent grade). In the second type of test, $SnO_2(F)$- and SnO_2-coated silicon oxide wafers were submerged at 58 ± 2 °C in an electrolyte solution of elevated but realistic operating concentrations of 1.5 M bromine and 3 M hydrobromic acid (Fluka, purum, >48 %). For the first 10 days, the samples and electrolyte were enclosed in a glass pressure vessel with Teflon seals. Subsequently, a water-cooled condenser was used for these samples to minimize Br_2 and HBr loss to the atmosphere. A diagram of this set-up, which is preferable to the sealed system for safety reasons, is shown in Figure 1.3.16. The pieces were subjected to Br_2/HBr exposure and heat for over two months. Periodically, the samples were removed, washed with DI water, and the sheet resistance was measured.

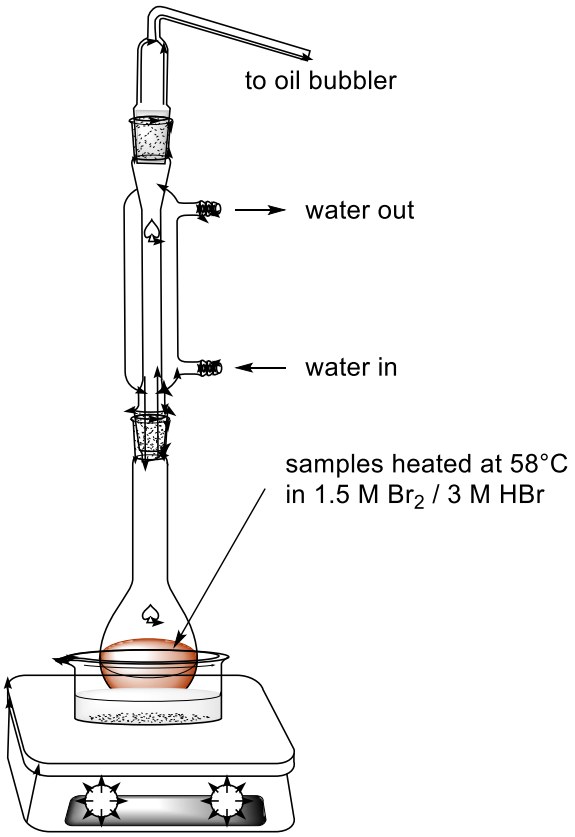

Figure 1.3.16: The reflux system used to enclose the samples and electrolyte solution during heating tests.

1.4 Results and discussion

Thin films of $SnO_2(F)$ were deposited on silicon themal oxide wafers using atmospheric pressure chemical vapor deposition (APCVD). These films were characterized to confirm the chemical stability, composition, growth rate, and resistivity of the material, as well as to assess and iteratively optimize deposition uniformity.[ix] $SnO_2(F)$-coated stainless steel substrates were

[ix] There is no reason, *a priori*, to expect that the initiation of $SnO_2(F)$ film growth on different substrates will be identical (e.g., silicon thermal oxide and stainless steel). However, relatively thick films have been deposited in this work, such that substrate effects are not expected to impact the properties under study.

used to determine the impact of deposition conditions on the area-specific resistance and continuity of a given film.

1.4.1 Characterization of $SnO_2(F)$ on silicon thermal oxide substrates

1.4.1.1 Composition

Given the challenge of measuring small fluorine concentrations, film composition was assessed primarily to verify, rather than precisely quantify, the presence of fluorine. For the purposes of developing a functional protective coating, the specific concentration of fluorine was less important than the combined effect of fluorine incorporation and doping efficiency on the carrier concentration. This was evaluated indirectly by the resistance measurements described in a later section, and hence, further quantification of fluorine content was not necessary.

XPS was used to confirm the presence of fluorine in samples deposited at 450 or 468 °C on silicon thermal oxide. The first set of samples were deposited for 30 minutes at 450 ± 2 °C under a flow of 5.7 μmol/min tetramethyltin (TMT), 780 μmol/min oxygen, and a balance of nitrogen to reach a total flow rate of 104, 93, or 90 sccm. The $BrCF_3$ delivery rates were 123, 180, and 270 μmol/min, respectively. The fluorine KL1 Auger peak was used as an indicator of fluorine unaffected by the presence of carbon. A small peak was observed for all three samples. The measured ratio of fluorine to tin (0.07, 0.07, 0.05) and the measured F composition (2.1, 1.9, and 1.4 at. %) decreased with increasing $BrCF_3$ delivery rate. However, the composition error is ca. 1 at. %, and the detection limit is ca. 0.5 at. % F, so these values are not distinguishable from one another accounting for the error. Carbon content was ca. 3-4 at. %; residual organic surface contaminants remained after argon cluster sputtering for 720 seconds.

The presence of fluorine could not be confirmed for samples deposited for 30 minutes at

468 ± 2 °C under varying $BrCF_3$ delivery rates. Samples were subjected to the following reactant delivery rates: 2.7 μmol/min TMT; 780 μmol/min oxygen; 36, 54, or 72 μmol/min $BrCF_3$; and a balance of nitrogen to reach a total flow rate of 98, 97, or 96 sccm. Here, the measured F composition (0.7, 0.7, and 0.9 at. %) was essentially at the detection limit—the low signal-to-noise ratio prevented the analysis of some sputtering levels. The fluorine KL1 Auger peak was not distinct from background noise. This result does not preclude the possibility of fluorine incorporation in the higher temperature samples: this technique cannot detect fluorine in a commercially-available 18 Ω/sq SnO_2(F) piece. Carbon content was ca. 8, 6, and 4 at. %; residual organic surface contaminants remained after cluster sputtering for 480 or 720 seconds (for the 72 μmol/min $BrCF_3$ sample).

The presence of fluorine was confirmed by XPS for samples deposited at 450 °C, but not for those deposited at 468 °C. Further discussion of the impact of fluorine incorporation is discussed in a later section addressing the dry cell resistance of SnO_2(F)-coated plates.

1.4.1.2 Growth rate and deposition patterns

The techniques employed to optimize the deposition process and minimize sample to sample variation have been described in the materials and methods section. A more detailed assessment of growth rate and deposition uniformity was pursued by depositing samples under varying total flowrate, but otherwise identical conditions. As demonstrated in Figure 1.4.1, the growth rate varies with distance from the center of deposition. These three samples were deposited

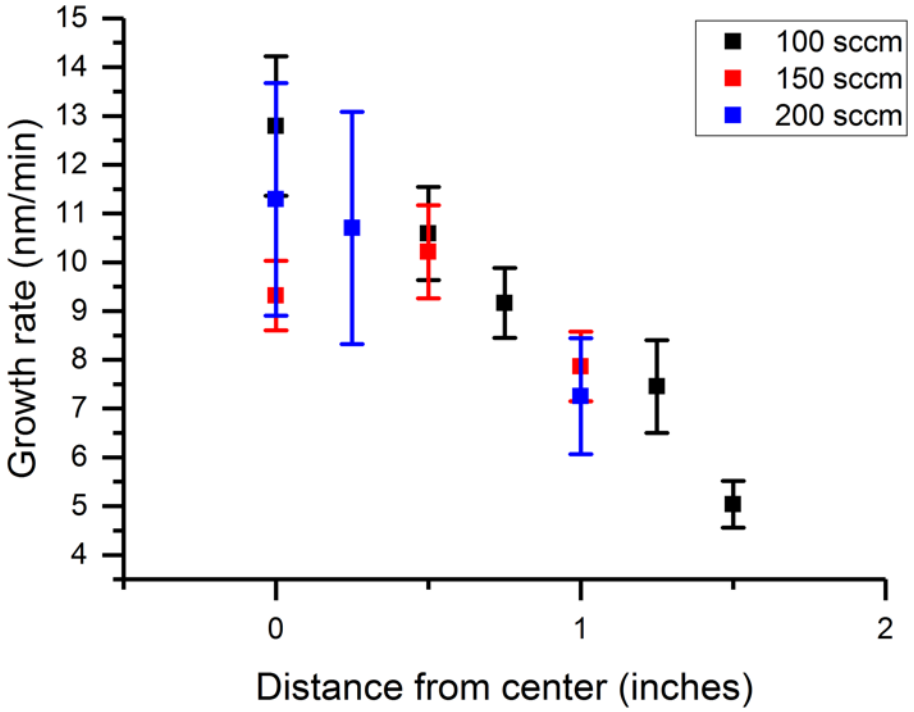

Figure 1.4.1: A comparison of growth rates versus distance from the center of deposition for different flow rates. Samples were deposited for 21 minutes at 450 °C with 5.7 µmol/min TMT[x], µmol/min $BrCF_3$, 780 µmol/min oxygen, and a balance of nitrogen to reach 98, 150, or 200 sccm. Growth rate error is determined by error propagation using the thickness error. Thicknesses are single measurements with error estimated from the SEM cross-section micrograph.

for 21 minutes at 450 °C with 5.7 µmol/min TMT[x], µmol/min $BrCF_3$, 780 µmol/min oxygen, and a balance of nitrogen to reach 98, 150, or 200 sccm.[xi] The center of deposition was assumed to be the center point of the smallest concentric fringe. This point is marked as zero on the plot, and thickness cross-sections were analyzed by SEM at this point and at points across the sample, along

[x] For these three depositions, a 602 flow tube was used for TMT (1.23 % in nitrogen). The accuracy of delivery is ± 330 µmol/min TMT, and the repeatability is ± 0.25 %, or ± 0.014 µmol/min. As mentioned in the materials and methods section, the same flow tube is used for each reactant from one deposition to the next. Hence, the run-to-run variability should be very small.

[xi] The total flow rate error is ± 1 sccm.

a single line perpendicular to the fringes. The reported growth rates are the thickness at each point divided by the deposition time. Except for the center point, the trends are remarkably similar; where direct comparisons are possible, the growth rate for each flow rate agrees within error. The growth rate of the center point decreases with increasing flow rate, and the depositions at 98 and 200 sccm are distinguishable after accounting for error. This trend has been observed with APCVD tin oxide previously,[23] and is consistent with two explanations. Gas delivered at a higher flowrate must travel farther along the sample to reach the same temperature. A higher flowrate, then, may give rise to a lower temperature at the center of the reactor; the growth rate in the center of the sample, where the gas has not thermally equilibrated, would then decrease. If temperature drives difference the growth rate, then different flowrates would be expected to produce similar growth rates after the gas has reached its steady-state temperature, consistent with the observed pattern of growth rates. Alternatively, and potentially simultaneously, intermediate gas phase reactions may require sufficient time to develop before deposition can occur. If this length of time is less than, but on the order of, the time required for a gas molecule to travel through the reactor, an increase in flow rate might subsequently reduce the growth rate at the center of deposition.

1.4.1.3 Bromotrifluoromethane impact

The presence of bromotrifluoromethane is known to accelerate the $SnO_2(F)$ deposition reaction.[23] This effect was observed in this system, as well. Above certain $BrCF_3$ flow rates, roughening of the film and powder formation have been observed during deposition, consistent with accelerated gas phase reactions. At 450 °C and 5.7 μmol/min TMT, a $BrCF_3$ delivery rate of 180 μmol/min or higher produces rough films that are cloudy in appearance. Figure 1.4.2 displays images of samples deposited over a range of $BrCF_3$ delivery rates. In addition to the change in appearance, films deposited with higher $BrCF_3$ delivery rates appear to be thicker at the center of

deposition. These observations are consistent with bromotrifluoromethane acting as a reaction accelerant.

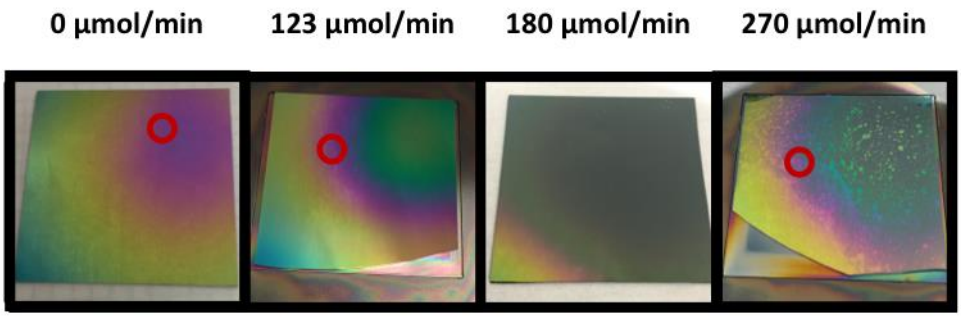

Figure 1.4.2: SnO_2 and SnO_2(F) samples deposited at 450 °C on silicon thermal oxide wafers with varying $BrCF_3$ flow rates (listed above each image). Where estimations can be made, red circles mark regions of approximately equal thickness, based on fringe color. All samples were subject to delivery rates of 5.7 µmol/min TMT and 780 µmol/min oxygen, and an excess of nitrogen to reach a total flow rate of ca. 96 sccm. Total flow rate 98, 104, 93, and 90 sccm. (96 ± 6 sccm, stdev). Depositions were conducted for 30 minutes at 450 ± 2 °C.

At 468 °C, evidence for reaction acceleration with increasing $BrCF_3$ delivery rate is weaker. The film thickness at the center of deposition is thinner for samples with higher delivery rates of $BrCF_3$. This trend is demonstrated by Figure 1.4.3; samples were deposited with a TMT delivery rate of 2.7 µmol/min, and a variety of $BrCF_3$ delivery rates. As the delivery rate is increased from 36 to 72 µmol/min (particularly from 54 to 72 µmol/min), the center of deposition appears thinner, but also shifts to the right. The shift in the deposition center is likely due to the run-to-run variability described earlier. The thinning of the deposition center could be explained by the formation of powder in the gas phase, transitioning to film roughening at higher $BrCF_3$ delivery rates. While these films appear smooth and shiny by eye, the surface of a film deposited with 123 µmol/min $BrCF_3$ (not pictured), is cloudy in appearance. While an increase in $BrCF_3$ delivery appears to create rough films and powder (consistent with accelerated gas phase reactions), there is no conclusive evidence that $BrCF_3$ causes *growth rate* acceleration in this system.

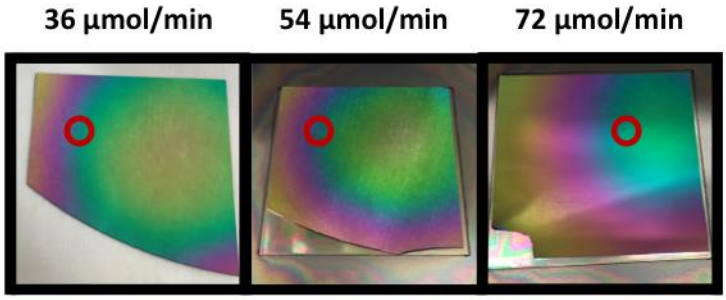

Figure 1.4.3: SnO_2 and SnO_2(F) samples deposited at 468 °C on silicon thermal oxide wafers with varying $BrCF_3$ flow rates (listed above each image). Red circles mark regions of approximately equal thickness, based on fringe color. Depositions were conducted for 30 minutes at a temperature of 468 ± 2 °C, under a flow of 2.7 µmol/min TMT, 780 µmol/min oxygen, and either 36, 54, or 72 µmol/min $BrCF_3$, and a balance of nitrogen to reach 98, 97, or 95 sccm. (97.0 ± 0.6 sccm, stdev).

1.4.1.4 Electrical properties

Neat SnO_2 and SnO_2(F) films deposited on silicon thermal oxide wafers produced resistivities consistent with literature values for APCVD SnO_2. The SnO_2 film resistivities shown in Figure 1.4.4 are deposited by APCVD at 350 °C (from ref. [40]), or from this work. All samples from this work were deposited under a flow of 5.7 µmol/min TMT, 780 µmol/min (19 sccm) oxygen, and a balance of nitrogen to reach a total flow rate of 98 sccm. For the 80 and 61 nm films, a single deposition was conducted at 448 ± 3 °C for 30 minutes. Two sections of different thicknesses were removed from the sample and analyzed. The 76 nm film was deposited at 451 ± 1 °C for 15 minutes. The 245 nm film was deposited at 451.5 ± 0.5 °C for 30 minutes. The resistivities are reported as averages of 3 measurements with 95% confidence intervals. Thicknesses are single measurements with error estimated from the SEM cross-section micrograph. The chemistry and temperature in this work differs from that used in ref. [40]; exact agreement is not expected, but the ranges are in agreement.

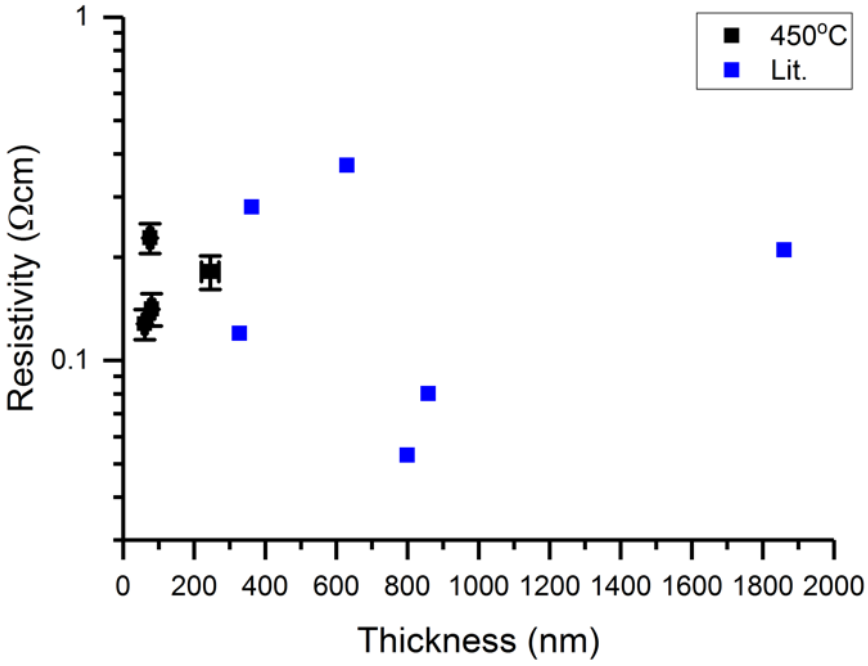

Figure 1.4.4: SnO_2 resistivities from this work and literature.[40] All samples were deposited under a flow of 5.7 µmol/min TMT, 780 µmol/min (19 sccm) oxygen, and a balance of nitrogen to reach a total flow rate of 98 sccm. For the 80 and 61 nm films, a single deposition was conducted at 448 ± 3 °C for 30 minutes. Two sections of different thicknesses were removed from the sample and analyzed. The 76 nm film was deposited at 451 ± 1 °C for 15 minutes. The 245 nm film was deposited at 452 ± 1 °C for 30 minutes. The resistivities are reported averages of 3 measurements with 95 % confidence intervals. Thicknesses are single measurements with error estimated from the SEM cross-section micrograph.

The resistivities of a selection of SnO2(F) films deposited at 450 and 520 °C are plotted in Figure 1.4.5. For these samples, a single deposition was conducted for 30 minutes at 450 ± 2 °C under a flow of 5.7 µmol/min TMT, 123 µmol/min bromotrifluoromethane, 780 µmol/min (19 sccm) oxygen, and a balance of nitrogen to reach a total flow rate of 104 sccm. Two sections were removed from the sample and analyzed. For the 87 and 130 nm films, a single deposition was conducted at 520 ± 1 °C for 15 minutes under a flow of 4.5 µmol/min TMT, 51 µmol/min bromotrifluoromethane, 780 µmol/min (19 sccm) oxygen, and a balance of nitrogen to reach a total flow rate of 98 sccm. Two sections of different thicknesses were removed from the sample

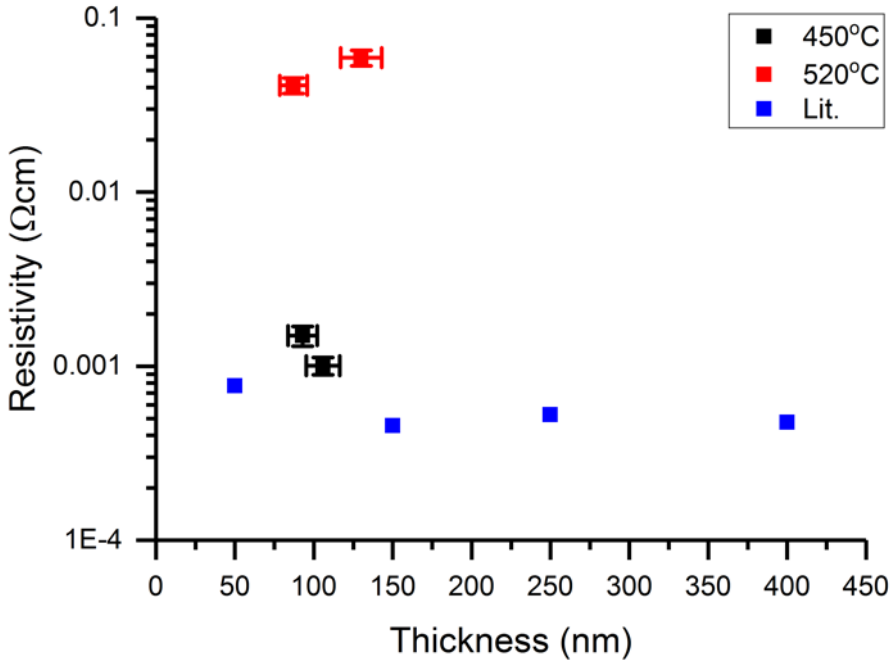

Figure 1.4.5: $SnO_2(F)$ resistivities from this work and literature.[23, 31] For the 93 and 106 nm samples, a single deposition was conducted for 30 minutes at 450 ± 2 °C under a flow of 5.7 µmol/min TMT, 123 µmol/min $BrCF_3$, 780 µmol/min oxygen, and a balance of nitrogen to reach a total flow rate of 104 sccm. Two sections were removed from the sample and analyzed. For the 87 and 130 nm films, a single deposition was conducted at 520 ± 1 °C for 15 minutes under a flow of 4.5 µmol/min TMT, 51 µmol/min $BrCF_3$, 780 µmol/min oxygen, and a balance of nitrogen to reach a total flow rate of 98 sccm. Two sections of different thicknesses were removed from the sample and analyzed. The resistivities are reported as averages of 3 measurements with 95 % confidence intervals. Thicknesses are single measurements with an assigned error of 10 %.

and analyzed. $SnO_2(F)$ films deposited at 450 °C show a decrease in resistivity with increasing thickness, which is consistent with more densely-packed, larger grains developing in a thicker film. $SnO_2(F)$ films deposited at ca. 520 °C show higher resistivity than samples deposited at 450 °C, likely due to the lower fluorine incorporation. It appears that in this system, fluorine incorporation may decrease with temperature; variations in fluorine concentration with temperature have been observed in the literature, including a decrease in incorporation with increasing temperature (though the temperatures in the reference are considered are considerably higher). The samples taken from ref. [23] were deposited at 570 °C, but are less resistive than the

520 °C (nominal) samples. This is consistent with the reference films containing higher concentrations of fluorine (ca. 9×10^{20} cm^{-3} fluorine). The deposition of tin oxide films with fluorine incorporation, resistivity consistent with the literature, and suitable uniformity was demonstrated. This initial iterative characterization and optimization stage paved the way for deposition of SnO_2(F) films on stainless steel and evaluation of the material as a protective coating.

1.4.2 Electrical properties in flow battery cells

Minimizing the total flow battery cell resistance is important for minimizing energy losses during charging and discharging. If a new coating and flow plate substrate is to be used, the impact on the resistive losses in the cell must be assessed. The ohmic resistance contribution of the coated flow plates was determined by measuring the resistance of a "dry cell", essentially a electrolyte- and membrane-less cell where one graphite electrode is replaced with a SnO_2(F)-coated stainless steel plate of comparable size. When the dry cell is assembled using graphite flow plates and SGL 39aa carbon electrodes, the ASR is 45 ± 11 $m\Omega cm^2$. While this value can serve as a reference point, it is not an upper limit to acceptable ASR: a coating with a higher ASR than a graphite plate would be preferred, provided that the material is not damaged by electrolyte exposure. In this section, the influence of the choice of carbon paper electrodes is noted, and the resistive contributions of the various cell interfaces are estimated. Finally, the impact of bromotrifluormethane delivery rate and temperature on the resistance of a dry cell assembly (the dry cell resistance) is measured and the new flow plates are compared with currently used graphite plates.

1.4.2.1 Impact of carbon paper on dry cell resistance

The measured dry cell resistance was markedly impacted by the choice of carbon paper

electrodes. Figure 1.4.6 compares dry cell resistances obtained by measuring each of a set of 6 samples using two different types of carbon electrodes: SGL 10aa and SGL 39aa. Samples were deposited with $BrCF_3$ delivery rates varying from 0 to 180 µmol/min. Samples are a subset of those shown later in Figure 1.4.12—only one sample represents a $BrCF_3$ delivery rate of 123 µmol/min. SGL 10aa was previously the standard carbon paper used for flow battery cells in this research collaboration. SGL39aa is the designated replacement for SGL 10 aa, yet for every sample, SGL

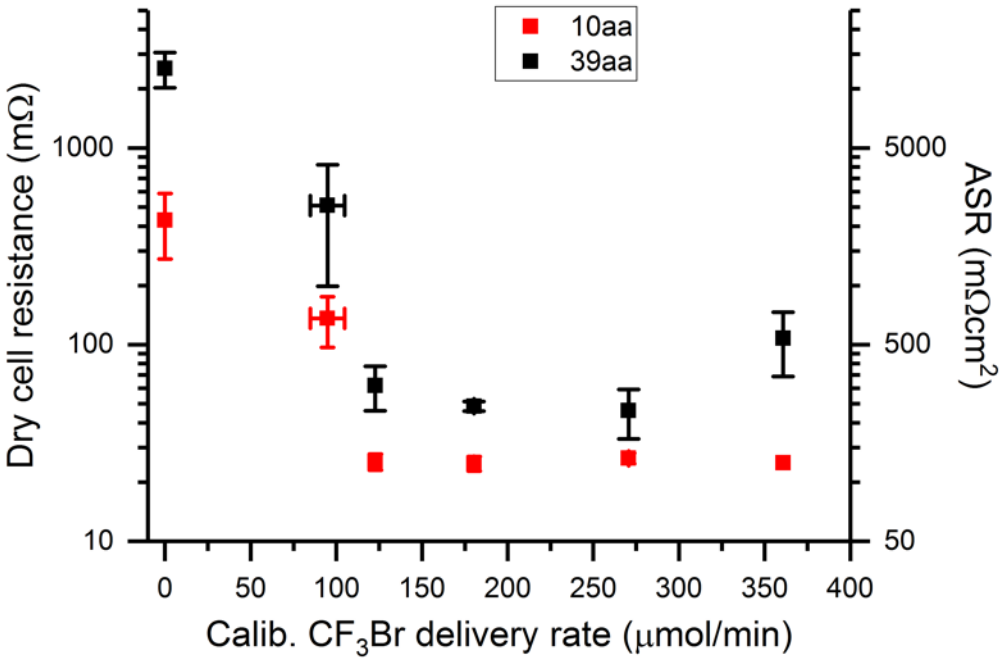

Figure 1.4.6: Dry cell resistance obtained by measure a set of 6 samples measured once using Sigracet SGL 39aa (red) and once using Sigracet SGL 10aa that had been exposed to 1 M sulfuric acid (black). Both types of electrodes were baked in air at 400 °C for 24 hours to activate the surface. All data points are averages of three measurements. Error bars are 95 % confidence intervals.

10aa-containing cells have significantly lower resistance. The difference is roughly 2-fold, except for neat SnO_2 (5.9-fold) and the highest $BrCF_3$ delivery rate (7.2-fold). In addition to a higher dry cell resistance, the error is higher for SGL 39aa cells for every coating but neat SnO_2. These observations suggest that a feature or features (e.g., morphology or compressibility) of the SGL

39aa paper both produce higher contact resistances, and less repeatable electrical contact. Although the increased contact resistance is responsible for a large portion of the estimated resistance contribution of SnO_2(F)-coated plates, the extraction of general trends is still possible. For example, both data sets follow a similar pattern of decreasing, then leveling off dry cell resistance with increasing $BrCF_3$ delivery rate. This is consistent with a reduction in contact resistance due to fluorine doping. Unfortunately, the increased error has the potential to obscure less pronounced trends, as will be evident in later sections.

1.4.2.2 Determining interfacial resistances in the dry cell measurement

To better understand the contribution of the various dry cell interfaces on the total resistance contribution, a series of modified dry cell resistance measurements were performed to separately estimate each interface. The resistance of the following interfaces were calculated using the measurements shown in Figure 1.3.15: stainless steel-copper (SS-Cu), stainless steel- doped tin oxide (SS-SnO_2(F)), and doped tin oxide-carbon paper (SnO_2(F)-Carbon).

The resistance of a SS-Cu interface and impact of heating stainless steel substrates were explored using stainless steel substrates heated under conditions that mimicking pre-deposition heating under nitrogen flow in the deposition chamber. After the standard cleaning procedure detailed earlier, stainless steel substrates were subject to the following treatments: heating under flow of "house" nitrogen with no purifier, heating under flow of purified house nitrogen, and heating under purified nitrogen, followed by sanding on both sides to restore the silver color of the surface.[xii] The substrate heated under purified nitrogen mimics the standard heating procedure

[xii] Sanding visibly increased the surface roughness.

used, while the substrates that were unheated or heated under unpurified nitrogen were intended to clarify the impact of heating and the importance of using a purifier. The polished sample was tested to ascertain whether polishing could reduce the interfacial resistance of a heated SS substrate, or restore it to the "unheated" value. Figure 1.4.7 displays the resistances calculated[xiii] for a single SS-Cu interface for a stainless steel substrate prepared under the listed conditions and for a graphite plate. Heating in the deposition chamber clearly increases the resistance of the SS-Cu interface, though purified and unpurified nitrogen preparations are not distinguishable within error. As evident from the two left most data points in Figure 1.4.7, polishing did not reduce the interfacial resistance. There are two physical changes that occur when the substrate is heated: first, a change in color from silver to a light golden color and second, the formation of a hardened surface layer that extends below the golden-colored layer. If this layer is the source of the resistance change, then restoring the SS-Cu interface to its "unheated" resistance is impractical: the hardened layer can only be removed by an endmill or similarly aggressive tool. Lastly, it should be noted that these resistance values are fairly small: often orders of magnitude smaller than the error on the measurements displayed in Figure 1.4.6.

Once the SS-Cu interfacial resistance has been measured, the SS-SnO_2(F) interface can be extracted by measuring the resistance of a treated stainless steel substrate placed against a coated stainless steel substrate, as shown in Figure 1.3.15 b. This resistance value consists of the sum of one measured SS-Cu interface (the fourth entry in Figure 1.4.7), one unknown SS-Cu interface

[xiii] As noted in the materials and methods section, this calculation assumes both SS-Cu interfaces are equivalent and that bulk SS resistivity is negligible.

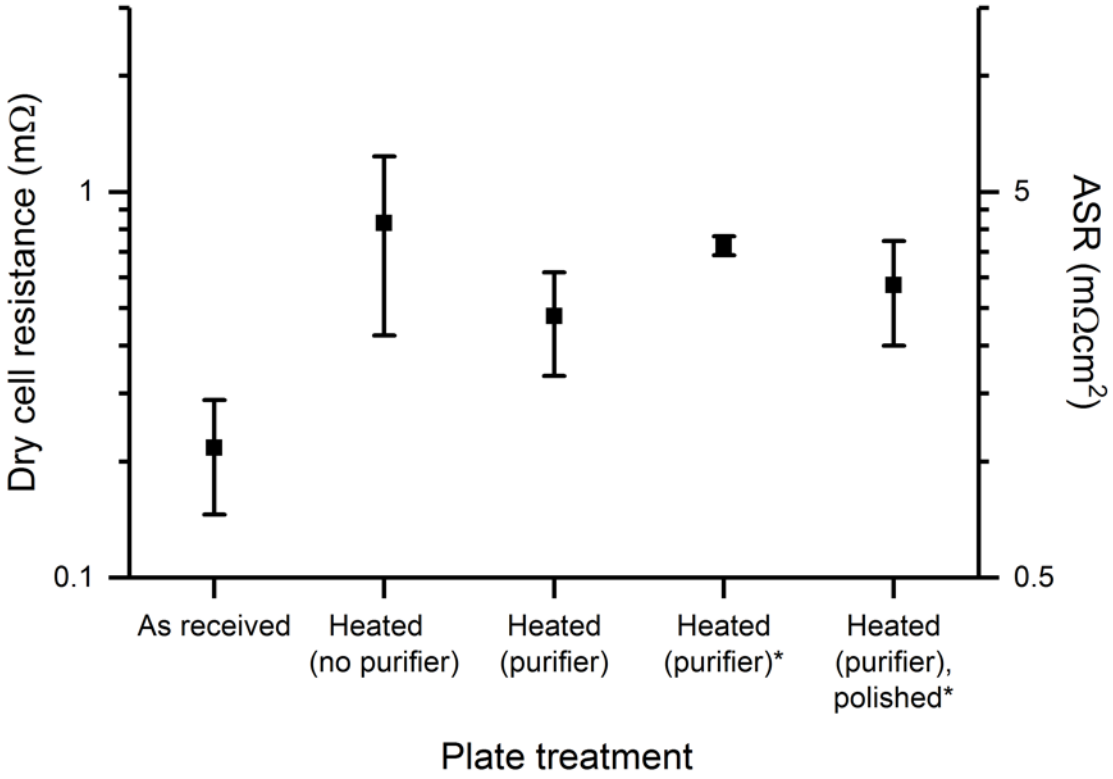

Figure 1.4.7: One-interface resistances (half the dry cell resistance measured by Figure 1.3.15 c of stainless steel plates measured as received, or heated under house nitrogen, purified nitrogen flow, or purified nitrogen followed by polishing both sides. Resistances and errors are reported as an average of multiple measurements, as detailed in the footnotes for: one unheated SS-Cu interface,[xiv] one average purified nitrogen-heated SS-Cu interface,[xv] one SS-Cu interface from a SS plate heated under house nitrogen with no purification,[xvi] and one SS-Cu interface of purified nitrogen-heated sample after polishing on both sides. The error bars indicate 95 % confidence intervals. The asterisk indicates measurements made on the same heated SS plate used in later SS-SnO_2(F) interface measurements.

(the back of the SnO_2(F) test sample, estimated by the average value of one SS-Cu interface, or

[xiv] 1 sample, 3 measurements, 95 % confidence interval.

[xv] 2 samples with 6 and 3 measurements, respectively. Error is a 95% confidence interval. Additional measurements were taken on the first sample because substantial variation was seen in the first three measurements.

[xvi] 1 sample, 4 measurements. Error is a 95% confidence interval.

the third entry in Figure 1.4.7), and two SS-SnO_2(F) interfaces. Subtracting the estimated resistance of the two SS-Cu interfaces from the dry cell resistance measured in the configuration shown Figure 1.3.15 b gives an estimate of the sum of the two SS-SnO_2(F) interfaces. Half of this value is an estimate of one heated SS-SnO_2(F) interface. The test sample was coated for 60 minutes at 450 °C, with a flow of 126 µmol/min CF_3Br, 5.7 µmol/min TMT, 780 µmol/min oxygen, and a balance of nitrogen to reach 94 sccm. The coated plate was measured in the configuration of Figure 1.3.15 b against an un-heated SS plate, a SS plate heated under purified nitrogen, and a heated SS plate polished on both sides.[xvii] Figure 1.4.8 shows the resulting dry cell resistance measurements.

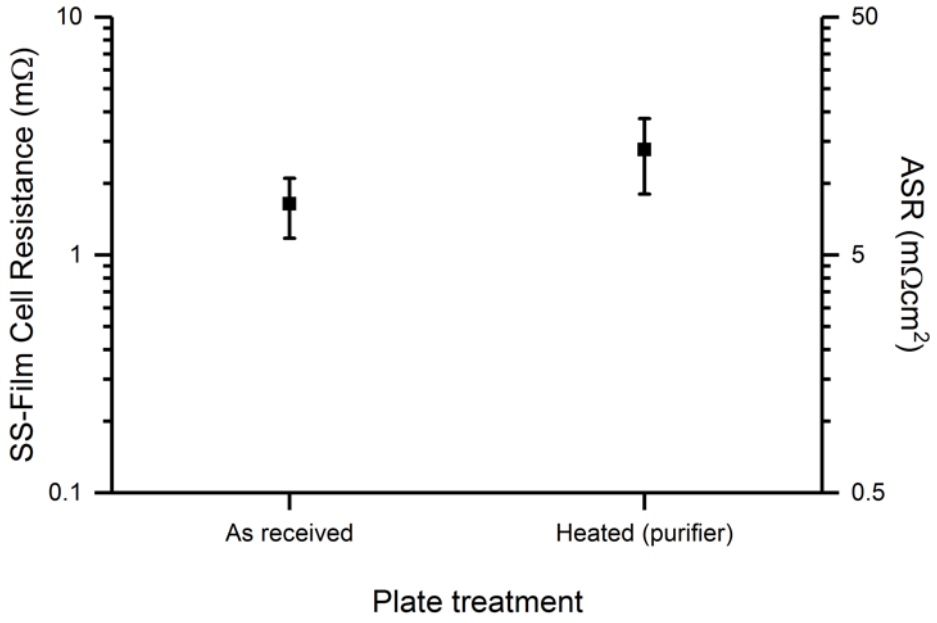

Figure 1.4.8: Dry cell resistances for a SnO_2(F)-coated plate measured against SS substrates that were unheated ("as received") or heated under purified nitrogen. Values are an average of three measurements for the un-heated SS plate, and four measurements for SS plate heated under purified nitrogen. Error bars indicate 95 % confidence intervals.

[xvii] These are the same SS substrates classified as unheated, heated under purified nitrogen, and heated, then polished on both sides in Figure 1.4.7.

From these values and the previously determined SS-Cu interface measurements, a SS-SnO_2(F) interfacial resistance of 0.7 ± 0.5 mΩ (ASR 3 ± 2 mΩcm^2) was obtained.

The full dry cell resistance measurement, shown in Figure 1.3.15 a, was performed on the test sample using SGL 39aa, and on a graphite plate using 39aa and 10aa, respectively. These measurements were intended to replicate the relevant interfaces in the full flow battery cell as closely as possible. These values are displayed in Figure 1.4.9.

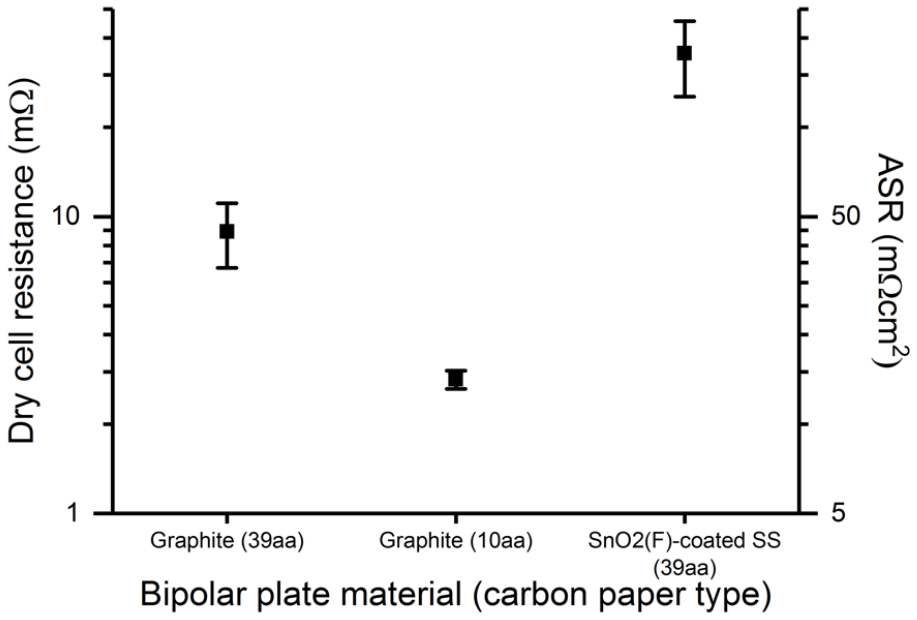

Figure 1.4.9: Full dry cell resistance values for a graphite plate using SGL 39aa carbon paper and SGL 10aa carbon paper, and a SnO_2(F)-coated SS plate. The deposition was conducted at 451 ± 1 °C for 60 minutes, under a flow of 5.7 μmol/min TMT, 126 μmol/min $BrCF_3$, 780 μmol/min (19 sccm) oxygen and a balance of nitrogen to reach a total flow rate of 94 sccm.

The dry cell resistance for graphite is lower than that of the test sample for both carbon paper types, and lower than values obtained for all SnO_2(F)-coated plates. The sum of half the full dry cell resistance of a graphite-39aa cell, the resistance of one SS-SnO_2(F) and one SS-Cu interface should be equal to the full dry cell resistance using the test SnO_2(F) minus the resistance of the SnO_2(F)-carbon paper interface. Since the SS-Cu interface represents the back side of the

SnO_2(F) sample, the average SS-Cu value was used. Hence, the SnO_2(F)-carbon paper interfacial resistance was calculated to be 30 ± 10 mΩ (ASR 150 ± 50 mΩcm^2). This value clearly dominates the full cell resistance, as shown in a comparison of various cell interfacial resistances (see Figure 1.4.10). This validates the focus of this work on tuning the carrier concentration of the SnO_2(F)

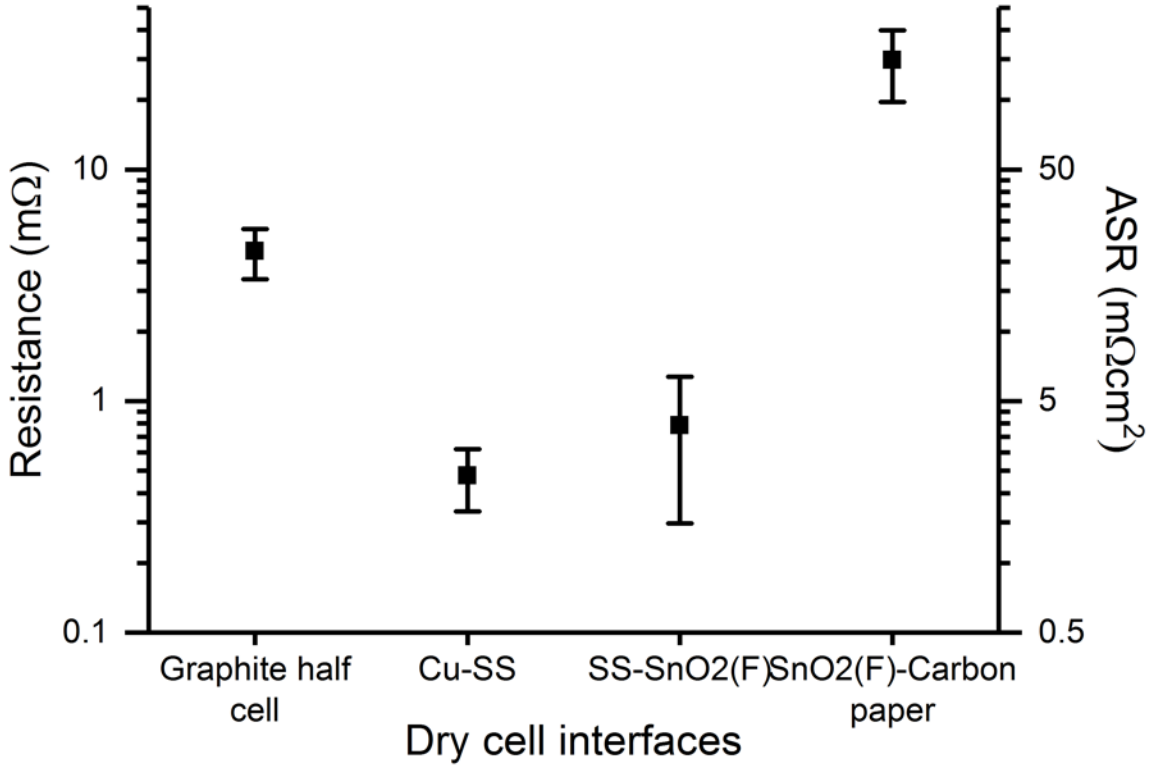

Figure 1.4.10: Dry cell interfaces measured (graphite half cell, Cu-SS, SS-SnO_2(F)) and calculated (SnO_2(F)-carbon paper). For graphite half cell and Cu-SS, the value and error is half of the average of three substrate-only measurements and half the corresponding 95 % confidence interval. For the other two interfaces, error propagation is performed using the values and errors of the relevant measurements.

film. Since only the SnO_2(F)-contacting interfaces are expected to change substantially, these values offer a reference for the coating's contribution to the contact resistance. The interfaces not involving SnO_2(F) have a total resistance of 5 ± 1 mΩ (ASR 27 ± 6 mΩcm^2). The somewhat high relative error inherent in these interface measurements is dwarfed by the large SnO_2(F)-carbon

paper contact resistance.

1.4.2.3 Dependence of dry cell resistance on deposition parameters

To minimize the dominant source of resistance—the $SnO_2(F)$-carbon paper interface—the electronic structure of $SnO_2(F)$ was tuned using by varying the temperature and bromotrifluoromethane and tetramethyltin delivery rates. Figure 1.4.11 demonstrates variation in dry cell resistance (and area-specific resistance)[xviii] of dry cells with bromotrifluoromethane delivery rate. The dry cell resistance is shown to decrease with increasing $BrCF_3$ flowrate before leveling off above a $BrCF_3$ flowrate of 123 μmol/min (3.0 sccm). These plates were coated at ~450 °C, under a flow of 780 μmol/min (19 sccm) oxygen and 5.7 μmol/min tetramethyltin (13 sccm of 1.1% TMT in nitrogen), with bromotrifluoromethane delivery rates varying from 0 to 6.5 μmol/min. The flow of purified nitrogen flow was adjusted to achieve a total flow rate of 96 ± 6 sccm (standard deviation).[xix] The deposition time was 30 minutes in all cases and SGL 39aa carbon paper is used.

The reduction in dry cell resistance with $BrCF_3$ delivery is consistent with decreased contact resistance as fluorine doping, and hence carrier concentration, increases. The dry cell resistance levels off at higher doping rates, consistent with a reduction in doping efficiency (despite additional fluorine incorporation). An alternative explanation might be roughening of the film, which could increase the contact resistance by reducing the contact area. Similar trends in resistivity have been reported [23] for this chemistry on glass substrates, and attributed to decreases

---

[xviii] Both values will be reported in each plot.

[xix] 98, 104, 93, and 90 sccm, in order of increasing $BrCF_3$ delivery rate.

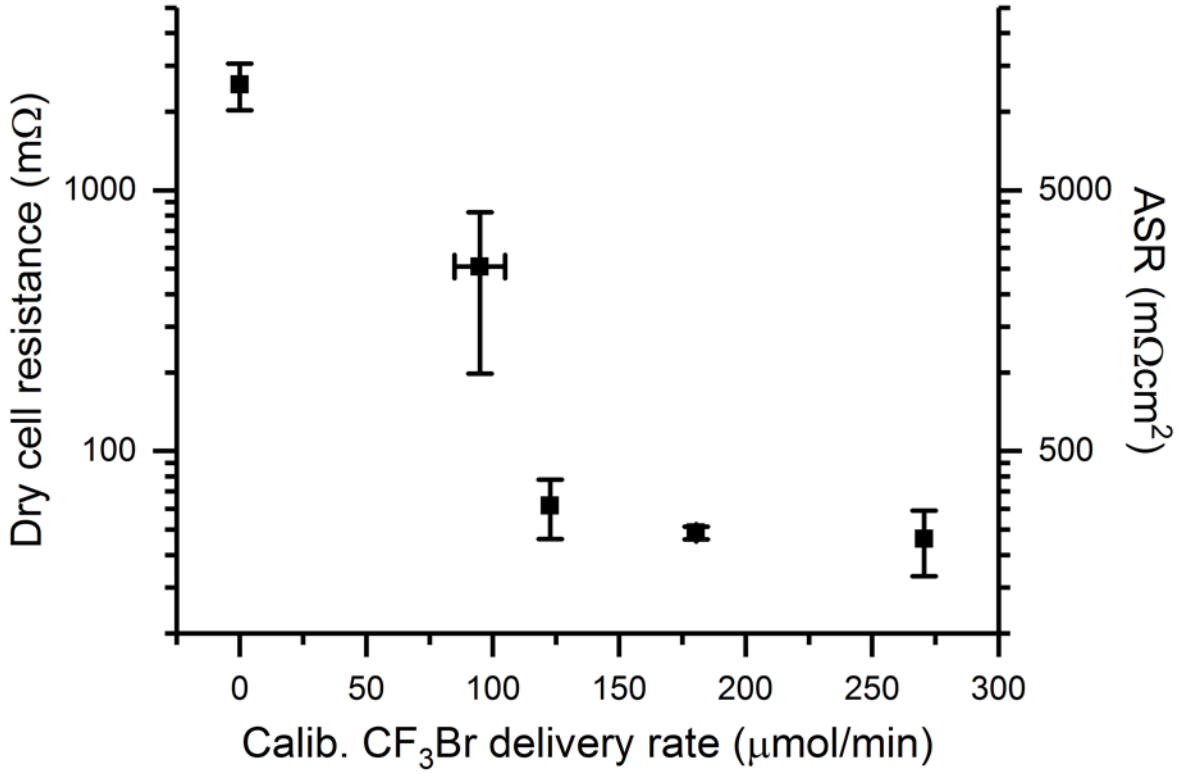

Figure 1.4.11: Plot of dry cell resistance vs. $BrCF_3$ delivery rate for samples deposited at 450 °C with 5.7 μmol/min TMT, 780 μmol/min oxygen, and purified nitrogen to reach a total flowrate of ca. 96 sccm. Data points are an average of three measurements; error bars are 95 % confidence intervals. Accuracy of $BrCF_3$ delivery is 100 μmol/min, but run-to-run variability is ca. 0.1 μmol/min, based on the commercial performance specifications.

in doping efficiency. When a deposition was performed on silicon thermal oxide under conditions mimicking those of the highest $BrCF_3$ delivery rate, the resulting film is rough and appears visibly cloudy by eye. By contrast, films deposited on thermal oxide wafers mimicking the lower $BrCF_3$ delivery rates appear smooth and mirror-like.

Figure 1.4.12: displays additional points representing 12- and 60-minute depositions. The 60-minute depositions show a similar trend to the 30-minute depositions over the range tested. At a delivery rate of ca. 120 μmol/min $BrCF_3$, the 60-minute depositions cover a ca. 30 mΩ range of dry cell resistances, or a factor of 2. If this reflects the real variability of the measurement (and of

the deposited films), a ca. 2-fold variation is sufficient to preclude the interpretation of smaller differences in resistance (e.g., at 180 µmol/min $BrCF_3$). With this in mind, the $BrCF_3$ delivery rates between ca. 120 and ca. 270 µmol/min are essentially equivalent. Even the 12-minute deposition (360 µmol/min), which seems distinct from the others, essentially overlaps within a factor of 2.

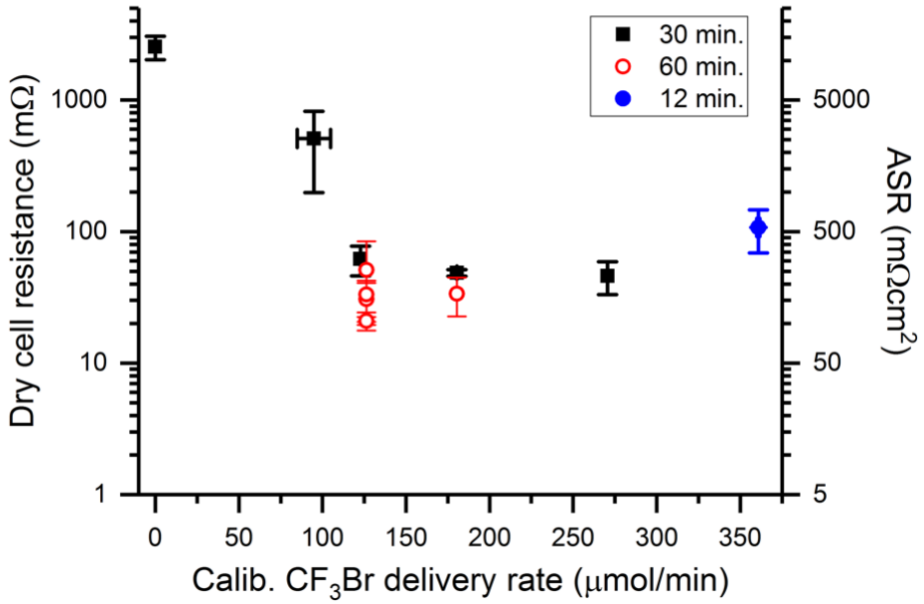

Figure 1.4.12: Plot of dry cell resistance vs. $BrCF_3$ delivery rate for samples deposited at 450 °C with 5.7 µmol/min TMT, 780 µmol/min oxygen, and purified nitrogen to reach a total flowrate of ca. 96 sccm. Data points are an average of three measurements; error bars are 95 % confidence intervals. Accuracy of $BrCF_3$ is 100 µmol/min, but run-to-run variability is ca. 0.1 µmol/min, based on the commercial performance specifications.

When the deposition temperature is increased to 468 °C, similar to slightly lower dry cell resistance values are measured. An increase in growth rate resulting in thicker films could result in reduced contact resistance, for the reasons described above. In the absence of additional data points in the range of 0 and 100 µmol/min at 450 °C, the potential for trend interpretation is limited—leveling off in dry cell resistance at high $BrCF_3$ delivery rates cannot be distinguished from a decrease. Figure 1.4.13 shows these measurements. Depositions were conducted at ca. 468 °C for either 30 or 60 minutes, under a flow of 780 µmol/min oxygen, and a 1.3, 2.6, or 5.7

μmol/min TMT delivery rate. The $BrCF_3$ delivery rate varied as indicated in Figure 1.4.13. The

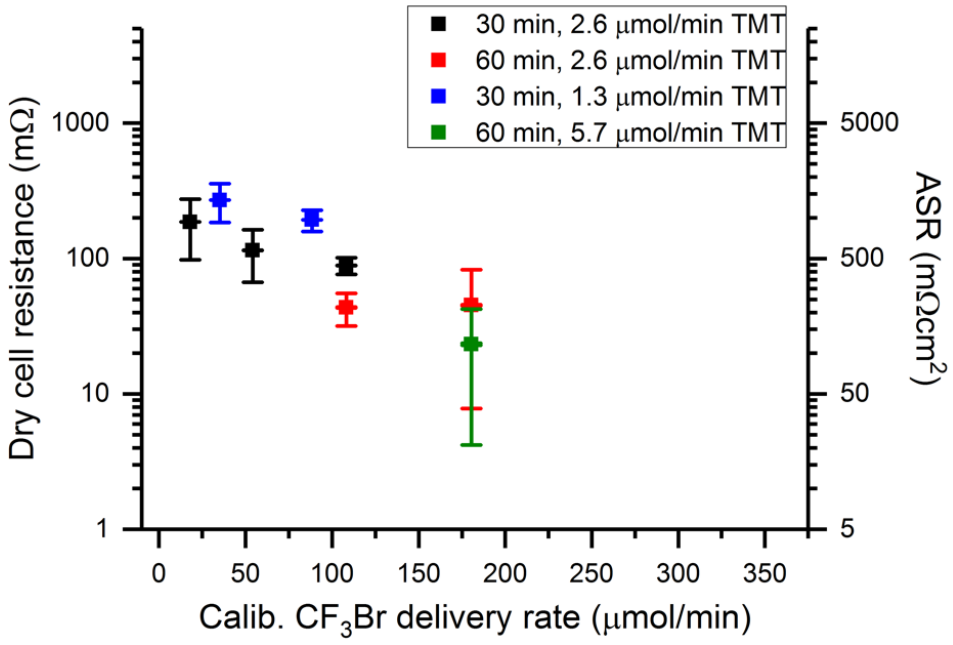

Figure 1.4.13: Depositions conducted at 468 °C for either 30 or 60 minutes, under a flow of 780 μmol/min (19 sccm) oxygen, and a 1.3, 2.6, or 5.7 μmol/min TMT delivery rate. The sample labeled 2.6 μmol/min TMT at 54 μmol/min CF_3Br is 2.7 μmol/min TMT, but was combined with the others for visual clarity. The flow of purified nitrogen flow was adjusted to achieve a total flow rate of 96 ± 2 sccm (standard deviation). Measurement was "full" dry cell measurement with Sigracet SGL 39aa carbon paper. The resistance shown for the sample deposited at 5.7 μmol/min TMT delivery rate is a single measurement, and the displayed error is the same percent error that of the point directly above. All other data points are averages of three measurements. Error bars are 95% confidence intervals.

flow of purified nitrogen flow was adjusted to achieve a total flow rate of 96 ± 2 sccm (standard deviation).[xx] While ca. a factor of 2 higher in dry cell resistance than graphite, a dry cell assembled with a SnO_2(F)-coated stainless steel flow plate is on par with the cell resistance of operating flow

[xx] standard deviation.

batteries.[xxi]

1.4.3 Chemical stability

To assess the chemical stability of SnO_2 and SnO_2(F) films,[xxii] representative films were immersed in an electrolyte of elevated, but realistic concentrations (3 M hydrobromic acid/1.5 M bromine solution) and kept at 58 °C for 14 weeks. The two samples were deposited at 448 ± 3 °C for 30 minutes under a flow of 5.7 μmol/min TMT, 0 or 123 μmol/min $BrCF_3$, 780 μmol/min (19 sccm) oxygen, and a balance of nitrogen to reach a total flow rate of 98 or 104 sccm. SnO_2(F) showed stable sheet resistance measurements over the course of the test. The sheet resistance of SnO_2 increased with time, potentially indicating a degradation of the film. These results are displayed in Figure 1.4.14.

SEM micrographs of pristine SnO_2 and SnO_2(F) and after 9.7 weeks of exposure to hot electrolyte are shown in Figure 1.4.15. The film appearance was similar at these two time points, and there is no indication of degradation. The sheet resistance and SEM data are consistent with a process that changes the resistivity of the material, without changing the appearance of the surface. If the strongly oxidizing environment of the heated electrolyte oxidizes the film, lowering the number of oxygen vacancies, the resistivity of the film would increase without dissolution. This process would not be expected to affect SnO_2(F), where the resistivity is set by the fluorine doping, rather than oxygen vacancies. The stability test results for the SnO_2(F) film are encouraging for

---

[xxi] To account for the difference in surface area (due to the existence of channels, rather than a flat plate), one can simply multiply the dry cell resistance value by the expected reduction in surface area. (i.e., half the area means double the resistance).

[xxii] Additionally, commercial SnO_2(F) (11.8 Ω/sq, supplier unknown) was immersed in pure bromine for two weeks. The appearance of the film by eye and SEM remained unchanged.

use of this material in corrosive environments.

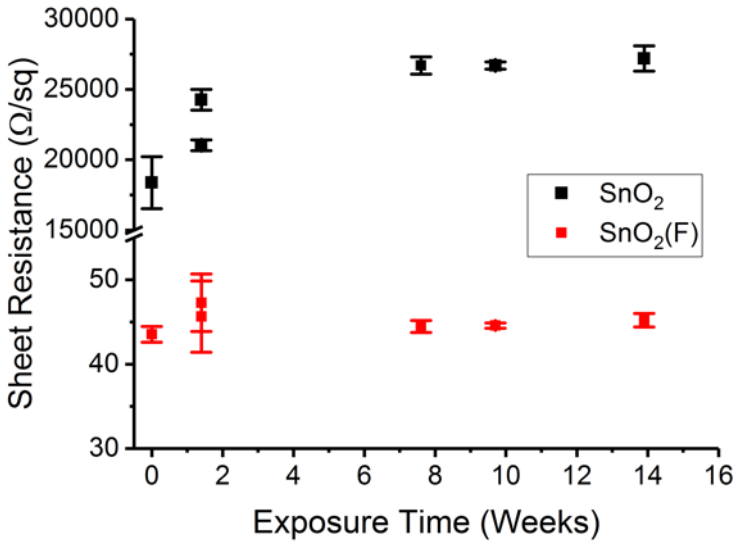

Figure 1.4.14: Sheet resistance of SnO_2 and SnO_2(F) films after heating to 58 °C in a 3 M HBr / 1.5 M Br_2 solution. SnO_2 and SnO_2(F) were deposited at 448 ± 3 °C for 30 minutes under a flow of 5.7 µmol/min TMT, 0 or 123 µmol/min $BrCF_3$, 780 µmol/min (19 sccm) oxygen, and a balance of nitrogen to reach a total flow rate of 98 or 104 sccm.

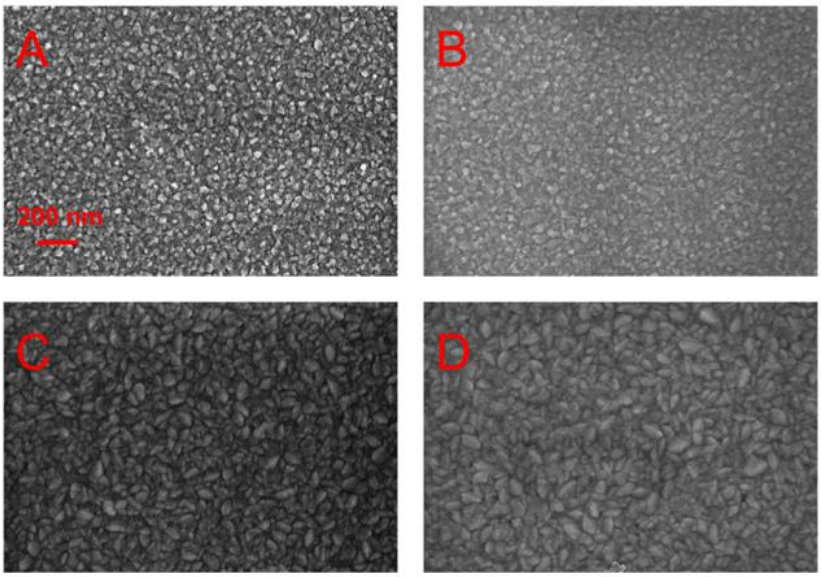

Figure 1.4.15: SEM micrographs of SnO_2 and SnO_2(F) (A, C) before exposure to heated electrolyte solution and (B, D) after exposure.

1.4.4 Film continuity

In addition to establishing that the coating material is resistant to electrolyte attack, a protective coating must be pinhole-free to be fully functional. Accordingly, the continuity of $SnO_2(F)$ films on silicon thermal oxide and stainless steel substrates was studied. Tests on thermal oxide evaluate the capacity of a deposition method to produce continuous films on a nearly atomically flat surface. If a process is not continuous on a smooth surface (assuming the continuity issues are not due to the chemistry of the surface), then it is unlikely to translate to continuous films on rough surfaces, e.g. stainless steel.

The continuity of films deposited on SiO_2 was assessed for 30-minute depositions at substrate temperatures of 450 and 468 °C. At 450 °C, the following four samples were deposited: two samples with zero $BrCF_3$ delivery and a 98-sccm total flowrate, one sample with 123-μmol/min $BrCF_3$ and 104-sccm total flow rate, and one sample with 180-μmol/min $BrCF_3$ and 93-sccm total flowrate. For all four depositions, 5.7 μmol/min TMT and 780 μmol/min oxygen were included, and a balance of nitrogen to reach the listed flow rate. At 468 °C, four samples were deposited as follows: for 1.3 μmol/min TMT, 36 or 72 μmol/min $BrCF_3$ was delivered and for 2.7 μmol/min TMT, 54 or 72 μmol/min $BrCF_3$ was delivered. For all four samples, 780 μmol/min oxygen and sufficient nitrogen were delivered to reach a total flow rate of 97 ± 1 sccm. The samples were exposed to 5:1 buffered oxide etch at room temperature for 10 minutes (450 °C samples) and 18 minutes (468 °C samples). No pinholes were visible on any samples after rinsing with de-ionized water and drying with nitrogen.

To test film continuity on SS substrates, four 30-minute depositions were performed at 450 °C, including the range of pinhole-free deposition conditions established above. All four samples were subjected to delivery rates of 5.7 μmol/min TMT and 780 μmol/min oxygen, and a balance

of nitrogen to reach a total flow rate of 98, 104, 93, and 90 sccm, respectively. $BrCF_3$ delivery rates were 0, 123, 180, and 270 µmol/min. These samples were treated with a drop of 20 % HCl / 5 % $FeCl_3$ solution that covered an area ca.1 inch in diameter. After 20 minutes, the samples were thoroughly rinsed in de-ionized water and dried with nitrogen. Figure 1.4.16 shows the resulting etch patterns.

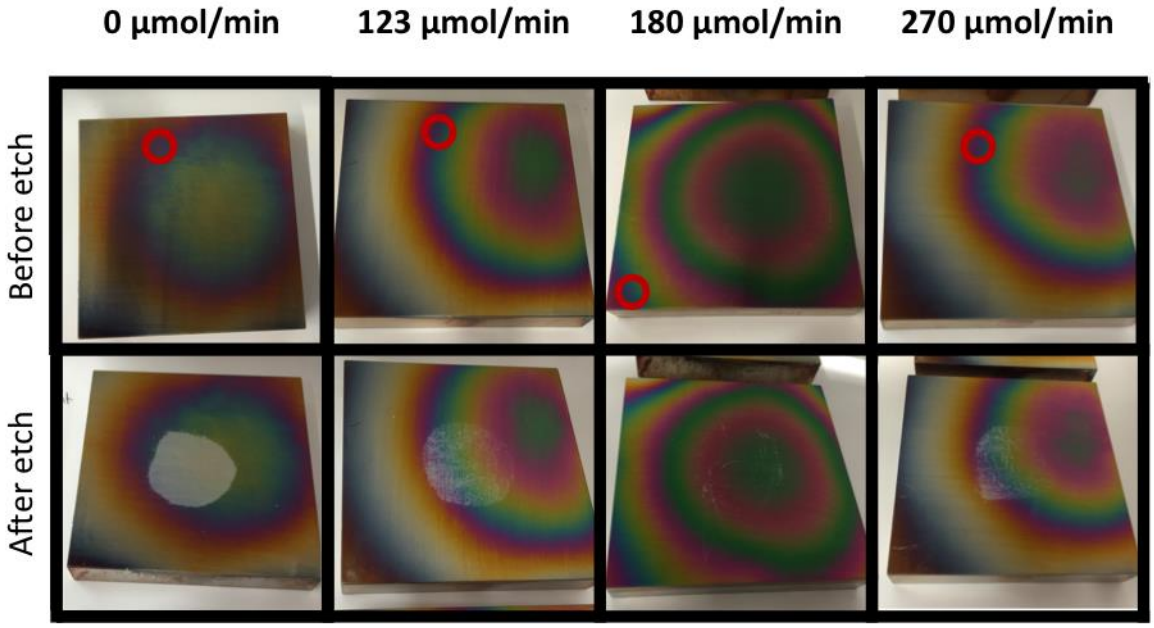

Figure 1.4.16: 30-minute $SnO_2(F)$ depositions on SS, subject to HCl/$FeCl_3$ etching. All samples were subject to delivery rates of 5.7 µmol/min TMT and 780 µmol/min oxygen, and an excess of nitrogen to reach a total flow rate of 98, 104, 93, and 90 sccm, respectively. $BrCF_3$ delivery rates are listed in the figure. Depositions were performed at ca. 450 °C. Depositions were 30 minutes in length. Open red circles denote fringes of approximately equal thickness.

The neat SnO_2 sample was fully etched in the drop location. The 123 and 270 µmol/min-samples were partially etched in all locations contacting the drop. The 180 µmol/min-sample was etched significantly less. Based on the colored interference fringes visible on the sample surfaces, the 180 µmol/min sample was the thickest, followed by the roughly equivalent 123 and 270 µmol/min-samples, and finally the neat SnO_2 sample. While a trend of increasing growth rate might be suggested by 450 °C depositions on SiO_2, sufficient variability in the film thickness has

been observed for other samples to obscure such a trend. Fringes of equivalent thickness are marked with open red circles in the diagram. In this case, an etch test in the center of the sample has sampled equivalent thicknesses for all but the 180 μmol/min-sample. Among samples of comparable thickness, the two higher $BrCF_3$ delivery rates had fewer pinholes. The middle two $BrCF_3$ delivery rates produced samples with the best combination of continuity and contact resistance (detailed in section 1.4.1.4), so 60 minute depositions were performed at 123 and 180 μmol/min $BrCF_3$ under otherwise identical conditions. Figure 1.4.17 and Figure 1.4.18 show images of the samples before and after a 40-minute $FeCl_3$/HCl etch (123-126 μmol/min $BrCF_3$ delivery rate) and a 20-minute etch (180 μmol/min $BrCF_3$ delivery rate). A few small pinholes were observed in the former sample at 20 minutes. As expected, fewer pinholes appeared in the

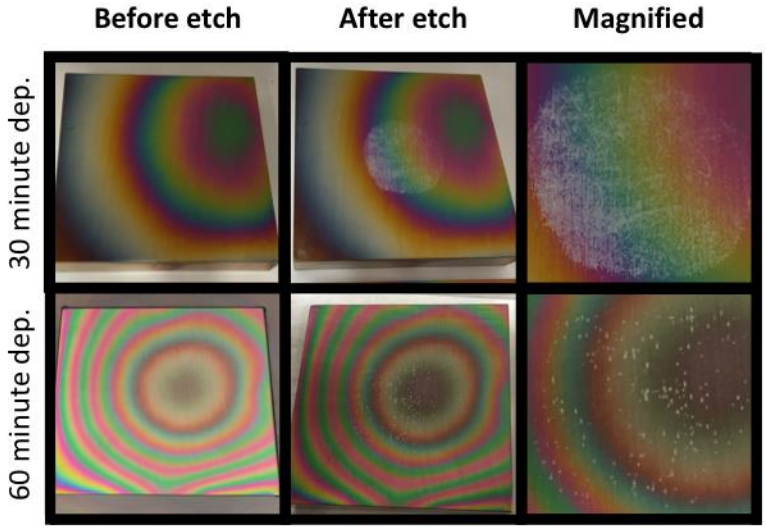

Figure 1.4.17: 30- and 60-minute SnO_2(F) depositions at 123 or 126 μmol/min $BrCF_3$, subject to HCl/$FeCl_3$ etching. All samples were subject to delivery rates of 5.7 μmol/min TMT, 780 μmol/min oxygen, and either 123 μmol/min (top images) or 126 μmol/min $BrCF_3$ (bottom images), and a balance of nitrogen to reach 99 ± 5 sccm at a temperature of 452 or 450 ± 2°C. Depositions were conducted at 30 minutes (top images) and 60 minutes (bottom images) in length.

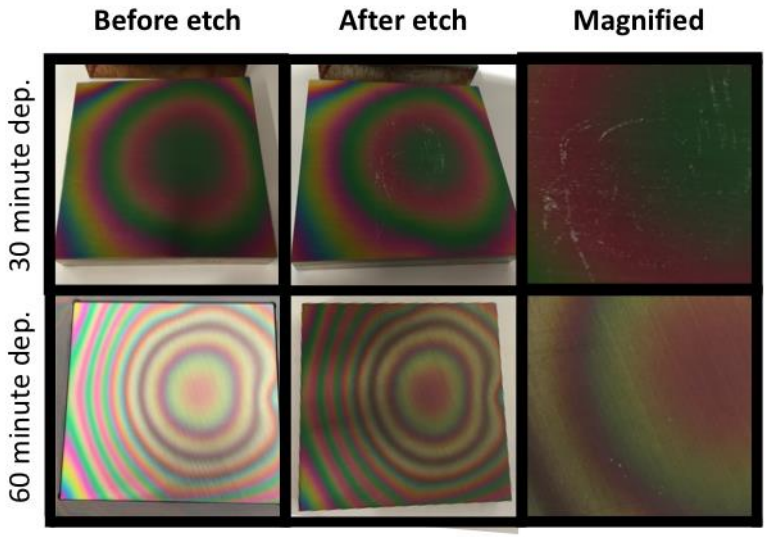

Figure 1.4.18: 30- and 60-minute $SnO_2(F)$ depositions at 180 µmol/min $BrCF_3$, subject to HCl/$FeCl_3$ etching. All samples were subject to delivery rates of 5.7 µmol/min TMT, 180 µmol/min $BrCF_3$, 780 µmol/min oxygen, and a balance of nitrogen to reach 93 sccm. Depositions were performed at 452 ± 2 °C and were 30 minutes (top images) and 60 minutes (bottom images) in length.

longer depositions. Surprisingly, with the exception of the 30-minute deposition with a 123 µmol/min $BrCF_3$ delivery rate, there was no obvious correlation between the number of pinholes and film thickness. This suggests that simply using a thicker film may not eliminate pinholes reliably.

Surface roughness appears to play a role in the appearance of pinholes on a coated substrate. This is likely due to modest conformality of films deposited on rough surfaces. Etch testing on a coated flow plate with channels illustrates this effect clearly. An interdigitated flow field (channels and landings ca 1mm wide) was milled into a 0.25″ thick stainless steel plate. The top surface of the plate was visibly rougher than typical precision ground SS substrates. The sides of the milled channels were very smooth due to the positioning of the drill bit. Completing each channel required a pass with the mill on each side, leaving two ridges running lengthwise along the bottom edges of the channel. Figure 1.4.19 illustrates these features.

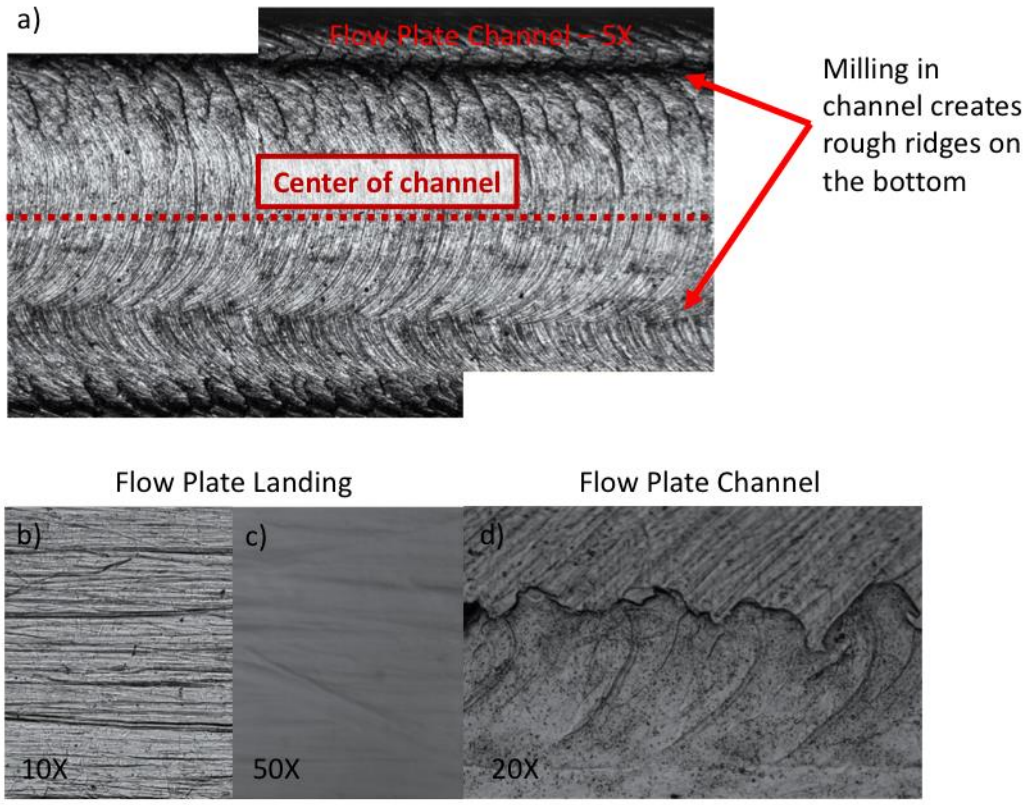

Figure 1.4.19: Optical microscope images of the channels and landings of an electropolished flow plate at different magnifications. (a) two optical microscope images, stitched together to show the full width of the channel, including ridges created by milling, (b),(c) the landing of the flow plate, and (d) a magnified image of the ridges created by milling.

When this plate was subjected to $FeCl_3$/HCl etching, no pinholes were observed on the sides of the channels, a moderate number were observed on the landings, and the ridges left by the end mill were etched (see Figure 1.4.20). This suggests that the level of smoothness achieved by the side of the end mill is sufficient for conformal films, and that the bottom of the channel, which is not accessible for polishing, must be dealt with specially. CVD processes are adept at covering low- to medium-aspect ratio surfaces, so the difficulty in continuously coating these regions implies that either a) there are high-aspect ratio features in these regions not visible by optical microscopy, or less likely, these particular features are challenging to clean fully, and hence contamination is impeding continuous coverage in these areas.

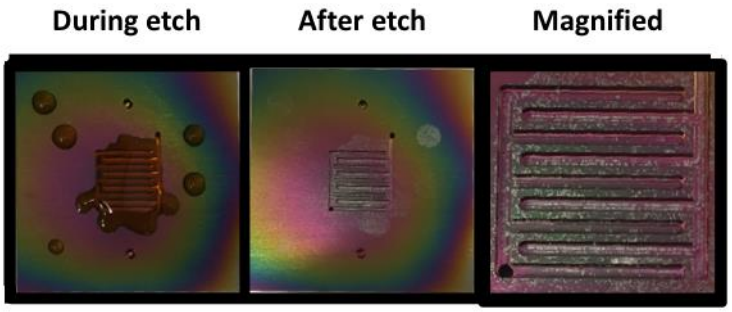

Figure 1.4.20: Etching of a flow plate with channels. Sample was deposited at 450 °C under a flow of 126 μmol/min $BrCF_3$, 5.7 μmol/min TMT, 780 μmol/min oxygen, and a balance of nitrogen to reach a total flow rate of 94 sccm.

To address the issue of surface roughness, a precision ground stainless steel plate was electropolished. Optical microscope images of the surface are shown in Figure 1.4.21. Some surface smoothing is evident, especially at 50× magnification. The electropolished stainless steel

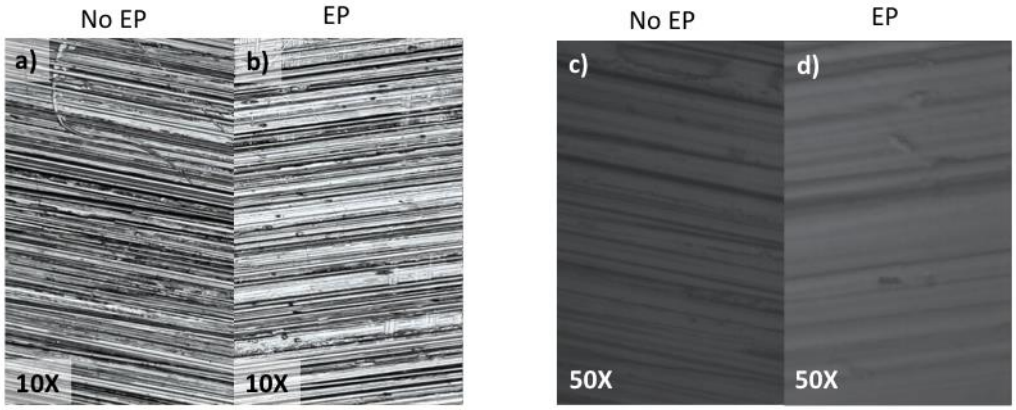

Figure 1.4.21: Optical microscope images comparing as-received precision ground stainless steel plates (a, c) and a similar plate after electropolishing (b, d).

substrate had a one-interface SS-Cu resistance of 1.8 ± 0.4 mΩ—a factor of 5 larger than that of an unheated SS plate. If electropolishing is to be used to smooth features, it is likely that a subsequent treatment will be required to remove the resulting oxide layer. The electropolished sample was coated at 450 °C under a flow of 180 μmol/min $BrCF_3$, 5.7 μmol/min TMT, 780 μmol/min oxygen, and a balance of nitrogen to reach a total flow rate of 102 sccm. An $FeCl_3$/ HCl

etch revealed pinholes (see Figure 1.4.22), suggesting that this electropolishing process alone is inadequate.

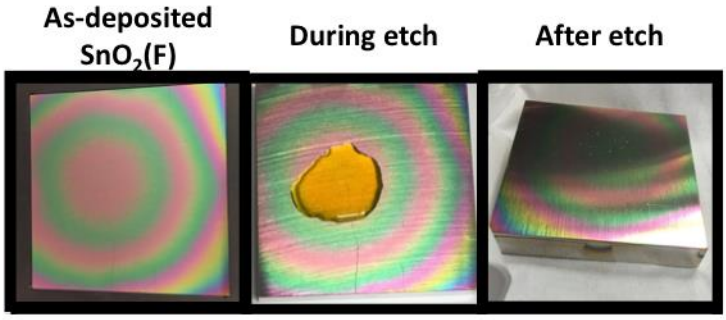

Figure 1.4.22: $HCl/FeCl_3$ etching of a $SnO_2(F)$-coated, electropolished stainless steel substrate. Deposition was conducted at 450 °C under a flow of 180 μmol/min $BrCF_3$, 5.7 μmol/min TMT, 780 μmol/min oxygen, and a balance of nitrogen to reach a total flow rate of 102 sccm.

Given the demonstrated corrosion-resistance of $SnO_2(F)$ in accelerated stability tests (see section 1.4.3), $SnO_2(F)$ is a promising protective coating. Further study of substrate smoothing methods, or ways of circumventing the milling issue[xxiii] are a logical next step in developing a satisfactory coating.

1.5 Conclusions

The widespread use of renewable energy like wind and solar power depends on the adaptation of the electric grid to the variability inherent in these sources. Redox flow batteries have the potential to smooth solar and wind output inexpensively and efficiently. Quinone-bromine flow batteries have inexpensive electrolyte materials, but bromine is highly corrosive, and damages graphite flow plates. $SnO_2(F)$-coated stainless steel substrates were prepared as a chemically stable

[xxiii] One can imagine, for example, drilling completely through a thinner flow plate to avoid the problematic ridge features. Electrical contact would be made directly with the plate, and a fluid seal could be established with a suitable gasket on the backside of the flow plate.

alternative to graphite. To assess the potential performance of these films, the ohmic resistance (via area-specific resistance), corrosion resistance, and continuity was studied.

Pinhole-free thin films of $SnO_2(F)$ were deposited on silicon thermal oxide using a variety of $BrCF_3$ delivery rates. Fluorine incorporation and a decrease in resistivity relative to neat SnO_2 were demonstrated. Consistent with a growth rate-dependent intermediate gas phase reactions, a decrease in thickness from the deposition center to the sample edge was observed. Stainless steel flow plates were coated, and the resistance contribution of the $SnO_2(F)$ and the individual interfaces of a mock flow battery were probed. The lowest ASR attained for a coated flow plate was 105 ± 7 $m\Omega \cdot cm^2$, at 450 °C, 5.7 μmol/min tetramethyltin, 126 μmol/min bromotrifluoromethane, 780 μmol/min oxygen, and nitrogen to reach a balance of 94 sccm. For reference, graphite flow plates in a similar cell measured 45 ± 11 $m\Omega \cdot cm^2$.

The dominant factor influencing cell area specific resistance (ASR) was the choice of carbon paper. The ASR measure for two nominally similar papers differed by as much as a factor of 8 for the highest dopant delivery rate tested, a factor of 6 for neat SnO_2, and ca. 2 for intermediate $BrCF_3$ delivery rates. Replacing the coated flow plate with a graphite flow plate yielded a factor of 3 difference in the ASR measured using the two carbon papers. The next largest source of resistance was the $SnO_2(F)$-carbon paper interface. This resistance can be reduced by increasing the $BrCF_3$ delivery rate, but the effect levels off above ca. 120 μmol/min for the considered depositions at 450 °C (the trend is less clear for depositions at 468 °C). The estimated total contribution of all other interfaces was small by comparison: 29 ± 6 $m\Omega \cdot cm^2$ vs. 150 ± 50 $m\Omega \cdot cm^2$ total ASR for a representative coated plate. Non-$SnO_2(F)$ contacting interfaces were estimated to contribute 25 ± 6 $m\Omega \cdot cm^2$ to the total measured ASR. While the ASR of the lowest-resistance coated plate is a factor of 2 greater than that of graphite, the contribution is still small compared to

the resistance of an operating flow battery cell.

Pinhole-free films were achieved on silicon thermal oxide substrates, but not for stainless steel plates with channels owing to roughness from the machining process. Due to the lack of pinhole-free films on stainless steel, the characterization of the film electrochemical stability on coated flow plates could not be assessed. The presence of even small exposed SS surface area would result in rapid corrosion, and the conflation of SS electrochemical reactions with those on the surface of SnO_2(F). To isolate the assessment of SnO_2(F) bromine and hydrobromic acid resistance from the impact of pinholes, chemical stability was determined using coated silicon thermal oxide substrates. A thin film of SnO_2(F) showed a stable sheet resistance and appearance (by SEM) during 14 weeks of exposure to a 58 °C solution of 3M hydrobromic acid and 1.5 M bromine. A similarly-exposed neat SnO_2 film was unchanged in appearance, but saw a 50 % increase in sheet resistance.

SnO_2(F)-coated flow plates are a promising substitute for graphite flow plates. If pinhole-free films can be achieved on a convenient substrate, then in operando tests can be performed, and further optimization can take place. The work of Park, et al. has demonstrated SnO_2(F) to be stable under electrochemical cycling in 1 M sulfuric acid.[19] The main limitation of the considered SnO_2(F) protective coatings is film continuity. Pinholes might be avoided by adequately smooth substrates, or a flow plate redesign. With these improvements, SnO_2(F)-coated could be a promising option for chemically resistant, conductive coatings in flow batteries and other applications.

References

1. Chen, Q., et al., *A quinone-bromide flow battery with 1 W/cm^2 power density*. Journal of the Electrochemical Society, 2015. **163**(1): p. A5010-A5013.

2. Dunn, B., H. Kamath, and J.M. Tarascon, *Electrical energy storage for the grid: A battery of choices*. Science, 2011. **334**(6058): p. 928-935.

3. Vaughan, A. *Time to shine: Solar power is fastest-growing source of new energy*. The Guardian [Online], Oct 4, 2017. https://www.theguardian.com/environment/2017/oct/04/solar-power-renewables-international-energy-agency. (accessed April 4, 2018)

4. Zhu, Y., K.A. Dunn, and A.E. Kaloyeros, *Properties of ultrathin platinum deposited by atomic layer deposition for nanoscale copper-metallization schemes*. Journal of Materials Research, 2007. **22**(05): p. 1292-1298.

5. Soloveichik, G.L., *Battery technologies for large-scale stationary energy storage*. Annual Review of Chemical and Biomolecular Engineering, 2011. **2**(1): p. 503-527.

6. Huskinson, B., et al., *A metal-free organic-inorganic aqueous flow battery*. Nature, 2013. **505**(7482): p. 195-198.

7. Zhang, M., et al., *Capital cost sensitivity analysis of an all-vanadium redox-flow battery*. Journal of the Electrochemical Society, 2012. **159**(8): p. A1183-A1188.

8. Huskinson, B., et al., *Novel quinone-based couples for flow batteries*. ECS Transactions, 2013. **53**(7): p. 101-105.

9. Huskinson, B., et al., *Cycling of a quinone-bromide flow battery for large-scale electrochemical energy storage*. ECS Transactions, 2014. **61**(37): p. 27-30.

10. Lin, K., et al., *A redox-flow battery with an alloxazine-based organic electrolyte*. Nature Energy, 2016. **1**(9): p. 16102-38.

11. Gerhardt, M.R., et al., *Anthraquinone derivatives in aqueous flow batteries*. Advanced Energy Materials, 2016. **7**(8): p. 1601488-14.

12. Beh, E.S., et al., *A neutral pH aqueous organic–organometallic redox flow battery with extremely high capacity retention*. ACS Energy Letters, 2017. **2**(3): p. 639-644.

13. Yang, Z., et al., *Alkaline benzoquinone aqueous flow battery for large-scale storage of electrical energy*. Advanced Energy Materials, 2017. **8**(8): p. 1702056.

14. Tong, L., et al., *UV-Vis spectrophotometry of quinone flow battery electrolyte for in situ monitoring and improved electrochemical modeling of potential and quinhydrone formation*. Physical Chemistry Chemical Physics, 2017. **19**: p. 31684-31691.

15. Axdal, S.H. and D.D. Chung, *Kinetics and thermodynamics of intercalation of bromine in graphite—I. Experimental*. Carbon, 1987. **25**(2): p. 191-210.

16. Gaier, J.R., N.F. Ditmars, and A.R. Dillon, *Aqueous electrochemical intercalation of bromine into graphite fibers*. Carbon, 2005. **43**(1): p. 189-193.

17. Widenkvist, E., et al., *Mild sonochemical exfoliation of bromine-intercalated graphite: a new route towards graphene*. Journal of Applied Physics D, 2009. **42**(11): p. 112003.

18. Brady, M.P., et al., *Manufacturing and performance assessment of stamped, laser welded, and nitrided FeCrV stainless steel bipolar plates for proton exchange membrane fuel cells*. International Journal of Hydrogen Energy, 2013. **38**(11): p. 4734-4739.

19. Park, J.H., B.J. Jeon, and J.K. Lee, *Electrochemical characteristics of fluorine-doped tin oxide film coated on stainless steel bipolar plates*. Surface and Coatings Technology, 2015. **277**: p. 1-6.

20. Chen, Z., et al., *Recent advances in tin dioxide materials: Some developments in thin films, nanowires, and nanorods*. Chemical Reviews, 2014. **114**(15): p. 7442-7486.

21. Gordon, R., *Chemical vapor deposition of coatings on glass*. Journal of Non-Crystalline Solids, 1997. **218**: p. 81-91.

22. Marikkannan, M., et al., *A novel synthesis of tin oxide thin films by the sol-gel process for optoelectronic applications*. AIP Advances, 2015. **5**(2): p. 027122.

23. Proscia, J. and R.G. Gordon, *Properties of fluorine-doped tin oxide films produced by atmospheric pressure chemical vapor deposition from tetramethyltin, bromotrifluoromethane and oxygen*. Thin Solid Films, 1992. **214**(2): p. 175-187.

24. Suh, S., et al., *Atmospheric-pressure chemical vapor deposition of fluorine-doped tin oxide thin films*. Thin Solid Films, 1999. **345**(2): p. 240-243.

25. Maruyama, T. and K. Tabata, *Fluorine-doped tin dioxide thin films prepared by chemical vapor deposition*. Journal of Applied Physics, 1990. **68**(8): p. 4282-4285.

26. Wang, J.T., et al., *Morphology control of fluorine-doped tin oxide thin films for enhanced light trapping*. Solar Energy Materials and Solar Cells, 2015. **132**(C): p. 578-588.

27. Suffner, J., et al., *Chemical vapor synthesis of fluorine-doped SnO_2 (FTO) nanoparticles*. Journal of Nanoparticle Research, 2009. **12**(7): p. 2579-2588.

28. Reddy, S.R. and A.K. Mallik, *UV absorption studies of undoped and fluorine-doped tin oxide films*. Thin Solid Films, 1986. **143**(2): p. 113-118.

29. Wang, J.T., et al., *Influence of preferred orientation on the electrical conductivity of*

fluorine-doped tin oxide films. Scientific Reports, 2014. **4**(1): p. 3679.

30. Zhou, Y., et al., *Vacancy defects and optoelectrical properties for fluorine tin oxide thin films with various SnF2 contents*. Journal of Applied Physics, 2018. **123**(2): p. 025706.

31. Martinez, A.I. and D.R. Acosta, *Effect of the fluorine content on the structural and electrical properties of SnO_2 and ZnO–SnO_2 thin films prepared by spray pyrolysis*. Thin Solid Films, 2005. **483**(1-2): p. 107-113.

32. Subba Ramaiah, K. and V. Sundara Raja, *Structural and electrical properties of fluorine doped tin oxide films prepared by spray-pyrolysis technique*. Applied Surface Science, 2006. **253**(3): p. 1451-1458.

33. Rakhshani, A.E., Y. Makdisi, and H.A. Ramazaniyan, *Electronic and optical properties of fluorine-doped tin oxide films*. Journal of Applied Physics, 1998. **83**(2): p. 1049-1057.

34. Huang, X., et al., *Preparation of fluorine-doped tin oxide (SnO_2:F) film on polyethylene terephthalate (PET) substrate*. Materials Letters, 2010. **64**(15): p. 1701-1703.

35. Canestraro, C.D., et al., *Strong inter-conduction-band absorption in heavily fluorine doped tin oxide*. Applied Surface Science, 2008. **255**(5): p. 1874-1879.

36. Pilkington. *Coating technology—Processes*. https://www.pilkington.com/en/global/about/education (accessed May 9, 2018)

37. Borman, C.G., *Reactive pathways in the chemical vapor deposition of tin oxide films by tetramethyltin oxidation*. Journal of the Electrochemical Society, 1989. **136**(12): p. 3820-3828.

38. Williams, K.R., K. Gupta, and M. Wasilik, *Etch rates for micromachining processing-part II*. Journal of Microelectromechanical Systems, 2003. **12**(6): p. 761-778.

39. Rao, P.N. and D. Kunzru, *Fabrication of microchannels on stainless steel by wet chemical etching*. Journal of Micromechanics and Microengineering, 2007. **17**: p. N99-N106.

40. Fadavieslam, M.R., H. Azimi-Juybari, and M. Marashi, *Dependence of O_2, N_2 flow rate and deposition time on the structural, electrical and optical properties of SnO_2 thin films deposited by atmospheric pressure chemical vapor deposition (APCVD)*. Journal of Materials Science: Materials in Electronics, 2015. **27**(1): p. 921-930.

2 Stability and performance of metal nitride protective flow plate coatings and other flow battery components

2.1 Chapter abstract

Inexpensive, efficient energy storage technology could be instrumental to the widespread implementation of solar and wind energy. Flow batteries based on bromine/hydrobromic acid electrolytes have the potential to meet this need, but the destruction of crucial components–flow plates, proton exchange membranes, and carbon paper electrodes–limits the practical lifetime of such devices. Accordingly, the efficacy of protective metal nitride flow plate coatings and the stability of membranes and carbon paper electrodes was assessed. Physical vapor deposition of V(N,O) and Ti(N,O), chemical vapor deposition of V(N,C), and atomic layer deposition of W(N,O,C) were used to coat stainless steel plates, glass, and silicon thermal oxide wafers. An initial screening of dry cell resistance and area specific resistance was performed for commercially available Entegris sealed graphite flow plates and stainless steel plates coated with PVD V(N,O), CVD V(N,C), PVD Ti(N,O), commercial Ti(N,O), and ALD W(N,O,C). All films had dry cell resistances below that of SnO_2(F), except commercial Ti(N,O). A second screening exposed test films deposited on SiO_2 and/or glass to pure bromine and concentrated hydrobromic acid at room temperature. Only CVD V(N,C) showed no evidence of degradation. The relative resistance of V(N,C) to ca. 2-week bromine exposure appears related to the elemental carbon content of the film. CVD V(N,C)-coated silicon, Entegris flow plates, carbon paper electrodes, and Nafion membranes were immersed in a 3 M bromine/1.5 M hydrobromic acid electrolyte

solution at 58 °C for 25 days to 14 weeks. Flow plates and carbon paper showed stable ASR throughout the test. Conductivity measurements of Nafion membranes showed high variability over 10 weeks, but significant degradation was not evident. Finally, the V(N,C) film was etched completely. The considered metal nitride films therefore have insufficient chemical resistance for use as protective flow plate coatings, and Entegris flow plates are the best candidate for immediate use with bromine/hydrobromic acid electrolytes.

2.2 Introduction

The expense and convenience of flow batteries as grid-scale energy storage are impacted by the lifetime of key or expensive components. Replacing the flow plates, carbon paper electrodes, or proton exchange membrane requires disassembly of the cell—minimally an inconvenience, and potentially expensive, depending on the maintenance time required and the cost of replacement parts. As discussed in Chapter 1, the stability of flow battery components to bromine and hydrobromic acid exposure must be addressed if this chemistry is to be employed in a commercial setting. In this chapter, the chemical stability and contact resistance of a selection of transition metal nitride protective flow plate coatings and a commercially-available pyrolytically sealed graphite plate are considered. The stability of the carbon paper electrodes and proton exchange membranes to bromine-based electrolyte exposure is also studied.

A conductive coating that is pinhole-free and resistant to bromine and hydrobromic acid can prevent damage to battery flow plates and permit economically feasible battery lifetimes. Transition metal nitrides are a promising class of materials: usually stable in acid except at high concentrations, and metallic in character with high conductivities approaching that of their pure metal counterparts.[1] For example, VN, WN, and TiN have reported resistivities[2] of 25, 9, and

85 μΩ·cm—comparable or superior to SnO_2(F) (ca. 10^2-10^3 μΩ·cm[3, 4]).

Physical or chemical vapor deposited coatings offer a rapid, convenient method of screening a variety of metal nitride films for contact resistance and stability to electrolyte exposure. Based on their encouraging conductivities and capacity for rapid implementation (to permit efficient screening), VN, WN, and TiN coatings were selected for fabrication. VN, WN, and TiN, and indeed most metal nitrides, can be synthesized by treating metal chlorides with ammonia or a nitrogen/hydrogen mixture, or nitriding metal, metal hydride, or metal oxide powders.[1] Common thin film deposition methods include CVD[5-7] and magnetron sputtering.[8-11] In this work, oxygen-containing VN, designated V(N,O), was deposited by magnetron sputtering under substrate bias in a nitrogen atmosphere and carbon-containing VN, similarly designated V(N,C), was deposited by chemical vapor deposition with ammonia and tris(*N*,*N*′-diisopropylformidinato)vanadium(III). W(N,O,C) was deposited by ALD, and Ti(N,O) was deposited by reactive magnetron sputtering under substrate bias. Two deposition methods were selected for VN to afford films with different impurity compositions (e.g., PVD V(N,O) vs. CVD V(N,C)).[i]

Potential coatings were screened for adequate ASR, chemical stability, and film continuity. An initial screening of ASR was performed for commercially available Entegris sealed graphite flow plates and stainless steel plates coated with PVD V(N,O), CVD V(N,C), PVD Ti(N,O), commercial Ti(N,O), and ALD W(N,O,C). All films showed acceptable ASR, except commercial Ti(N,O). A second screening exposed test films deposited on SiO_2 and/or

[i] The literature often refers to metal nitrides with substantial carbon or oxygen impurities as simply "nitrides". Because the presence of these elements may impact the chemical stability of the considered films, I list all elements present in a given film.

glass to pure bromine and concentrated hydrobromic acid at room temperature. Only CVD V(N,C) showed no change in appearance or sheet resistance. CVD V(N,C), Entegris flow plates, carbon paper electrodes, and Nafion membranes were subjected to further stability tests. Entegris flow plates and carbon paper showed no appreciable change in ASR after immersion in in typical electrolyte at 58 °C for two months. CVD VN dissolved fully during 14 weeks of exposure. Nafion membranes showed a substantial variability in conductivity measurements, however, catastrophic degradation was not observed. Owing to adequate corrosion resistance and a low contribution to the total resistance of the flow battery cell, Entegris flow plates are the best candidate for immediate use with bromine/hydrobromic acid electrolytes.

2.3 Materials and methods

2.3.1 Deposition of metal nitride films

2.3.1.1 Chemical vapor deposition of V(N,C)

Films of V(N,C) were deposited by chemical vapor deposition (CVD) by Xian Gong and Dr. Jun Feng (graduate students of Prof. Roy Gordon at Harvard when this work was completed), using a deposition system that will be detailed in the thesis of Mr. Gong (in preparation). The vanadium source was a new precursor tris(*N*,*N*′-diisopropylformidinato)vanadium(III), abbreviated $V(iPr_2FMD)_3$. The preparation method was similar to the acetamidinate congener.[12] Depositions were conducted under two sets of conditions: a substrate temperature of 285-297 °C, a flow of 100 sccm each of ammonia and $V(iPr_2FMD)_3$ in nitrogen, or a substrate temperature of ca. 325 °C, a flow of 20 sccm ammonia, and 100 sccm $V(iPr_2FMD)_3$ in nitrogen. The sample deposited on glass under the former conditions is labeled V(N,C)-1. The samples

deposited on silicon thermal oxide and stainless steel (in a single run) under the latter conditions are labeled V(N,C)-2. $V(iPr_2FMD)_3$ vapor was carried by nitrogen flowing through a heated glass bubbler (ca. 120 °C) containing the precursor. Substrates were silicon wafers with a 300-nm oxide layer grown by wet oxidation, 1 mm thick microscope slides, or 316 stainless steel pieces (TCI America via McMaster-Carr). The wafers and glass were cut into ca. 0.5″ to 1″ pieces, and treated with UV-ozone for 5 minutes immediately before loading. Stainless steel substrates were cleaned before deposition by sonicating for 30 minutes in toluene (BDH, ACS grade), isopropanol (BDH, ACS grade), acetone (semiconductor grade, 99 %), and finally isopropanol (semiconductor grade, 99 %). Upon removal from the final isopropanol bath, the pieces were rinsed with semiconductor grade isopropanol, dried with nitrogen and immediately loaded into the deposition chamber. Dr. Feng used XPS survey scans to assess composition: V(N,C)-1 had 48 at. % V, 37 at. % N, and 15 at. % C and a sample deposited under the same conditions as V(N,C)-2 had 46 at. % V, 35 at. % N, and 20 at. % C. Dr. Feng's analysis method excluded oxygen because the counts on the sample surface were similar to that of a Si sample after sputtering away surface contaminants. This method assumes that a fresh Si surface exposed to an oxygen-containing XPS chamber will form an oxide layer or adsorb oxygen at the same rate as a fresh VN surface. There is no evidence to support this assumption—therefore, we cannot certify that the film has less than ca. 5 at. % oxygen.

2.3.1.2 Physical vapor deposition of titanium nitride

The assistance of Dr. Christine Zgrabik (a graduate student of Prof. Evelyn Hu at Harvard when this work was completed) in magnetron sputtering of Ti(N,O) is gratefully acknowledged. The development of the Ti(N,O) deposition methods listed below were guided by her experience with Ti(N,O) depositions in the sputtering system used in this work.[10, 11] This instrument is

an AJA magnetron sputtering system (model ATC) containing 6 shuttered magnetron guns (3 RF, 3 DC), mass flow controllers for argon, nitrogen, and oxygen (all gases are of purity 99.999 %), a turbo-pumped main chamber capable of attaining low 10^{-8} Torr vacuum levels, a load lock, and optional substrate bias. Deposition of Ti(N,O) films was accomplished by RF sputtering of a 2″ Ti(N,O) sputtering target at a power of 150 W, under a substrate bias of 93 ± 5 V.[ii] Depositions were conducted at a base pressure of 2.1 to 10. × 10^{-8} Torr.

Titanium readily reacts with oxygen, and thus low system base pressure is crucial to minimizing oxygen incorporation. To minimize the introduction of impurities during sample loading, the load lock was pumped to ca. 0.8 to 2 × 10^{-7} Torr. With a lengthy (multi-hour) pump down, pressure can be reduced to ca. 7 × 10^{-8} Torr, but this procedure was not feasible in practice. Two limits are imposed on the reduction of oxygen in this system. First, targets are changed once per week, and the system requires ca. 4 days to reach the maximum acceptable base pressure (ca. 3 × 10^{-8} Torr). The base pressure often remains near this level due to continual contamination from the load lock and oxide depositions by other users. Second, argon and nitrogen gases are used as received; in a highly oxygen-sensitive deposition, oxygen impurities in working gases may be sufficient to prevent the deposition of a pure nitride film.[iii] In this work and by Dr. Zgrabik's report, the most pure Ti(N,O) films still contain ca. 8 at. % oxygen by XPS.

[ii] The range is due to run-to-run variation in the applied voltage when 8 W bias current is applied (the bias voltage is controlled by setting a desired power).

[iii] For a 99.999% pure argon source and a chamber operating at 4 mTorr, impurities are ca. 4 × 10^{-8} Torr—roughly the magnitude of the system base pressure. The argon atmosphere in the deposition chamber is continually replenished, and consequently the impurities are supplied continuously also. It is well known that reactive metal surfaces are fouled in seconds or minutes at these pressures. Assuming film with a sticking coefficient of 1 in a chamber at a base pressure of 4 × 10^{-8} Torr, the entire surface would be covered by adsorbed impurities in about 20 minutes.

Substrates were silicon wafers with a 300-nm oxide layer grown by wet oxidation or 3″ × 3″ × 0.038″ 316 stainless steel pieces. The wafers were cut into ca. 1-3″ pieces, and rinsed with acetone (BDH, semiconductor grade, 99 %), then isopropanol (BDH, semiconductor grade, 99 %), and dried with nitrogen immediately before loading. Stainless steel substrates were cleaned before deposition by sonicating for 30 minutes in toluene (BDH, ACS grade), isopropanol (BDH, ACS grade), acetone (BDH, semiconductor grade, 99 %), and finally isopropanol (semiconductor grade, 99 %). Upon removal from the final isopropanol bath, the pieces were rinsed with semiconductor grade isopropanol, dried with nitrogen, and immediately transported to the clean room. A final semiconductor grade isopropanol rinse was performed immediately before loading the substrate into the deposition chamber.

2.3.1.3 Physical vapor deposition of vanadium nitride

In same sputtering system used for Ti(N,O), V(N,O) films were deposited by reactive RF or DC sputtering of a 2″ V sputtering target at a power of 248 W, under a substrate biases of ca. 0, 100, 150, and 200 V. Depositions were conducted at base pressures ranging from 0.6 to 2.2 × 10^{-8} Torr. Exceptionally poor system base pressures were lowered by ca. 100 or 150 W RF sputtering of titanium metal onto either an empty sample holder, or a movable cover designed to mask samples during depositions. Substrates were sourced and prepared identically to Ti(N,O) depositions.

2.3.1.4 Atomic layer deposition of WN

W(N,O,C) films (40 nm thick, 180 cycles) were deposited by Dr. Xiaobing Lou with an atomic layer deposition (ALD) system and deposition procedure developed by Dr. Xinwei Wang and Dr. Harbing Lou of the Gordon research group at Harvard University, following a previously

described recipe.[13] The tungsten and nitrogen sources were bis(tert-butylimido)bis(dimethylamido)tungsten(VI) and ammonia, respectively. The substrate and W precursor bubbler were held at temperatures of 385 °C and 75 °C, respectively. Substrates were sourced and prepared identically to CVD V(N,O) depositions.

2.3.2 Dry cell resistance measurements

The contribution of coated stainless steel substrates to the dry cell resistance was estimated using the dry cell resistance (DCR) test described in Chapter 1. A schematic of this set up is reproduced in Figure 2.3.1.

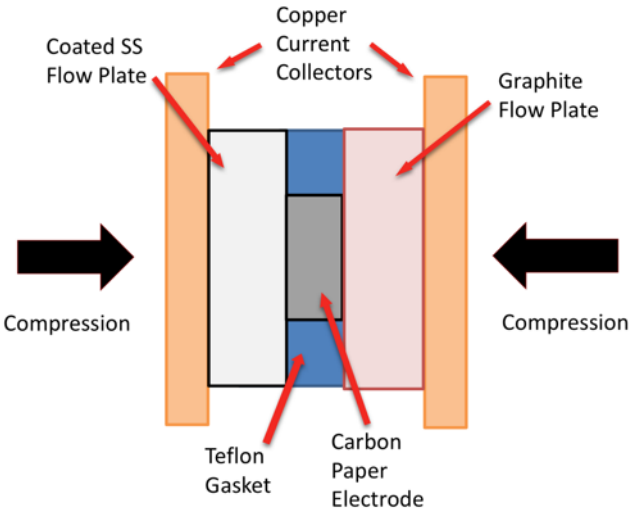

Figure 2.3.1: ASR "dry" cell set-up. Connection to the potentiostat is made through copper current collectors. A pair of electrically isolated stainless steel plates is used to compress the assembly, ensuring good electrical contact between the plates and the electrode.

Because CVD V(N,C) and ALD W(N,O,C) films were limited by reactor geometry to depositions on 1″ substrates, 2 cm^2 SGL 39aa carbon paper electrodes (of identical material and preparation) were used in place of 5 cm^2 electrodes. The coated plate was smaller than the current collectors or opposing graphite plate; the use of a torque wrench resulted in uneven, over-tightening of bolts, damaging the electrode and producing inconsistent measurements. Thus, the

cell was finger-tightened during these measurements. Any impact on DCR from finger tightening (which errs on the side of under-tightening bolts) is expected to increase, not decrease the measured resistance. Hence, resistances and ASR values reported for CVD V(N,O) and ALD W(N,O,C) are considered upper bounds on the expected dry cell resistance for a full-sized plate. NB: The expected graphite half-cell correction can be estimated as 5/2 times 4.5 ± 1.3 mΩ (the ratio of the electrode areas times the value for a graphite half-cell with 5 cm^2 electrodes, reported in Chapter 1).

2.3.3 Physical properties of V(N,O), V(N,C), Ti(N,O), and W(N,O,C) films

Film morphology was determined via scanning electron microscopy (SEM) micrographs. All SEM micrographs were collected using a Zeiss Supra 55 scanning electron microscope. The thickness of samples on SiO_2 substrates was ascertained by either analyzing a freshly-cleaved cross-section surface by SEM, or modeling film thickness by X-ray reflectometry (XRR) scans. X-ray reflectometry scans were collected using a θ-2θ scan a Bruker D8 Discover in XRR/HRXRD mode. Scans were performed using Cu Kα (λ = 1.542 Å) radiation, an increment of 0.01 degrees, and a typical scan range of ca. 0.2 to 10. degrees. Interference between reflections from the surface and film-substrate interface cause oscillations (called Kiessig fringes) in the XRR intensity with varying 2θ.[14] These fringes were used to calculate film thickness and density. From the film thickness and deposition time, the average growth rate was calculated.

More sophisticated modeling is required to obtain the film density from XRR patterns. The film-substrate density contrast and Brewster's angle influence the oscillation amplitude and the shape of the intensity plot at low 2θ. The surface and film-substrate interface roughness influence the rate of reduction in the oscillation amplitude and average intensity at higher 2θ

angles. Where a density estimate was desired, film thickness, film density, and surface and interface roughness were modeled together using simulations in DIFFRAC^{plus} LEPTOS 7 software. The silicon thermal oxide layer atop the silicon substrates was sufficiently thick to be approximated as an infinitely thick substrate. A density of 2.65 g/cm^3 was assumed for the density of SiO_2, as per the instrument database.

To assess the sensitivity of the model to variations in the allowed ranges of these parameters, the model was re-fit with different initial conditions for film thickness and density, and expanded parameter ranges (covering physically reasonable values) for each of these parameters in succession. The reported density and thickness values are from the most stable fits obtained. To validate the results of the model, a variation of the Bragg equation was used to calculate film thickness from that spacing of the Kiessig fringes.[15] Thickness estimates from this modified Bragg method and modeling were in good agreement.

Sample compositions were measured by XPS using a Thermo Scientific K-Alpha spectrometer with a 12 kV electron beam and a monochromatized Al Kα X-ray source (1486.7 eV). Surface cleaning was performed in situ with monatomic argon sputtering (2 keV, unless otherwise noted). To hold the sample in place and establish electrical contact between the sample stage and the film, a copper clip pressed onto the surface of the film. The center of each sample was targeted for analysis, and the clip was placed close to the region of interest. Elemental compositions were determined using high resolution scans performed in the energy ranges relevant to elements of interest. An energy resolution of 0.1 eV, a pass energy of 50 eV, and an average of 10 scans per element were used. The C1s, O1s, V2p, and N1s peak areas were fitted with a “Smart” background and the built-in instrument calibrations were used for element quantification.

2.3.4 Stability of V(N,O), V(N,C), Ti(N,O), and W(N,O,C) films

The chemical stability of V(N,O), V(N,C), Ti(N,O), and W(N,O,C) films was assessed through two types of extended electrolyte exposure. In the first type of test, films deposited on glass (CVD V(N,C)) or silicon thermal oxide (all others) were submerged for two weeks in a sealed container filled with either pure bromine (Aldrich, reagent grade) or concentrated hydrobromic acid (Fluka, purum, >48 %). The appearance of samples before and after exposure was monitored by eye in all cases. The sheet resistance and/or appearance by SEM micrographs was recorded before and after exposure for select samples. Sheet resistance was measured with a four-point probe (FPP-5000 Automatic Resistivity Meter).

In the second type of test, a CVD V(N,C)-coated silicon oxide wafer piece was submerged at 58 ± 2 °C in an electrolyte solution of elevated, but realistic operating concentrations of 1.5 M bromine and 3 M hydrobromic acid (Fluka, purum, >48 %). For the first 10 days, the sample and electrolyte were enclosed in a glass pressure vessel with Teflon seals. Subsequently, condenser was used to minimize bromine and hydrobromic acid loss to the atmosphere. A diagram of this set-up is shown in Figure 2.3.2. The piece was subjected to bromine/hydrobromic acid exposure and heat for over two months, as described above. Periodically, the sample was removed, washed with de-ionized water, and the sheet resistance was measured.

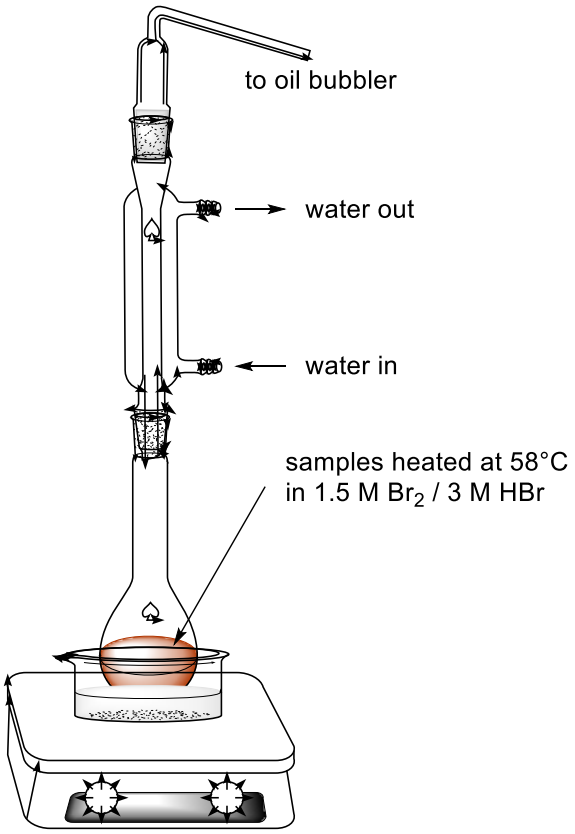

Figure 2.3.2: The reflux system used to enclose the samples and electrolyte solution during heating tests.

2.3.5 Flow plate, carbon electrode, and membrane stability tests

Two 2″ × 2″ × 0.25″, pyrolytically sealed, flat graphite plates (Entegris) were immersed in heated electrolyte as described above, for two months. A condenser and vessel similar to that of Figure 2.3.2 was used. To monitor plate stability, dry cell resistance measurements were performed periodically. Upon removal for testing, the samples were soaked in de-ionized water for 24 hours and dried in air. The dry cell resistance of each plate was measured three times (see Figure 2.3.1), and the values for both plates were averaged. Error bars are 95 % confidence intervals.

A set of Sigracet SGL 39aa carbon paper electrodes were exposed to heated electrolyte

for 25 days, using the same vessel as the graphite plates. A standard pretreatment was performed before immersion or, for pristine samples, before resistance measurements: a 24-hour bake at 400 °C. A custom-made, rigid, porous Teflon case with slots for individual carbon paper pieces was used to enclose the test pieces. This prevented cracking, compression, and other incidental mechanical damage to the papers during immersion and removal. Upon removal for testing, the samples were soaked in de-ionized water for 24 hours and dried in air. Each piece was used in a dry cell ASR/DCR measurement with two graphite plates. The average and 95 % confidence interval of the resulting average ASR/DCR for 4 pristine electrodes was compared with that of 3 electrolyte-exposed pieces.

The stability of Nafion 212 membranes was evaluated by monitoring the in-plane conductivity throughout 1.5 months of soaking in heated electrolyte in a condenser and vessel similar to that of Figure 2.3.2. At each time point, a new membrane was removed from solution and soaked in DI water for at least two days before testing. The conductivity experiment set-up is shown in Figure 2.3.3.

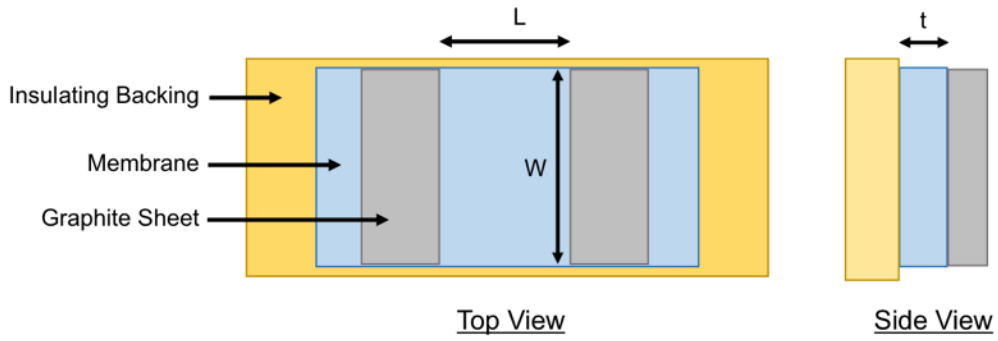

Figure 2.3.3: Membrane conductivity set-up. The labeled membrane dimensions are the distance between the graphite sheets (L), the length of width of the membrane strip (W), and the membrane thickness (t).

A rectangular piece of membrane was dipped in de-ionized water and laid across an insulating backing, and two small graphite rectangles (separated horizontally by 5 to 10 mm)

were placed on top of the membrane. The assembly was clamped together, and electrical contact was made with each of the graphite pieces. The assembly was enclosed in a container partially filled with de-ionized water, and measured when the membrane humidity has equilibrated (ca. 24 hours). Potentiostatic EIS measurements are then made using the graphite contacts. The inverse of the resulting resistance can be multiplied by the quantity $\frac{L}{Wt}$ to calculate the in-plane conductivity. The labeled membrane dimensions are the distance between the graphite sheets (L), the length of width of the membrane strip (W), and the membrane thickness (t). The former two values were measured with a micrometer, and the latter was taken from the supplier-provided membrane specifications.

2.4 Results and discussion

2.4.1 Magnetron sputtering of Ti(N,O) and V(N,O)

Titanium oxy-nitride was deposited by magnetron sputtering of stoichiometric TiN under a ca. 100 V substrate bias. This deposition process and the impact of parameter manipulation has been explored in depth by Dr. Christine Zgrabik.[10, 11] Consistent with her reports for films deposited under similar conditions, films vary in oxygen content from ca. 9-12 at.%, and are approximately 1:1 in titanium to nitrogen abundance. The expected deposition rate, based on her observations, is approximately 0.7 nm/min. Oxygen-free TiN was never achieved, likely due to residual oxygen or water contamination in the deposition chamber and the high reactivity of titanium with both contaminants. Table 2.4.1 (in the next section) lists the compositions and select deposition details for a representative set of titanium, vanadium, and tungsten-based nitrides films.

Reactive sputtering of V(N,O) from a vanadium target and nitrogen atmosphere was

performed under a variety of substrate bias voltages and nitrogen delivery rates. For all depositions, the working pressure was 4 mTorr and the total flow rate of the working gas was 40 sccm. Nitrogen concentration varied from 0 to 50 mol % of the working gas, with the balance being argon. Films were produced using either RF sputtering at 150 W, or DC sputtering at 250 W. Film compositions varied from nearly pure VN with 3 at. % oxygen to vanadium oxy-nitride with ca. 22 at. % oxygen, with some dependence of oxygen content on substrate bias. SEM micrographs of a subset of films, deposited at 50 mol % nitrogen, ca. 100 V substrate bias, and either RF or DC sputtering are displayed in Figure 2.4.1. Substrate bias appears to have no

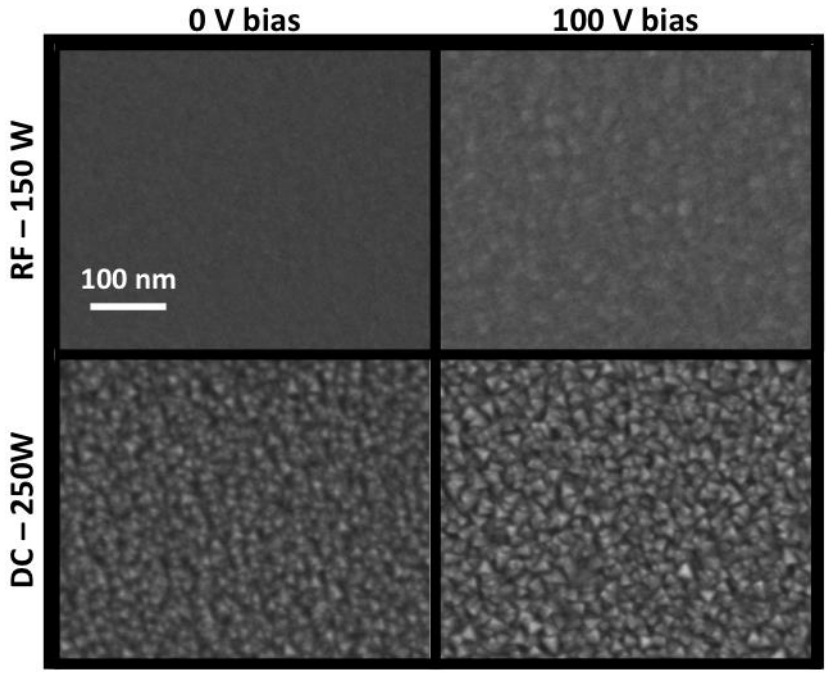

Figure 2.4.1: SEM micrographs displaying morphological variation in V(N,O) films with varying bias voltage and either RF or DC sputtering. Films displayed are V(N,O)-4, V(N,O)-6, V(N,O)-5, and V(N,O)-7, moving clockwise from the top left. Depositions were conducted with 50 % nitrogen working gas, bias voltage 0 or ca. 100 V. Deposition times were 30, 61, 34, and 30 minutes, moving clockwise from the top left. Please see Table 2.4.1 for sample information.

impact on the morphology of DC-sputtered films; small, pyramid-shaped grains are observed. RF-sputtered films show a possible increase in surface feature size with the application of substrate bias. Density estimates by XRR indicate that films deposited under bias by RF and DC

sputtering have roughly the expected bulk density of pure VN (6.5 and 6.3 g/cm^3 measured vs 6.1 g/cm^3 bulk[1]). Films deposited by RF-sputtering under no substrate bias were less dense than bulk VN, as well as the calculated bulk density of a film with the same elemental composition and comprising ca. 80 mol % VN and 20 mol % V_2O_5 [iv][8] (ca. 4.9 g/cm^3 measured vs. ca. 5.7 g/cm^3 calculated). An increase in density with the application of substrate bias is plausible; adding energy to impinging metal atoms could help shift and rearrange surface atoms to the stable crystalline form. The use of bias does not appear to affect film growth rate: both the displayed RF-sputtered films had growth rates of 2 nm/min. A small decrease in growth rate has been observed with increasing bias, but the change was 6 % (6.7 to 5.6 nm/min) from 0 to 100 V—a difference that is unlikely to be distinguishable using XRR thicknesses.[8]

The application of substrate bias tends to reduce the oxygen content of the resulting film, and has no obvious effect on the nitrogen to vanadium ratio, which remains at ca. 1, in agreement with literature.[8]

Figure 2.4.2 shows these trends. RF-sputtered films also appear to have lower oxygen contents than DC-sputtered films. For small to moderate variations in base pressure, there is no obvious impact on oxygen content. Insufficient samples were deposited and measured to permit a systematic study, but two films deposited with 50 % nitrogen concentration in the working gas, ca. 100 V substrate bias, and base pressures of 8.9×10^{-9} or 1.5×10^{-8} Torr both had O:V ratios of 0.5. The impact of substrate bias or nitrogen partial pressure on O:V ratio was not reported in the literature consulted.

Changing the nitrogen concentration of the working gas from 0 to 17 % increases the

---

[iv] The least dense vanadium oxide, V_2O_5 (3.36 g/cm^3), was chosen to put a lower bound on the bulk density of a mixed-phase VN-V_2O_5 material.

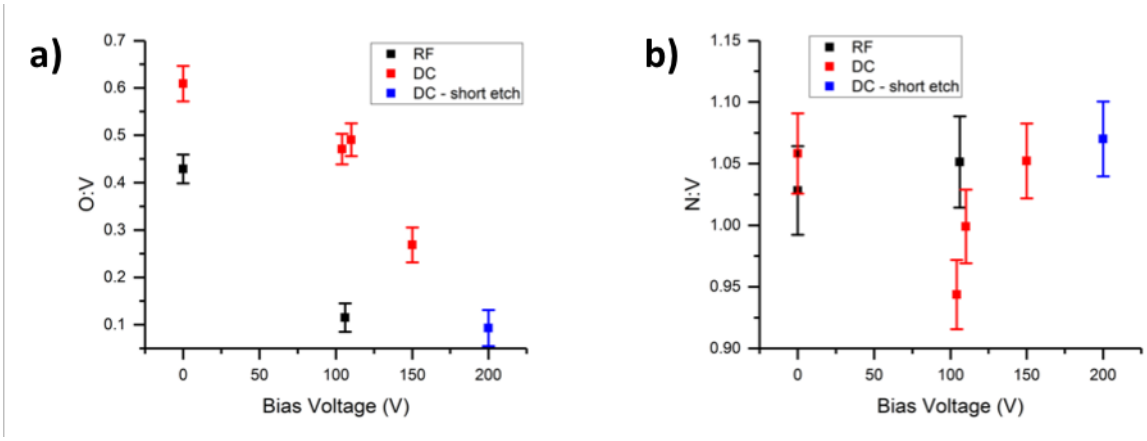

Figure 2.4.2: Ratios of (a) oxygen and (b) nitrogen to vanadium (by XPS) versus applied substrate bias. Working gas nitrogen concentration was 50 %, and deposition length was 30 minutes for all samples except for RF/106 V, which was 60 minutes. All films were etched for 60 seconds at 1 keV in monatomic sputtering mode, except the "short etch" sample, which was etched for 40 seconds.

N:V ratio from essentially zero[v][16] to ca. 1, but increasing the concentration to 50 % appears to have no additional impact on N:V ratio. This is in agreement with reported N:V for a similar deposition process.[8] A note regarding V(N,O) purity: Dr. Daniel Oates at MIT's Lincoln labs measured the resistivity vs. temperature of V(N,O)-6 (3 at. % oxygen), observing a superconducting transition temperature of 4.4 K. This is consistent with values for ultra-pure VN reported in the literature,[17] and suggests that this sample was sufficiently pure to maintain a connected, conductive network of pure VN grains.

PVD of V(N,O) and T(N,O) was performed on silicon thermal oxide wafers and stainless steel substrates. Nearly pure VN (2-3 at. % oxygen) was deposited under certain conditions, but pure TiN was never achieved, likely due to residual oxygen contamination in the deposition chamber.

---

[v] Intermittently, a few percent of nitrogen is observed on the surface of films deposited under argon. This might be due to residual nitrogen in the chamber or the surface of the target. Please see cited reference.

2.4.2 Composition of considered films

The composition of all the considered Ti(N,O), W(N,O,C), and V(N,C) films and a subset of the considered V(N,O) films was analyzed by XPS. Table 2.4.1 lists the film name, deposition method, XPS composition, whether ASR was measured on an equivalent film, and deposition details (in the case of PVD V(N,O) films). An "equivalent film" for an ASR sample is defined as a stainless steel substrate coated in the same deposition as the labeled film. The composition of V(N,C)-2 was estimated by analyzing a film deposited under the same conditions, but in a different run. Ti(N,O*) showed ca. 3 at. % Si at the surface, likely indicating exposed substrate. The composition of this film has been adjusted to exclude the Si signal, to make the values comparable to the other listed films.

Table 2.4.1: Compositions of a subset of the considered metal nitride films. The "ASR" column indicates whether ASR measurements were performed. ASR samples are stainless steel substrates prepared in the same deposition as the labeled film. The Deposition notes column lists the nitrogen percentage of the working gas (where relevant) and the applied substrate bias for V(N,O) and Ti(N,O) films. The composition of the Ti(N,O*) film has been adjusted to exclude the ca. 3 at. % Si signal, thought to be due to regions of exposed substrate. The composition of V(N,C)-2 was estimated by analyzing a film deposited under the same conditions, but in a different run.

Film	Deposition method	Metal (at. %)	N (at. %)	O (at. %)	C (at. %)	ASR	Deposition notes
V(N,O)-1	RF, PVD	39	39	22	0	no	17% N_2 0 V bias
V(N,O)-2	DC, PVD	47	51	2	0	no	17% N_2 160 V bias
V(N,O)-3	DC, PVD	47	49	4	0	no	17% N_2 200 V bias
V(N,O)-4	RF, PVD	42	43	15	0	no	50% N_2 0 V bias
V(N,O)-5	DC, PVD	38	40	23	0	no	50% N_2 0 V bias
V(N,O)-6	RF, PVD	47	50	3	0	yes	50% N_2 104V bias
V(N,O)-7	DC, PVD	39	48	13	0	no	50% N_2 100 V bias
V(N,O)-8	PVD	44	47	9	0	no	50% N_2 150 V bias
V(N,O)-9	PVD	44	50	6	0	no	50% N_2 200 V bias
V(N,C)-1	CVD	48	37	0	15	yes	
V(N,C)-2	CVD	46	35	0	20.	no	
Ti(N,O*)	PVD	35	17	48	0	yes	0 V bias
Ti(N*,O)	PVD	45	44	10	0	yes	93 V bias
Ti(N,O) comm.		47	45	8	0	yes	
W(N,O,C)	ALD	41	19	14	26	yes	

2.4.3 Material screening by dry cell ASR

To evaluate the ASR contribution of the metal nitrides films described in the preceding section, films were deposited on stainless steel substrates and measured in the previously described dry cell resistance set up. All ASR samples are deposited in the same run as one of the films listed in Table 2.4.1, and labeled in figures and in the text with the name of that sample. Figure 2.4.3 shows the most promising results from each type of material measurements. In the case of Ti(N,O), the samples represent sputtered films with two different oxygen contents (Ti(N*,O) and Ti(N,O*)), and a commercial Ti(N,O) film (2-3 μm CVD coating, nominally TiN, on a stainless steel 316 substrate, Goodfellow). Dry cell ASR measurements of SnO_2(F) and graphite were used as the maximum and current best-case ASR benchmarks. To merit further study, a coating needed to produce a lower or equivalent dry cell ASR to SnO_2(F). The deposition conditions for each coating are listed below.

In the figure, "Ti(N,O*)" is a high oxygen content film deposited by RF sputtering at 150 W under no bias in a different sputtering system (base pressure of 3.4×10^{-6} Torr). "Ti(N*,O)" is a typical Ti(N,O) film deposited by RF sputtering method described in section 2.3.1.2 The "Ti(N,O) – comm" film is the previously mentioned commercially-sourced TiN-coated substrate. V(N,C)-2 was deposited at 330 °C with 100 sccm nitrogen and 20 sccm ammonia for 120 minutes at a nominal temperature of 325 °C (actual temperature 276-323 °C). V(N,O)-6 was deposited by RF magnetron sputtering over 34 minutes with 50 % nitrogen working gas and a substrate bias of 104 V. Using the system detailed in Chapter 1, the SnO_2(F) sample was deposited over 30 minutes at a temperature of ca. 450 °C, with reagent delivery rates of 5.7 μmol/min tetramethyltin, 126 μmol/min bromotrifluoromethane, 780 μmol/min oxygen, and a balance of nitrogen to reach a total flow rate of 94 sccm. This sample is the best-performing

SnO_2(F) coating in terms of dry cell ASR. W(N,O,C), CVD V(N,C), and commercial Ti(N,O) are deposited on 1″ × 1″ substrates (the former two substrates are 0.25″ thick, while the latter is ca 0.038″ thick). PVD V(N,O) and Ti(N,O) are deposited on 3″ × 3″ × 0.038″ stainless steel substrates.

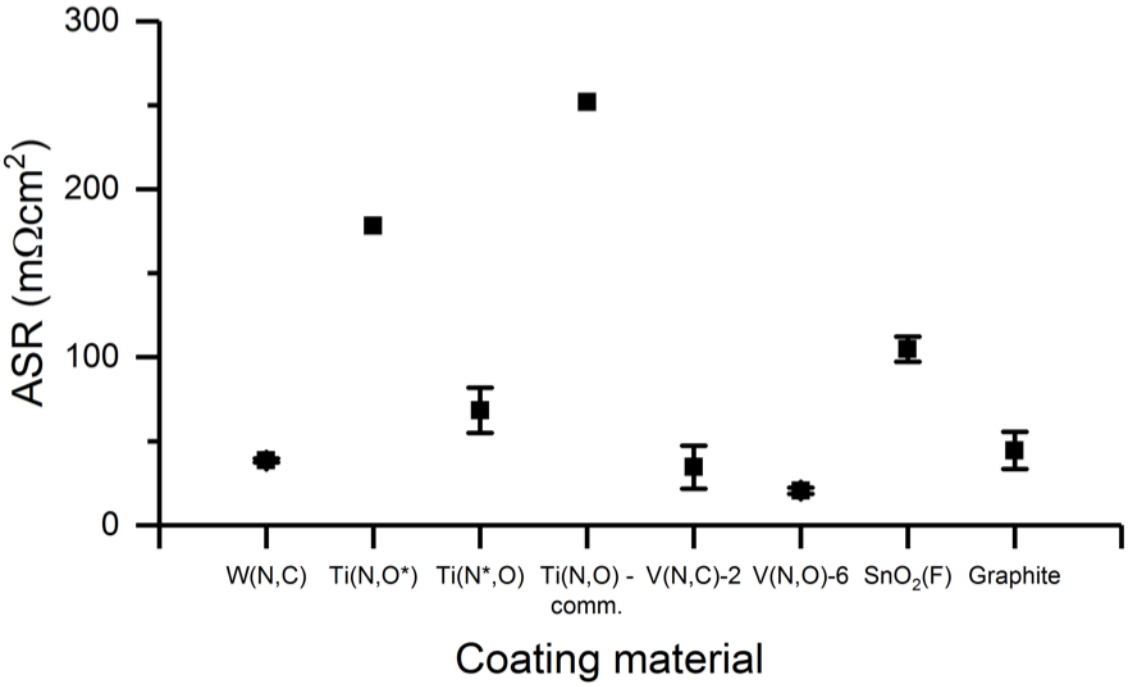

Figure 2.4.3: Dry cell ASR measured for the metal nitrides studied in this work. The carbon paper electrode is one sheet of Sigracet SGL 39aa, baked for 24 hours in air at 400 °C. W(N,O,C), CVD V(N,C), and commercial Ti(N,O) were deposited on 1″ × 1″ substrates (the former two are 0.25″ thick, while the latter is ca 0.038″ thick). PVD V(N,O) and both Ti(N,O) were deposited on 3″ × 3″ × 0.038″ stainless steel substrates. W(N,O,C) was deposited by ALD as described in section 2.3.1.4. "Ti(N*,O)" and "Ti(N,O*)" are a typical substrate-biased, RF-sputtered film and a film with high oxygen content deposited in another sputtering system. The "Ti(N,O) – comm" film is a 1″ commercially sourced TiN-coated substrate. The CVD V(N,C), PVD V(N,O), and Ti(N,O) films were deposited on stainless steel in the same run as the plot label indicates (i.e., the PVD V(N,O) film was deposited in the same run as V(N,O)-6). The SnO_2(F) sample is the coated plate from Chapter 1 with the lowest dry cell ASR. The graphite plate dry cell was also reported in Chapter 1. As-received graphite flow plates were used. Data points for Ti(N,O*) and commercial Ti(N,O) are single measurements. All other data points are the average of three consecutive measurements and error bars are 95 % confidence intervals. For the expected composition of these films, please see the corresponding sample Table 2.4.1.

Due to the sample size limits of the CVD V(N,C) and ALD W(N,O,C) systems, 1″

samples were used, rather than 3″ plates. For similar reasons, PVD Ti(N,O) samples were deposited on 0.038″ thick 316 stainless steel, rather than the 0.25″ plates used for other materials. The bulk resistance of stainless steel is assumed to be negligible, so all 3″ substrates are assumed to be comparable for the purposes of ASR testing. Assuming the coating-graphite interface is the dominant source of resistance, measurements of 1″ and 3″ inch substrates should also be comparable provided that ASR, rather than dry cell resistance, is used. This metric accounts for the different carbon electrode area used for testing the coated stainless steel plates. If the other cell interfacial resistances increase due to the smaller contact area of a 1″ substrate, then the measurement is an upper bound for the dry cell ASR of coatings on 3″ substrates.

Based on the dry cell ASR metric, all coatings except the high oxygen-content Ti(N,O) and the commercial Ti(N,O) are worthy of consideration. All of the metal nitrides compare favorably to SnO_2(F), and the vanadium- and tungsten-based films appear poised to out-perform graphite. Unsurprisingly, the higher oxygen content titanium nitride films have a higher ASR—titanium oxide is a more resistive material than titanium nitride, and the incorporation of oxygen into titanium nitride would be expected to reduce the carrier concentration (making the film less metallic) and hence increase the contact resistance. V(N,C) has a higher ASR than V(N,O). This could be due to the smaller substrate, as mentioned above, but also the more metallic character of VN than VC[2] (vanadium oxide is less metallic than either VN or VC, but the V(N,O) film has less than 3 at. % oxygen, and hence should be dominated by VN-type metallic behavior).

2.4.4 Evaluation of metal nitride stability to bromine and hydrobromic acid exposure

As previously described, metal nitride films deposited on glass or silicon thermal oxide were exposed to either pure bromine (Aldrich, reagent grade) or concentrated hydrobromic acid (Fluka, purum, >48 %) for 14 or 19 days as an initial chemical stability screening. In the 14-day

test, the sheet resistance of two pieces of each film was measured, then one of each was immersed in bromine or hydrobromic acid, and the sheet resistance was measured after 14 days of exposure (see Figure 2.5.4 and Figure 2.4.5). Samples V(N,C)-1, V(N,C)-2, and Ti(N,O*)

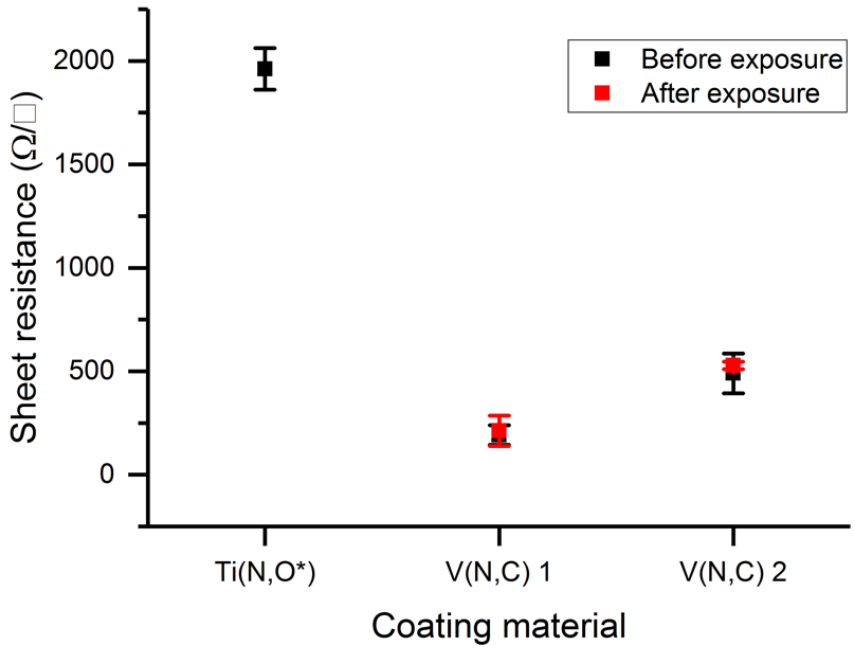

Figure 2.4.4: Sheet resistance of Ti(N*,O) and two CVD V(N,C) samples after 14-day exposure to bromine. Data points are the average of three consecutive measurements and error bars are 95 % confidence intervals. Please see Table 2.4.1 for sample information.

were tested, and only V(N,C)-1 showed no change in sheet resistance after exposure to either bromine or hydrobromic acid. The acid-exposed V(N,C)-2 piece showed a slight increase—the 95 % confidence intervals of the sheet resistance values are not overlapping. The acid-exposed Ti(N,O*) showed more than a factor of 2 increase in sheet resistance. Upon exposure to bromine, Ti(N,O*) appeared to dissolve completely: the film color returned to that of the silicon oxide substrate, and the sheet resistance was out-of-range of the 4-point probe (i.e., $> 5 \times 10^5$ Ω/□). A sample of lower oxygen content, Ti(N*,O), was subjected to similar exposure, and was no more robust to attack by hydrobromic acid or bromine. V(N,C)-2 showed no change in sheet resistance

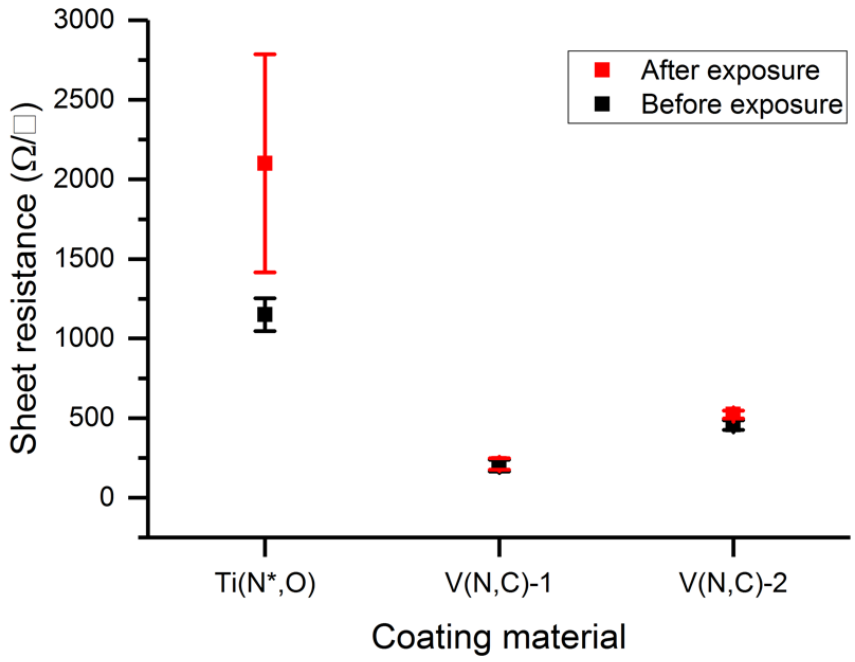

Figure 2.4.5: Sheet resistance of Ti(N*,O) and two CVD V(N,C) samples after 14-day exposure to concentrated hydrobromic acid (48 %). Data points are the average of three consecutive measurements and error bars are 95 % confidence intervals. Please see Table 2.4.1 for sample information.

within error. Based on these results, CVD V(N,C) was designated as sufficiently chemically resistant for the next stage of stability testing.

Films of W(N,O,C) and a series of PVD V(N,O) films were subjected to bromine and hydrobromic acid exposure for 19 days. Sheet resistances were measured for all samples before testing. Upon the completion of the test, samples were removed, and the film color was compared to an existing, pristine sample from the same deposition. The sheet resistance of a selection of films was measured after exposure, and others after aging in air for 2 months. As detailed in Figure 2.4.6 most of the films tested showed no color change in response to hydrobromic acid exposure. Only V(N,O) samples deposited by DC sputtering at 50 % nitrogen (working gas) and 0 or ca. 100 V bias (V(N,O)-5 and V(N,O)-7, respectively), and a film deposited at 8 % nitrogen (working gas) and 0 V bias showed visible signs of degradation.

W(N,O,C) films showed color change, but were not dissolved.

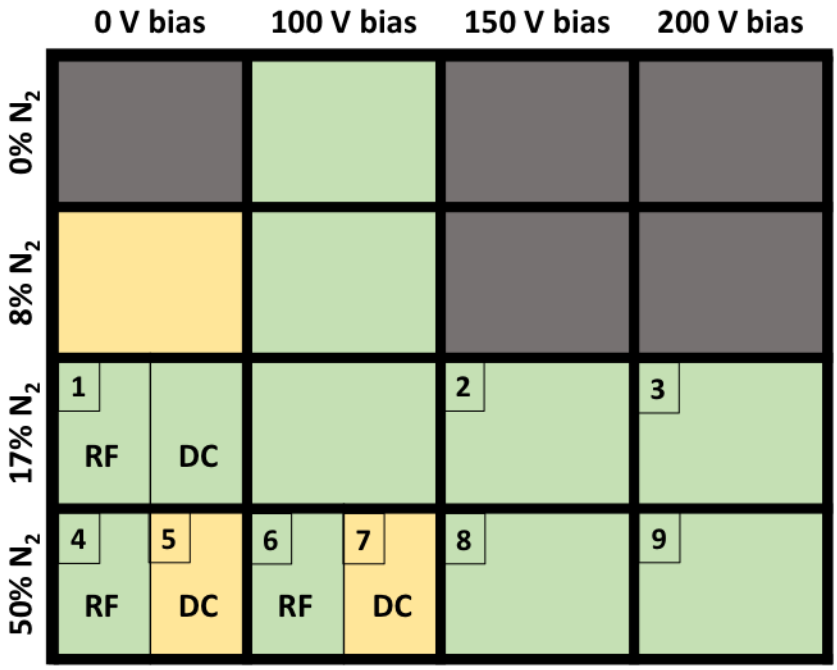

Figure 2.4.6: Stability of V(N,O) films subjected to room temperature hydrobromic acid exposure for 19 days. Column labels indicate the size of the applied substrate bias and row labels indicate the nitrogen concentration of the working gas. An "RF" or "DC" label indicates whether RF or DC sputtering was used (unlabeled boxes were DC-sputtered). The box colors indicate the appearance of samples after exposure to concentrated hydrobromic acid. Green indicates no visible color change, yellow indicates visible color change, and dark grey indicates that no representative sample was deposited for that set of conditions. The numbers in the upper left corner of each box are sample numbers from Table 2.4.1.

Resistance to hydrobromic acid attack appears to be inversely correlated to a film's oxygen content. Figure 2.4.7 duplicates Figure 2.4.6, and includes the measured oxygen composition (by XPS). Most of the surviving films have a low (below 10 at. %) oxygen content, and all the measured films showing color change had 15 at. % oxygen or greater. All oxides of vanadium are readily dissolved in acid,[18] presumably explaining the correlation between

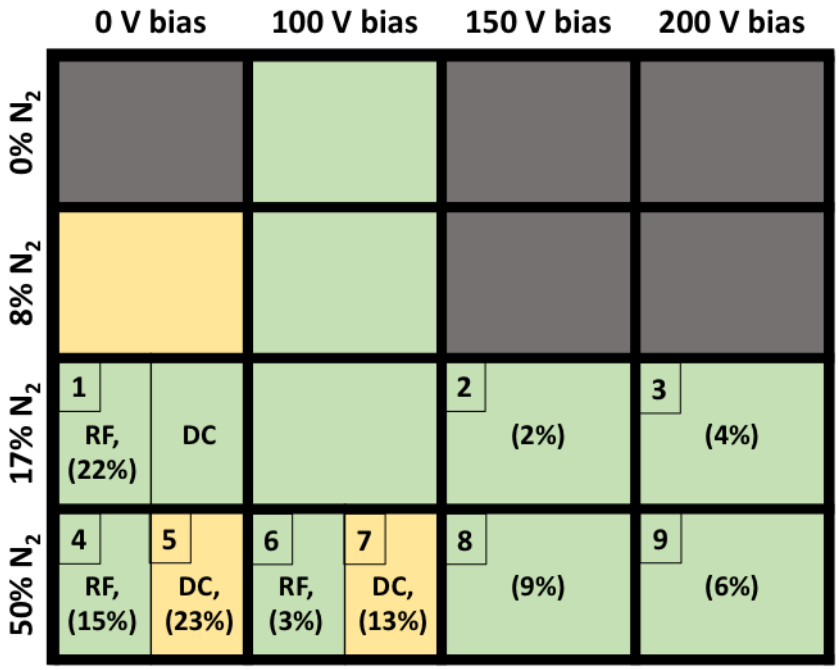

Figure 2.4.7: Stability of metal nitride films subjected to room temperature hydrobromic acid exposure for 19 days (including film oxygen content). Column labels indicate the size of the applied substrate bias and row labels indicate the nitrogen concentration of the working gas. For samples where composition was measured, oxygen content is listed in parentheses. An "RF" or "DC" label indicates whether RF or DC sputtering was used (unlabeled boxes were DC-sputtered). The box colors indicate the appearance of samples after exposure to concentrated hydrobromic acid. Green indicates no visible color change, yellow indicates visible color change, and dark grey indicates that no representative sample was deposited for that set of conditions. The numbers in the upper left corner of each box are sample numbers from Table 2.4.1

resistance to hydrobromic acid attack and low oxygen content. Ti(N,O) and W(N,O,C) results are consistent with this trend. Both Ti(N,O) films were fully dissolved by hydrobromic acid, while W(N,O,C) showed an increase in sheet resistance.

To further distinguish sample stability, sheet resistance was measured for films marked in green deposited with 50 % nitrogen working gas, and the film deposited with RF sputtering at 0 V bias and 17 % nitrogen working gas. By this point, the pieces had aged for 2 months in air, but the samples with oxygen content 6 % or less showed no change in sheet resistance. The sample with 9 % oxygen showed a slight increase in sheet resistance, and all other samples showed more significant increases. These values displayed in Figure 2.4.8 correspond to the sample number

listed in Table 2.4.1 and the upper right hand corner of each box in Figure 2.4.7.

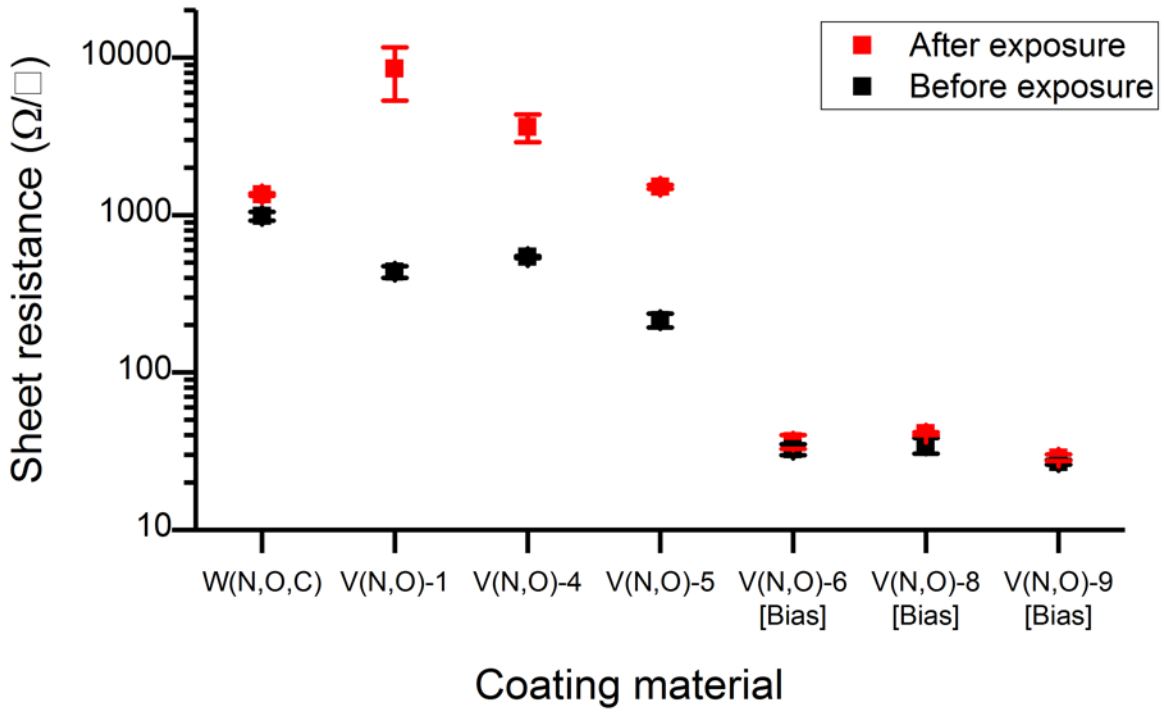

Figure 2.4.8: Sheet resistances for films before and after a 19-day hydrobromic acid exposure. W(N,O,C) was measured immediately after exposure, and other samples were measured after 2 months of aging in air. Samples deposited under bias are marked as such. Data points are the average of three consecutive measurements and error bars are 95 % confidence intervals. Please see Table 2.4.1 for sample information.

Also included are the results for W(N,O,C), which were measured immediately after removal from solution. These sheet resistance measurements are consistent with the trend of more corrosion-resistant samples containing less oxygen.

No PVD vanadium- or ALD tungsten-based samples, except a vanadium-based film deposited under ca. 100 V bias and pure argon, retained the same appearance after a 19-day exposure to bromine. This last set of conditions does not produce a repeatable film: residual nitrogen and oxygen on the surface of the target and in the chamber lead to a film with no

guaranteed compositional uniformity with depth or on the surface. While the apparent survival of this film poses an interesting scientific puzzle, it is ultimately not practical to pursue. Notably, the W(N,O,C) film saw a smaller sheet resistance change after bromine exposure (21 %) than acid exposure (37 %). This is believed to be related to the carbon content of the film, and will be addressed shortly. Figure 2.4.9 shows variation in film appearance after bromine exposure, organized by deposition conditions. There is no obvious connection between the deposition conditions used for PVD V(N,O) and resistance to bromine.

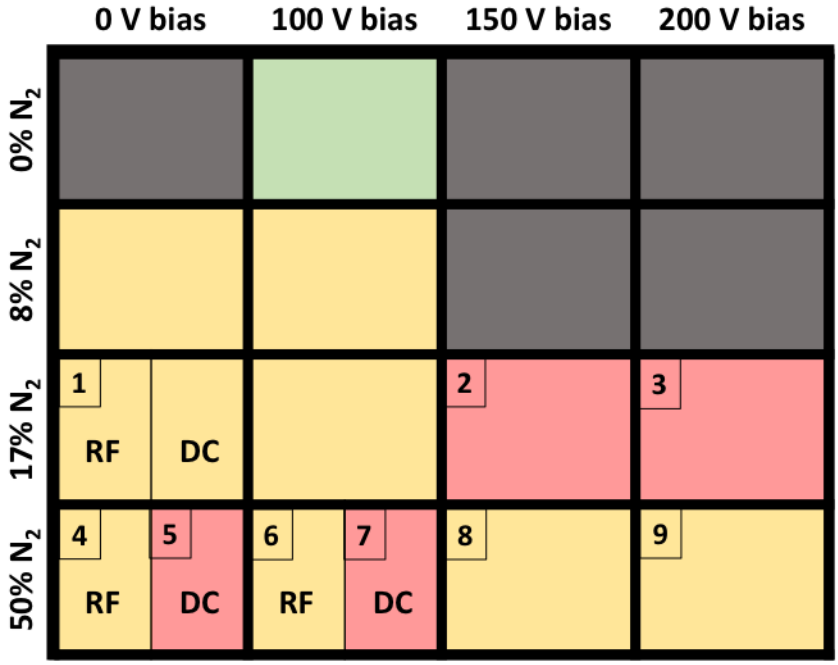

Figure 2.4.9: Stability of metal nitride films subjected to room temperature bromine exposure for 19 days. Column labels indicate the size of the applied substrate bias and row labels indicate the nitrogen concentration of the working gas. An "RF" or "DC" label indicates whether RF or DC sputtering was used (unlabeled boxes were DC-sputtered). The box colors indicate the appearance of samples after exposure to pure bromine. Green indicates no visible color change, yellow indicates visible color change, red indicates a return to the substrate color (suggesting film dissolution), and dark grey indicates that no representative sample was deposited for that set of conditions. The numbers in the upper left corner of each box are sample numbers from Table 2.4.1.

The bromine corrosion resistance of V(N,C)-1 and -2, and to some extent W(N,O,C), cannot be explained by oxygen content alone. While these films contained minimal oxygen, the

PVD film of quite pure VN (containing less than 3 at. % oxygen by XPS) showed evidence of attack by both bromine and hydrobromic acid. The presence of carbon appears correlated to stability in bromine. XPS compositions of films subject to stability testing are displayed in Figure 2.4.10. Further detail about these samples is listed in Table 2.4.1. All film compositions are measured on pieces from the same deposition,[vi] with the exception of V(N,C)-2: an extra piece was not available, so the composition was measured on a piece deposited under similar conditions.

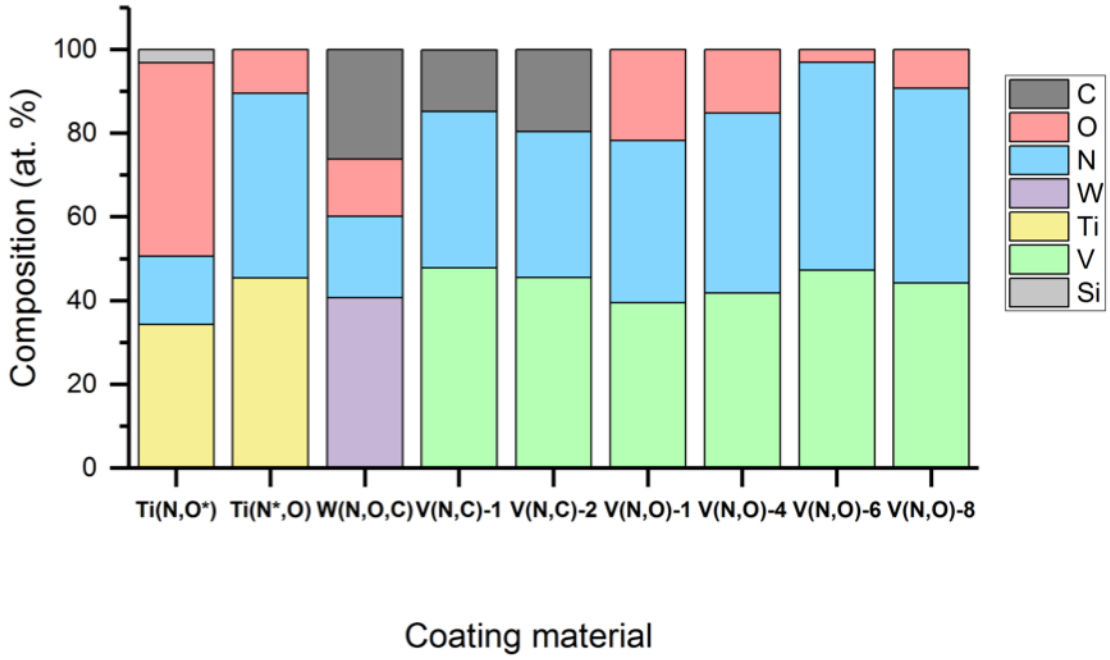

Figure 2.4.10: Compositions by XPS of a representative subset of the metal nitride films subjected to room temperature bromine and hydrobromic acid stability tests. Please see Table 2.4.1 for further sample information.

The data in Figure 2.4.10 reflect the oxygen variation previously noted, and the carbon

[vi] A different piece must be used for composition, because the surface of film must be sputtered away to determine the bulk composition. The damage resulting from sputtering might impact the stability of the film during exposure.

variation in question. The most stable vanadium-based film has the least carbon, and the tungsten films has the most. VN, VC, and TiN are attacked by room temperature solutions of 10:1 acetonitrile to bromine.[18] Carbides and nitrides of vanadium and titanium are also thermodynamically unstable in bromine and hydrobromic acid—the reactions to form tetravalent metal bromides are exothermic,[19] as demonstrated in Table 2.4.2. This fact suggests that variations in corrosion rate between the different nitrides and carbo-nitrides must be driven by kinetics.

Reaction	Enthalpy of Reaction (kJ/mol)
$VN + 2Br_2 \longrightarrow VBr_4 + \frac{1}{2}N_2$	-120
$VN + 4HBr \longrightarrow VBr_4 + \frac{1}{2}H_2 + NH_3$	-20
$VC + 4Br_2 \longrightarrow VBr_4 + CBr_4$	-207
$TiN + 2Br_2 \longrightarrow TiBr_4 + \frac{1}{2}N_2$	-279
$TiN + 4HBr \longrightarrow TiBr_4 + \frac{1}{2}H_2 + NH_3$	-180
$TiC + 4Br_2 \longrightarrow TiBr_4 + CBr_4$	-403
$C + 2Br_2 \longrightarrow CBr_4$	+29
$C + 4HBr \longrightarrow 2H_2 + CBr_4$	+66

Table 2.4.2: Standard enthalpies of reaction for byproducts of VN, VC, TiN, and TiC attack by bromine and hydrobromic acid.[19]

Film morphology and density differences are potential kinetic factors, but neither hypothesis is supported by the data. As shown in Figure 2.4.11, while morphology varies somewhat between the vanadium-based films, no trend related to corrosion resistance is apparent. Similarly, there is insufficient evidence to attribute stability differences to density

variation. While XRR data suggests density differences between different V(N,O) films, this effect is confounded by the variations expected as a result of the variations in oxygen content. No density measurements were made on the V(N,C) films, as they were too thick for XRR.

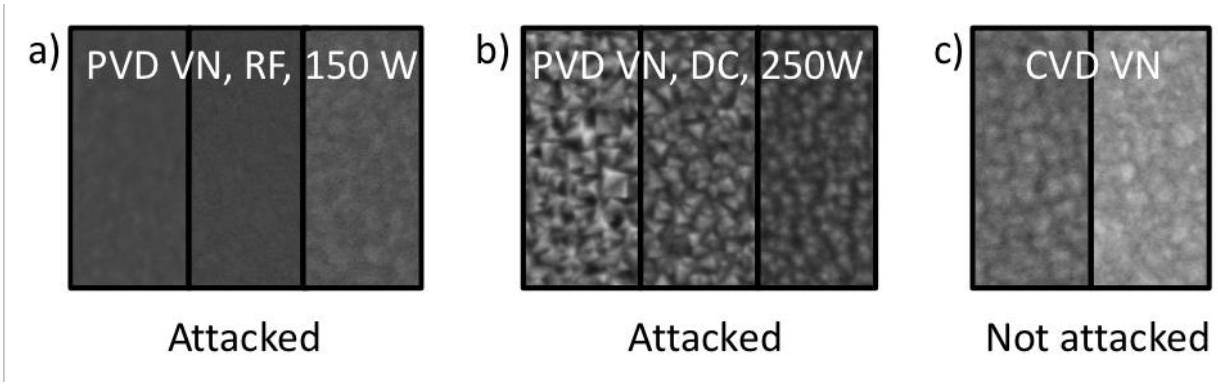

Figure 2.4.11: Morphology of PVD V(N,O) and CVD V(N,C) films. Films were deposited using a) RF sputtering, b) DC sputtering, and c) CVD. There are morphological similarities between films that were attacked (e.g., the left-most RF sample) and those that were not (e.g., CVD VN).

Returning to the correlation of carbon content with corrosion resistance, high-resolution XPS carbon 1s scans of the considered nitride films show evidence of primarily two types of carbon bonds: metal carbide (~283 eV binding energy) and carbon-carbon (~284-284.8 eV binding energy). Deconvoluting these peaks in the XPS software can give an estimate of the relative abundance of each bond type. Figure 2.4.12 displays a captured image of the software's deconvolution of a sample carbon 1s scan. Deconvolution suggests that ca. 19 at. % carbon in V(N,C)-2 is roughly evenly divided between metal carbide and carbon-carbon bonds. While the bonding identity of carbon atoms (17 at. %) for V(N,C)-1 were not quantitatively assessed, no carbide peak is present in a high resolution carbon 1s scan. Therefore, it appears that greater resistance to bromine is correlated with higher concentrations of elemental carbon, not carbide. This is consistent with the literature describing bromine attack on metal nitrides and carbides in acetonitrile:[18] VC is much more aggressively attacked than VN, implying that it is unlikely to protect a carbonitride film. While the oxygen content of W(N,O,C) might influence its

vulnerability to hydrobromic acid, its greater resistance to bromine might similarly be explained by the presence of elemental carbon. Of the ca. 26 at. % carbon in W(N,O,C), ca. 30 % is carbide, and the rest elemental carbon.

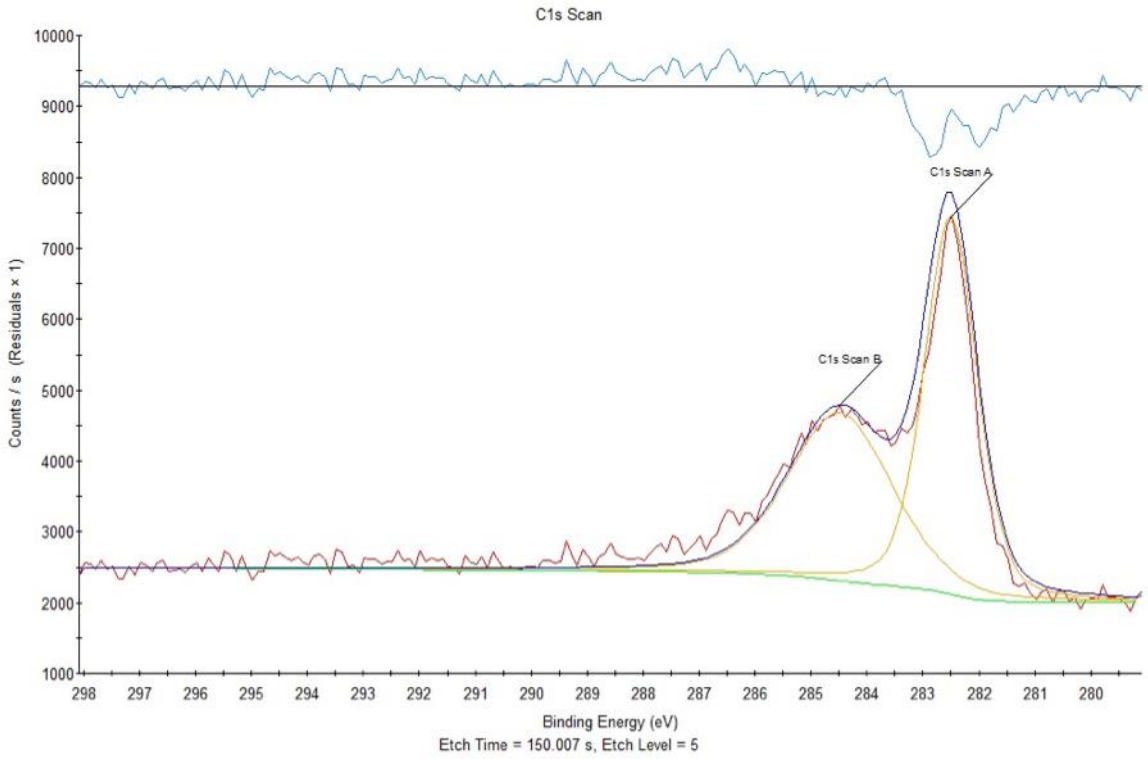

Figure 2.4.12: A screenshot of the XPS software, during carbon peak deconvolution. The raw data is displayed in red, the background in green, and in yellow, the fitted peaks for elemental carbon (left) and carbide (right).

For the films considered, oxygen content appears to be inversely correlated with stability to hydrobromic acid. Only carbon-containing vanadium nitride films were resistant to bromine attack, and this advantage correlates with the presence of elemental carbon. The reaction of carbon and bromine or HBr to form carbon tetrabromide (or carbon tetrabromide and hydrogen) has a positive enthalpy of reaction. Although bromine is known to exfoliate graphite sheets from the bulk material, the carbon-carbon bonds are not necessarily attacked. We speculate that the presence of a stable carbon phase within a VN film may actually slow degradation.

While stable to pure bromine or concentrated hydrobromic acid exposure, V(N,C) films did not withstand heating in electrolyte. As with SnO_2(F), a V(N,C) film deposited on silicon[vii] was immersed in a 58 °C solution of 3 M hydrobromic acid and 1.5 M bromine. Periodically over 14 weeks, the sample was removed, and the color and appearance examined by eye. The sample maintained a consistent sheet resistance throughout the 14-week trial: ca. 200 ± 30 Ω/□ pristine, 190 ± 30 Ω/□ after 1.4 weeks, and 190 ± 80 Ω/□ after 14 weeks of exposure.[viii] Though no color change was noted, the color of the as-deposited film was essentially identical to that of the bare substrate. An XPS scan after 14 weeks of exposure and subsequent aging in air showed no evidence of vanadium on the surface. It appears that the film dissolved at some point during the 14-week exposure, but the original V(N,C) film's sheet resistance was, unfortunately and coincidentally, remarkably similar to that of the substrate after exposure to heated electrolyte. The destruction of the film supports the hypothesis that the presence of carbon slows, but does not halt, film degradation in electrolyte. Ultimately, none of the nitride films studied showed sufficient resistance to bromine attack to merit further consideration. Fortunately, two bromine-stable materials have been demonstrated in this work: SnO_2(F), as described in Chapter 1, and a commercially-available sealed graphite plate from Entegris, described in the next section.

2.4.5 Stability of Entegris sealed flow plates

The corrosion-resistance of sealed graphite flow plates was assessed by monitoring the ASR of two Entegris pyrolytically-sealed graphite plates exposed to heated electrolyte for 12 weeks. As Figure 2.4.13 shows, the dry cell resistance/ASR is stable throughout the study. The

[vii] Deposition conditions similar to that of V(N,C)-2.

[viii] Values are the average of 3 measurements, errors are 95 % confidence intervals.

fluctuation in resistance is likely due to the variability of the dry cell resistance measurement. Optical micrographs show no evidence of exfoliation on the surface of the plates (see Figure 2.4.14 below).

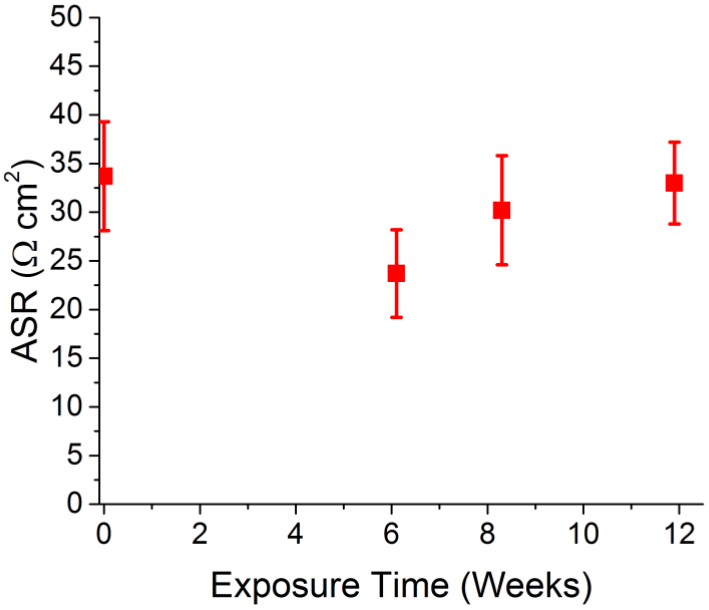

Figure 2.4.13: ASR measurements for Entegris flow plates after heating to 58 °C in a 3 M hydrobromic acid / 1.5 M Br_2 solution. Data points are the average of 3 measurements each of 2 samples, and error bars are 95 % confidence intervals.

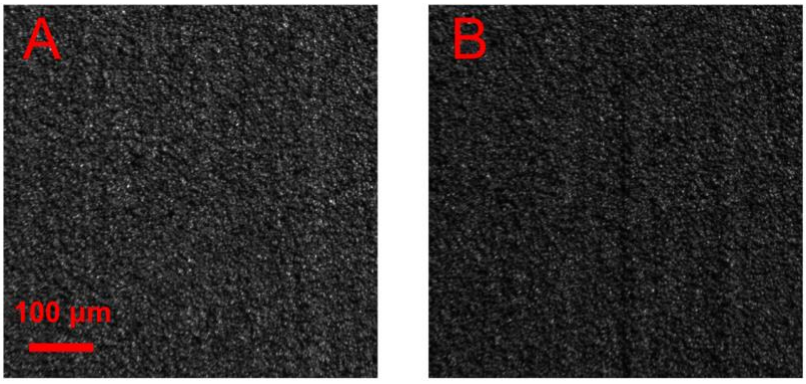

Figure 2.4.14: Optical micrographs of Entegris flow plates before and after heating to 58 °C in a 3 M hydrobromic acid / 1.5 M Br_2 solution.

Based on the presented data, the in-house sealing process employed by Entegris

adequately protects graphite plates from the destructive effects of bromine exposure. This may be due a reduction in the total exposed surface area (due to the closing of pores) and a chemical or structural change in the surface which makes the material less vulnerable to bromine intercalation. Anecdotal observations during testing suggest that the sealing process might not eliminate bromine incorporation; even after extended soaking in de-ionized water, the plates continue to smell of bromine. This suggests that either bromine reversibly intercalates into these plates, or the surface is sufficiently porous to trap bromine for some length of time.

Though SnO_2(F)-coatings show promise in terms of ASR and corrosion resistance, we have elected to use Entegris flow plates. The latter can be custom-machined and sealed by the vendor, whereas SnO_2(F) deposition has not been sufficiently optimized to produce pinhole-free coatings on stainless steel flow plates. Furthermore, the use of graphite plates is expected to lessen the importance of carbon paper choice. As noted in Chapter 1, dry cells assembled with 39aa vs. 10aa differ in ASR by merely 30 $m\Omega \cdot cm^2$—a small number compared to other sources of resistance in the cell. This number may differ for sealed plates, but is expected to be small compared to the 2- to 8-fold difference seen for SnO_2(F)-coated plates. To wit, the dry cell ASR for a cell using sealed flow plate and 39aa (the worse-performing paper for SnO_2(F)) is ca. 30 $m\Omega \cdot cm^2$—a factor of ca. 3 smaller than the best performing SnO_2(F) coating and negligible compared to the largest resistance sources in the cell.

2.4.6 Carbon paper electrode stability

Unlike unsealed graphite flow plates, which have been observed to crack after exposure to bromine-based electrolyte in a flow battery assembly, observations of damage to carbon paper have been limited and inconclusive. Occasionally, fragments of carbon paper collect in parts of

the flow battery during operation (e.g., in the flow channels). The occurrence is sufficiently infrequent that it has not been possible to definitively blame bromine exposure, as opposed to mechanical damage sustained during cell assembly. Accordingly, the carbon paper used in flow battery cells was subjected to chemical stability testing, similarly to the flow plates.

Sigracet SGL 39aa carbon paper was exposed to heated electrolyte for 25 days. The DCR and ASR values of pristine and electrolyte-exposed carbon paper are 9 ± 2 mΩ (45 ± 11 mΩ·cm^2) and 6.2 ± 1.5 mΩ (31 ± 8 mΩ·cm^2), respectively.[ix] The stability in morphology (see Figure 2.4.15) and dry cell resistance is consistent with negligible degradation of the electrode by electrolyte exposure. SGL 39aa appears stable to bromine, and yields acceptable ASR values when paired with graphite flow plates.

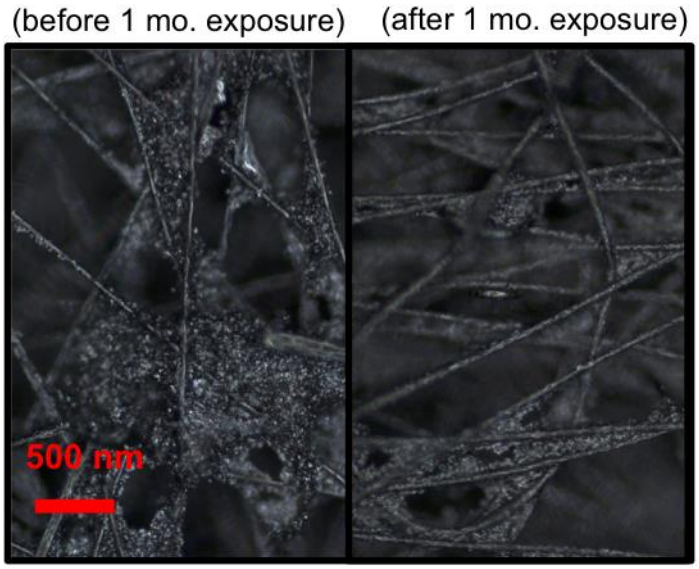

Figure 2.4.15: Sigracet SGL 39aa carbon paper (L) with no exposure to heated electrolyte, and (R) after 25 days of exposure.

[ix] Data points for the initial and final DCR/ASR are are the average of 4 and 3 measurements, respectively. Error bars are 95 % confidence intervals.

2.4.7 Membrane stability

Figure 2.4.16 shows the membrane in-plane conductivity over the course of stability testing. The conductivity shows some variation, and possibly a slight decrease over 10 weeks.

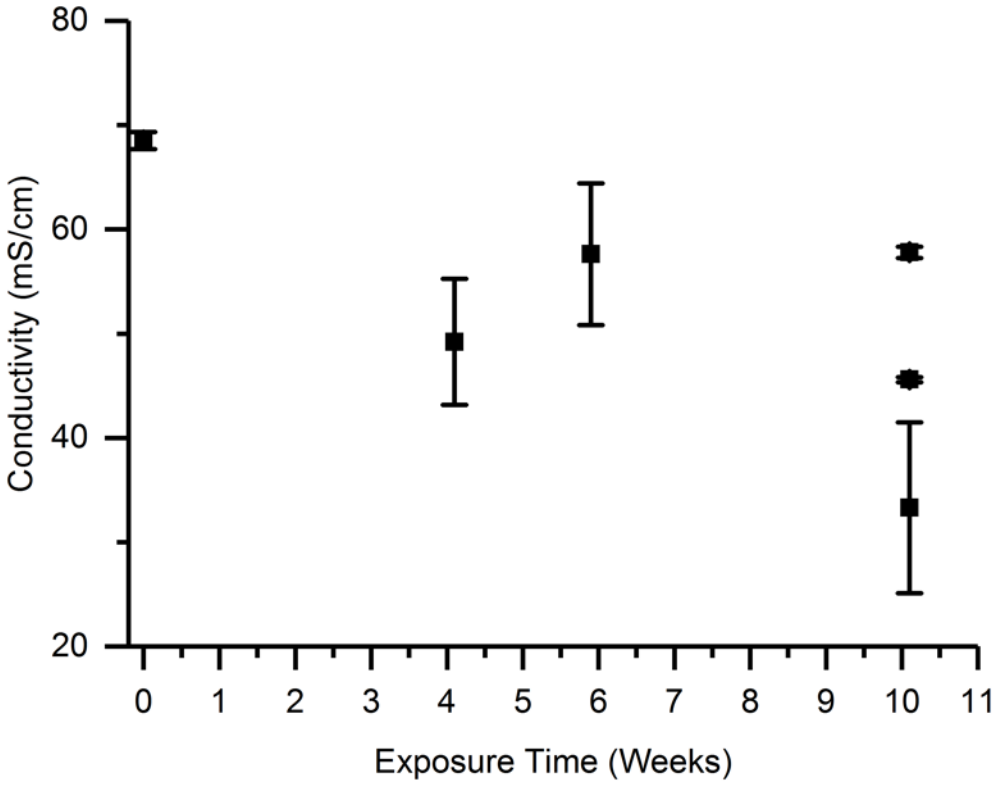

Figure 2.4.16: Membrane conductivity after heating to 58 °C in a 3 M hydrobromic acid / 1.5 M Br_2 solution. Values are the average of three measurements. Error bars are 95 % confidence intervals.

There appears to be substantial membrane-to-membrane variability, exemplified by the spread in data points at the final time point; the difference between these points is much larger than the measurement error of each point. The difference between the final data points may be due to differing degrees of degradation, or to variability inherent in the measurement itself. For example, degradation would likely be due to bromination of the membrane (i.e., the sulfonic acid groups are replaced by Br^-), and would decrease membrane conductivity. An increase in

conductivity may be due to residual hydrobromic acid in the membrane. Similarly, the unexpected shifts in previous data points (e.g., the apparent increase in conductivity between the second and third time point) could be interpreted as measurement noise from varying acid residue. With this in mind, the data in Figure 2.4.16 is more appropriately interpreted as follows: membranes retain some conductivity after exposure to heated electrolyte, and a substantial number of replicates may be necessary to reduce measurement uncertainty. Since the membrane is the largest contributor to cell ohmic resistance (and the most expensive), further stability studies are recommended, including the addition of other measures of membrane performance (e.g., proton uptake through membrane titration).

2.5 Conclusions

The variability of solar and wind energy is a hindrance to widespread implementation of these technologies. Flow batteries based on bromine/hydrobromic acid electrolytes have the potential to remove this obstacle by storing excess energy and smoothing the resulting electricity output. The stability of all flow battery components is important to reducing operating costs in the long term. The corrosive environment created by bromine and hydrobromic acid electrolyte leads to the destruction of graphite components, specifically flow plates, increasing costs and limiting the practical lifetime of such devices. The impact of electrolyte exposure on the Nafion proton exchange membrane and carbon paper electrodes must also be assessed. Accordingly, metal nitride films were developed and evaluated as electrolyte-stable flow plate coatings. The stability of Nafion membranes and carbon paper electrodes was assessed.

Vanadium, titanium, and tungsten-based nitrides were evaluated for adequate area specific resistance and chemical stability. Stainless steel plates, glass, and silicon thermal oxide

wafers were coated by the following processes: physical vapor deposition of V(N,O) and Ti(N,O), chemical vapor deposition of V(N,C), and atomic layer deposition of W(N,O,C). An initial screening of dry cell resistance and area specific resistance was performed for commercially available Entegris sealed graphite flow plates and stainless steel plates coated with PVD V(N,O), CVD V(N,C), PVD Ti(N,O), commercial Ti(N,O), and ALD W(N,O,C). All films had adequate dry cell resistances (below that of SnO_2(F)) except commercial Ti(N,O). A second screening exposed test films deposited on SiO_2 and/or glass to pure bromine and concentrated hydrobromic acid at room temperature. Only CVD V(N,C) showed no change in appearance or sheet resistance after exposure to both bromine and hydrobromic acid. The relative resistance of V(N,C) to ca. 2-week bromine exposure is thought to be related to the elemental carbon content of the film. A second stability test included additional flow battery components. A CVD V(N,C) film, Entegris flow plates, carbon paper electrodes, and Nafion membranes were immersed in a 3 M bromine/1.5 M hydrobromic acid electrolyte solution at 58 °C for several weeks to 2 months. Flow plates and carbon paper showed stable ASR throughout the test. Conductivity measurements of Nafion membranes showed high variability, but significant degradation was not evident. Finally, the V(N,C) film dissolved completely during the test.

The considered metal nitride films have ASR acceptable or superior to SnO_2(F) and Entegris flow plates, but insufficient chemical resistance. Entegris pyrolitically sealed graphite plates are the most suitable for the immediate application of bromine/hydrobromic acid-based flow batteries: they are commercially available, can be machined with different flow field patterns before sealing, show favorable area specific resistance, and appear robust to bromine and hydrobromic acid attack. In other applications, the flexibility of APCVD SnO_2(F) coatings might be preferable, particularly in cases where pre-existing parts must be protected, sealed

graphite is insufficiently chemically resistant, or its brittleness presents an obstacle. Regarding the latter idea, researchers in our collaboration have encountered challenges in reducing the size of machined graphite features. For example, the width of flow channel walls is limited by the tendency of thin graphite walls to crack and break. Regardless, APCVD SnO_2(F) represents another coating option for researchers and manufacturers working with highly corrosive materials. Assessing stability and performance of these coatings in more realistic operating conditions is a logical next line of inquiry. Testing under short- and long-term electrochemical cycling could support or discourage the application of this coating in ways not revealed by this work.

Further experiments are required to draw definitive conclusions regarding the stability of Nafion membranes, though the results are consistent with some degradation with exposure to heated electrolyte. As the most expensive structural component in a flow battery, membranes have attracted much research interest, and doubtless, stability assessment should be part of that program. Here, an expanded repertoire of stability tests including membrane titration, through-plane conductivity testing, membrane crossover rates for the electrolytes of interest, and mechanical robustness, would be of interest.

The main obstacle addressed by this work—failure of graphite flow plates—has been solved via the availability of pyrolytic sealing of graphite. This process is highly scalable, commercially accessible, and inexpensive—in other words, well-suited to the needs of commercial flow battery installations.

References

1. Toth, L., *Transition metal carbides and nitrides*. Refractory materials. Vol. 7. 1971: Academic Press. 296.

2. Oyama, S.T., *The chemistry of transition metal carbides and nitrides*. 2012: Springer Science & Business Media. 536.

3. Martinez, A.I. and D.R. Acosta, *Effect of the fluorine content on the structural and electrical properties of SnO_2 and ZnO–SnO_2 thin films prepared by spray pyrolysis*. Thin Solid Films, 2005. **483**(1-2): p. 107-113.

4. Proscia, J. and R.G. Gordon, *Properties of fluorine-doped tin oxide films produced by atmospheric pressure chemical vapor deposition from tetramethyltin, bromotrifluoromethane and oxygen*. Thin Solid Films, 1992. **214**(2): p. 175-187.

5. Price, J.B., J.O. Borland, and S. Selbrede, *Properties of chemical-vapor-deposited titanium nitride*. Thin Solid Films, 1993. **236**(1-2): p. 311-318.

6. Kafizas, A., C.J. Carmalt, and I.P. Parkin, *CVD and precursor chemistry of transition metal nitrides*. Coordination Chemistry Reviews, 2013. **257**(13-14): p. 2073-2119.

7. Fix, R.M., R.G. Gordon, and D.M. Hoffman, *Synthesis of thin films by atmospheric pressure chemical vapor deposition using amido and imido titanium (IV) compounds as precursors*. Chemistry of Materials, 1990. **2**(3): p. 235-241.

8. Qiu, Y., et al., *Influence of nitrogen partial pressure and substrate bias on the mechanical properties of VN coatings*. Procedia Engineering, 2012. **36**: p. 217-225.

9. Liao, M.Y., et al., *Crystallographic structure and composition of vanadium nitride films deposited by direct sputtering of a compound target*. Journal of Vacuum Science and Technology A, 2004. **22**(1): p. 146-150.

10. Zgrabik, C.M. and E.L. Hu, *Optimization of sputtered titanium nitride as a tunable metal for plasmonic applications*. Optical Materials Express, 2015. **5**(12): p. 2786-2797.

11. Zgrabik, C.M., PhD. Dissertation, Harvard University: Cambridge, Massachusetts, 2016.

12. Lim, B.S., et al., *Synthesis and characterization of volatile, thermally stable, reactive transition metal amidinates*. Inorganic Chemistry, 2003. **42**(24): p. 7951-7958.

13. Wang, X., PhD. Dissertation, Harvard University: Cambridge, Massachusetts, 2012.

14. Yasaka, M., *X-ray thin film measurement techniques: V. X-ray reflectivity measurement*. The Rigaku Journal, 2010. **26**(2): p. 1-9.

15. Huang, T.C., R. Gilles, and G. Will, *Thin-film thickness and density determination from x-ray reflectivity data using a conventional power diffractometer*. Thin Solid Films, 1993. **230**(2): p. 99-101.

16. Chu, X., et al., *Reactive magnetron sputter deposition of polycrystalline vanadium nitride films*. Journal of Vacuum Science and Technology A, 1996. **14**(6): p. 3124-7.

17. Zasadzinski, J., et al., *Properties of superconducting vanadium nitride sputtered films*. Physical Review B, 1985. **32**(5): p. 2929-2934.

18. Comey, A.M. and D.A. Hahn, *A dictionary of chemical solubilities: Inorganic*. Second ed. 1921, New York: The MacMillan Company.

19. Rumble, J., *CRC handbook of chemistry and physics, 98th edition*. 2017: CRC Press.

3 Alloying of germanium into tin oxide by atmospheric pressure chemical vapor deposition

3.1 Chapter abstract

An APCVD method was developed for (Sn,Ge)O_2, using tetramethyltin, tetramethylgermanium, and oxygen at nominal deposition temperatures between 475 and 520 °C. Germanium incorporation of up to 8 at. % was achieved, which corresponds to replacing ca. 25 % of the tin with germanium. Tetramethylgermanium appeared to act as a retardant to the free radical reactions that drive SnO_2 deposition, resulting in negligible film growth for germanium incorporation over 8 at. %. A set of samples with 0, 0.3, 2.2, 5.5, and 7.1 at. % Ge were selected for detailed characterization of the band structure and electrical properties. XRD patterns showed peaks consistent with rutile SnO_2 for neat SnO_2, as well as 0.3 and 2.2 at. % Ge films; the films with higher germanium content do not diffract, but are too thin to expect observable diffraction. Resistivity decreased with increasing germanium incorporation, consistent with stable mobility and increasing carrier concentration. The measured carrier concentrations imply that all samples are degenerately doped. The optical absorption spectra showed patterns consistent with both crystalline-direct and amorphous-direct optical transitions, suggesting crystalline films with an increasing fraction of less well-ordered material with increasing germanium incorporation. The measured crystalline-direct optical gap increases slightly with increasing germanium incorporation, in a manner well fit by predicting the Fermi level from the carrier concentration. The measured valence band maximum decreases by ca. 0.5 eV moving from 0 to 0.3 at. % Ge,

and then slowly increases with increasing germanium incorporation. When combined with the nearly constant optical gap, this change in the valence band maximum dictates a corresponding trend in the conduction band minimum. There appears to be a non-negligible amount of amorphous material in all films, and the Fermi level at the film surface, measured by XPS, does not match the bulk values measured by the Hall effect (which reproduce the optical gap trend). Moreover, the surface Fermi level is constant for all germanium-containing films, as if surface band bending lowers the work function of the material from the bulk value by a similar mechanism in all cases. This observation is consistent with Fermi level pinning previously reported in tantalum- or antimony-doped tin oxide films, attributed to surface dipoles or enrichment of dopants at the grain surfaces.[1] This work shows that some tuning of the conduction band position is possible by alloying germanium into tin oxide. However, the high carrier concentration and likely presence of defects tailing into the bandgap are expected to preclude the use of this deposition method for (Sn,Ge)O_2 electron transport layers at any but the lowest concentrations of germanium.

3.2 Introduction

Global solar photovoltaic power capacity is expected to increase by nearly half a terawatt over the next 5 years.[2] To drive down the cost of these technologies and improve their scalabilty, researchers aim to increase device efficiency, reduce material cost, and focus on earth-abundant materials. In common parlance, solar cells are referred to by their absorber layer: the material that absorbs a photon to produce a spatially-separable electron-hole pair. This nomenclature may reflect a more general lack of emphasis placed on the additional layers that make charge transfer possible—beyond simple efficiency increases, these layers make a

functioning thin-film photovoltaic device possible. Figure 3.2.1 shows a schematic of a thin-film solar cell.

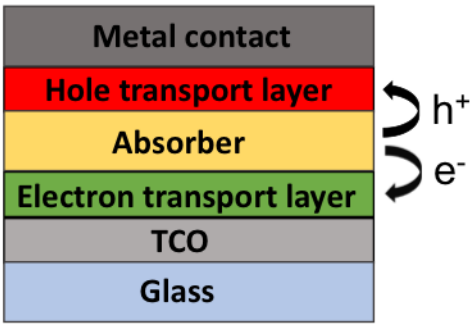

Figure 3.2.1: Schematic of a thin-film photovoltaic device. Electrical contact is made to the metal contact and transparent conducting oxide (TCO) layer.

The hole and electron transport layers flanking the absorber serve as selective conductors of the indicated charge carrier. In the absence of these materials, the vast majority of holes and electrons moving directly from the absorber to the current collecting layers recombine, resulting in negligible photocurrent. The interplay of the band structure of the absorber and transport layers determines the interfacial resistance, electron-hole recombination rate, and other efficiency losses incurred at the interface.

The ideal electronic structure for a charge-carrier transport layer depends on the electronic properties of the absorber as well as on the properties of the interface between these layers, and must normally be optimized through empirical testing for a given material. A significant disparity in carrier concentration across the absorber-transport layer interface can result in efficiency losses from carrier recombination; this fact represents a further complication to selecting materials with optimal band structures. A material with a tunable conduction band position permits optimization and avoids the need to perfectly match *a priori* the conduction band maxima of the transport and absorber layers. As new thin-film absorber layers are

developed, new thin-film carrier transport layers must also be explored, in order to optimize photovoltaic device performance.

SnO_2, tin oxide, is a wide band gap, n-type semiconductor. Fluorine-doped tin oxide, SnO_2(F), has found wide application in solar cells as the transparent conducting oxide (TCO) layer. Tin oxide has been doped with a wide variety of elements, including antimony,[3] cobalt,[4, 5] aluminum,[6, 7] fluorine,[8-11] and gallium.[12] These dopants[i] increase the electron concentration of tin oxide, often to degenerately doped levels, and thereby enhance its conductivity. However, considerably less attention has been paid to tuning the conduction band position of tin oxide. Consequently, literature describing doping or alloying with tetravalent metals, such as germanium, is sparse. (Sn,Ge)O_2, tin-germanium oxide, has been deposited by sol-gel[13] and magnetron sputtering[14], but the band structure of germanium-alloyed tin oxide has never been mapped. Given the difference in bandgaps of rutile SnO_2 (ca. 3.5 to 4 eV[8, 15, 16]) and rutile GeO_2 (ca. 4.7 to 5.6 eV[17, 18]), one might expect (Sn,Ge)O_2 to have a bandgap that varies with the alloy ratio, and permits conduction band position tuning. Such a material could function as an earth-abundant, tunable electron transport layer for solar cells. The carrier concentration could presumably be tuned independently, using the variety of known methods for doping tin oxide.

SnO_2 can be deposited numerous methods, including ALD,[19, 20] CVD,[10, 21, 22] sol-gel,[23] and spray pyrolysis.[16] GeO_2 films can be deposited by methods such as RF magnetron sputtering,[24] thermal evaporation,[25] and plasma-enhanced CVD[26]. By contrast, tin-rich (Sn,Ge)O_2 has only been reported in thin film form in a few publications.[17, 18] Chapter 1 describes a SnO_2 and SnO_2(F) deposition method that has previously been incorporated into

[i] Cobalt doping is used for ferromagnetic properties.

industrial-scale processes: the reaction of tetramethyltin (TMT) and oxygen at atmospheric pressure between 450 and 520 °C. One might expect tetramethylgermanium (TMG) to serve as a germanium source in this reaction, just as TMT does for tin oxide, providing a tin-germanium oxide alloy of tunable composition.

This reaction was studied in the APCVD chamber described in Chapter 1. Tetramethylgermanium was mixed with nitrogen by the same procedure used for tetramethyltin, and the relative and absolute concentrations of TMT and TMG were varied to produce film compositions ranging from 0 to ca. 8 at. % Ge (assuming that metal atoms comprise 33 at. %). TMG was observed to act as a reaction suppressant; the growth rate plummeted to negligible levels as the delivery ratio of TMG:TMT was increased and germanium incorporation exceeded ca. 8 at. %. The electrical and optical properties of films covering the available range of germanium concentrations were assessed. In light of the desirability of evaluating $(Sn,Ge)O_2$ as a potential electron transport layer, efforts were made to map the changes in carrier concentration, mobility, resistivity, and band structure resulting from the incorporation of germanium into SnO_2. Crystallinity data from XRD showed small crystallites in the 0, 0.3, and 2.2 at. % Ge samples, and no peaks in the other samples. However, the other samples are too thin to be well characterized by XRD. The carrier concentration increases with germanium incorporation, consistent with an increase in oxygen vacancies owing to tetramethylgermanium hindering the completion of the tin oxide deposition reaction. The electron mobility was modest, likely due to the small grain size of the material, but remained essentially unchanged with increasing germanium incorporation. Consistent with the trends in carrier concentration and mobility, the resistivity decreases as a film's germanium content increases.

Construction of a band structure diagram was approached through XPS measurements of

the valence band position and Fermi level and UV-Vis spectroscopy for the optical gap. The valence band position shifted upwards from 0.3 to 7.1 at. % Ge, perhaps due to electron-electron interactions caused by the high carrier concentration. The optical gap was not well defined for the films studied. While a reasonably strong crystalline-direct transition of ca. 4 eV was observed for the films with a crystalline phase detectable by XRD, acceptable crystalline-direct and amorphous-direct fits were found for all considered samples. The Fermi level was measured by XPS to be above the valence band position by a similar energy as the amorphous-direct transition, while the crystalline-direct transition was located between 0.4 eV and ca. 1 eV higher. However, the carrier concentrations obtained from Hall effect measurements suggest degenerate doping and cleanly reproduce a small Moss-Burstein effect, that is, an increase in the crystalline-direct optical gap with increasing germanium (and carrier) concentration. Considered together, these results imply that the Fermi level is always near the crystalline-direct conduction band position in the bulk material, but upon germanium incorporation is pushed downward at the surface of the film—where the XPS measurements interrogate—by band bending. Alloying tin and germanium oxides appears to afford a small degree of conduction band tuning, ca. 0.5 eV. The high carrier concentration and likely presence of defects in films prepared by this APCVD method likely require further optimization before $(Sn,Ge)O_2$ can be employed as an electron transport layer.

3.3 Materials and methods

3.3.1 Atmospheric pressure deposition of $(Sn,Ge)O_2$

Thin films of $(Sn,Ge)O_2$ were deposited using the atmospheric pressure chemical vapor

deposition system described in Chapter 1. Substrates held at 475 to 520 °C[ii] were exposed to a flow of 1 mol % tetramethytin in nitrogen, ca. 0.4 to 1.1 mol % tetramethylgermanium (Sigma Aldrich, 98 %), pure oxygen, and purified nitrogen carrier gas. The deposition and mixing procedures were identical to those described in Chapter 1, with the following changes: only silicon thermal oxide and quartz substrates were used; the bromotrifluoromethane tank was replaced with a tetramethylgermanium tank; and a flowmeter exhaust line and flowmeter bypass line, described below, were added to better control the timing of reagent delivery. The modified system is shown in Figure 3.3.1.

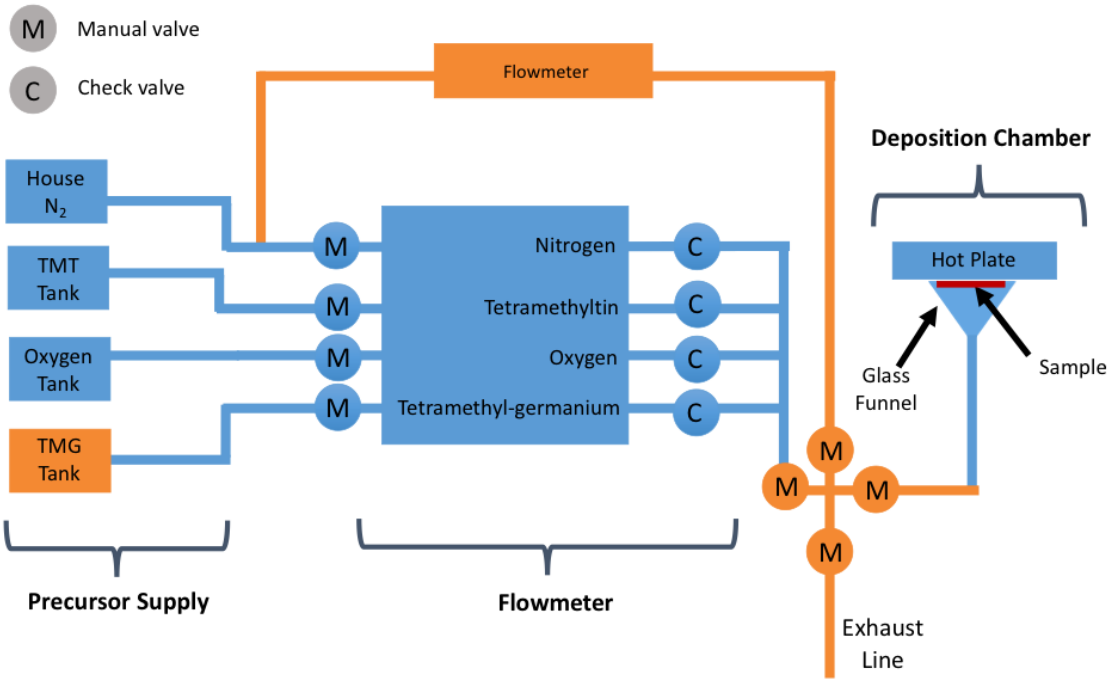

Figure 3.3.1: Atmospheric pressure chemical vapor deposition system for $(Sn,Ge)O_2$. The components marked in orange are the new bypass line, flowmeter exhaust line, and tetramethylgermanium tank.

[ii] As noted in Chapter 1, between 490 and 510 °C, the substrate surface was on average 89 ± 1 °C lower than the sample holder thermocouple reading. Temperatures reported in this work are uncorrected thermocouple readings from the sample holder.

The bypass line permits the user to direct either purified nitrogen or the stream of mixed reagents (including nitrogen) into the deposition chamber. When purified nitrogen is flowing to the chamber, the reagent stream flows into an exhaust line. This feature is useful for stabilizing the relative concentrations of reagents before beginning a deposition, and for quickly returning the chamber to a nitrogen atmosphere when a deposition is concluded. To deposit a film using the bypass lines, a nitrogen flow over the substrate was established using the new bypass line. After the desired temperature was achieved, the reactant gases were adjusted to the appropriate relative and absolute flow rates while the reactant gas stream was directed into the exhaust line. Once the flowrates had stabilized, the nitrogen purge was shut off, and the reactant gas stream was immediately directed into the deposition chamber. The deposition time was marked as beginning as soon as the gas streams were turned on. The system temperature was monitored and adjusted during the deposition, and kept to ± 2 °C unless otherwise noted. The deposition was ended by re-directing the reagent gas stream to exhaust and beginning a 400+ sccm nitrogen purge. After 5 minutes of purging, the heater was turned off. This shut-down procedure was established after XPS evidence suggested that film compositions changed sharply at the beginning and end of depositions. It is suspected that differing reactant concentrations due to different turn-off rates were the origin of this variation, which prompted the installation of bypass line for rapid turn-on/turn-off and the implementation of the high flowrate nitrogen purge.

3.3.2 Physical properties

Film thickness measurements were obtained either by scanning electron microscope (SEM) cross-section, in the case of silicon thermal oxide (300 nm of wet oxidation SiO_2 on Si) wafer substrates, or by Focused Ion Beam-milled (FIB-milled) cross-sections in the case of quartz substrates. For FIB samples, the thickness was defined as the distance between the film-

substrate interface (typically very smooth) and the centerline of the film's surface features. This distance is labeled in Figure 3.3.2. The roughness was estimated from the cross-section SEM micrograph, and half of this value was used as the error. Samples on SiO_2 substrates were prepared by cleaving the wafer to generate a fresh cross-section surface. All SEM micrographs were collected using a Zeiss Supra 55 scanning electron microscope. For the 5.5 at. % sample, the thickness was estimated by predicting the total atoms/cm^2 of germanium and tin, using densities of 6.994 and 6.278 g/cm^3 for rutile SnO_2 and GeO_2, respectively. Because using the RBS-XRF calibration curve (described below) overestimates the film thickness,[iii] half of the predicted value was used as the thickness and error.

FIB cross-sections were prepared by coating the sample in a ca. 25 nm layer of carbon in a Baltec MED-20 carbon coater, and then placing a ca. 10 μm × 1.5 μm, 500 nm thick platinum layer on the region of interest via electron beam deposition (3 kV, 1.6 nA, 1.4 μs dwell time). All FIB cross-section imaging, Pt deposition, and milling were performed with a FEI Helios 660 FIB and electron microscope with assistance from Dr. Stephan Kraemer of Harvard University's Center for Nanoscale systems. The Pt layer served to protect the surface of the film during cross-section milling. The carbon layer reduced charging effects during imaging and provided visible demarcation between the film of interest and the protective Pt layer. The cross-section was prepared by milling an initial cross-section (30 keV, 0.43 nA, 1 μs dwell time), followed by a more gentle cleaning cross-section, designed to smooth the cross-section while minimizing damage artifacts (30 keV, 0.23 nA, 1 μs dwell time). Figure 3.3.2 shows a sample milled cross-

[iii] These films might be amorphous, nano-crystalline, or rough in comparison to their thickness. Furthermore, the RBS-XRF curve appears to overestimate the absolute atoms/cm^2 for very thin films. The 7.1 at. % film, for example, was estimated to be 60 nm using the calibration curves, and measured after FIB cross-section to be 30 nm thick.

section, with layers labeled.

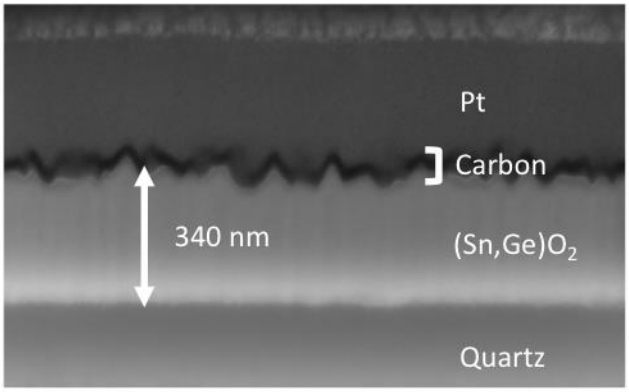

Figure 3.3.2: FIB cross-section for thickness determination.

Elemental compositions were determined via X-Ray Fluorescence spectroscopy measurements calibrated by Rutherford Backscattering Spectrometry. Both XRF and RBS spectra were obtained for calibration samples. For all other samples, only XRF data were obtained. Samples were deposited on quartz or SiO_2 substrates with a minimum size of 1 cm^2. XRF spectra were collected over a range of 0 to 25 keV binding energy on a Spectro Xepos III. Intensities for the Sn Lα1 and Ge Kα1 peaks were obtained by recording the counts per second at 3.443 and 9.881 keV, respectively, and subtracting the background spectrum of the relevant substrate. RBS measurements were performed by Dr. Ryan Thorpe (Department of Physics and Astronomy, Rutgers University). Measurements were obtained using a 2 MeV $^4He^{2+}$ ion beam perpendicular to the sample surface with the detector positioned at an angle of 17 degrees from the beam axis. A strong substrate signal can distort measurements if the substrate elements are equal to or higher than the film elements in atomic number. The uncertainty in the oxygen quantification was higher than that of tin or germanium because the samples were measured on quartz substrates, which contain oxygen and silicon. For very smooth films, it is possible to use a grazing angle measurement to emphasize the film signal. Here, film roughness (ca. ± 10 to 30

nm) was sufficient to cause shading effects, making grazing angle measurements infeasible. An alternate substrate, e.g. glassy carbon, can eliminate substrate interference, but deposition on glassy carbon was not practical due to the shape, small size, and high thickness of available substrates. The run-to-run composition variability of depositions made it challenging to achieve a specific, uniform composition on a small substrate. Large thermal oxide and quartz substrates permitted uniform areas of desired compositions to be selected for analysis.

To permit the rapid determination of sample composition by XRF, an XRF-RBS calibration curve was obtained via an x- and y-error-weighted linear regression (also called an orthogonal distance regression) of XRF counts vs RBS atoms/cm^2. A weighted linear regression was chosen so that points with less uncertainty have a greater influence on the fit. For three samples, some uncertainty exists in the location of the RBS scan (these samples are all below the line of best fit shown later). Accordingly, XRF scans were performed in three to four different locations on each sample, averaged, and assigned an x-error equal to the standard deviation plus 5 %. Based on typical XRF measurement variation, an x-error of 5 % was assumed for all other samples, except 0 at. % on the Ge fit, which was assigned an x-error of 28 counts/5 minutes (the approximate noise level of the instrument). RBS error was provided by Dr. Thorpe, based on his simulations of the data. At 0 at. % Ge, the y-error of the next-lowest Ge concentration was used. While no Ge is expected to appear in this sample, assigning a very low error (and hence a high weight) to this point underestimates the error in the fit at low concentrations, where an inherently lower signal-to-noise ratio should result in higher errors. The fit was obtained using the York method, a standard method for least-squares regressions weighted with x- and y-error.[27] The inverse of the square of the error in x and y was used to weight each point in the fit.

Figure 3.3.3 and Figure 3.3.4 shows the XRF-RBS correlations for tin and germanium,

overlaid with the weighted line-of-best-fit and 95 % confidence intervals. The tin oxide calibration curve (Figure 3.3.3) has the broadest confidence intervals at higher concentrations, owing to the influence of samples with higher x-errors. The increase in x-error at lower concentrations also results in broadening confidence intervals approaching the lowest concentration measured. Figure 3.3.4 shows the Ge calibration curve. Here, the influence of the weighting choice at 0 at. % Ge is evident in the widening confidence intervals approaching 0 at. % Ge.

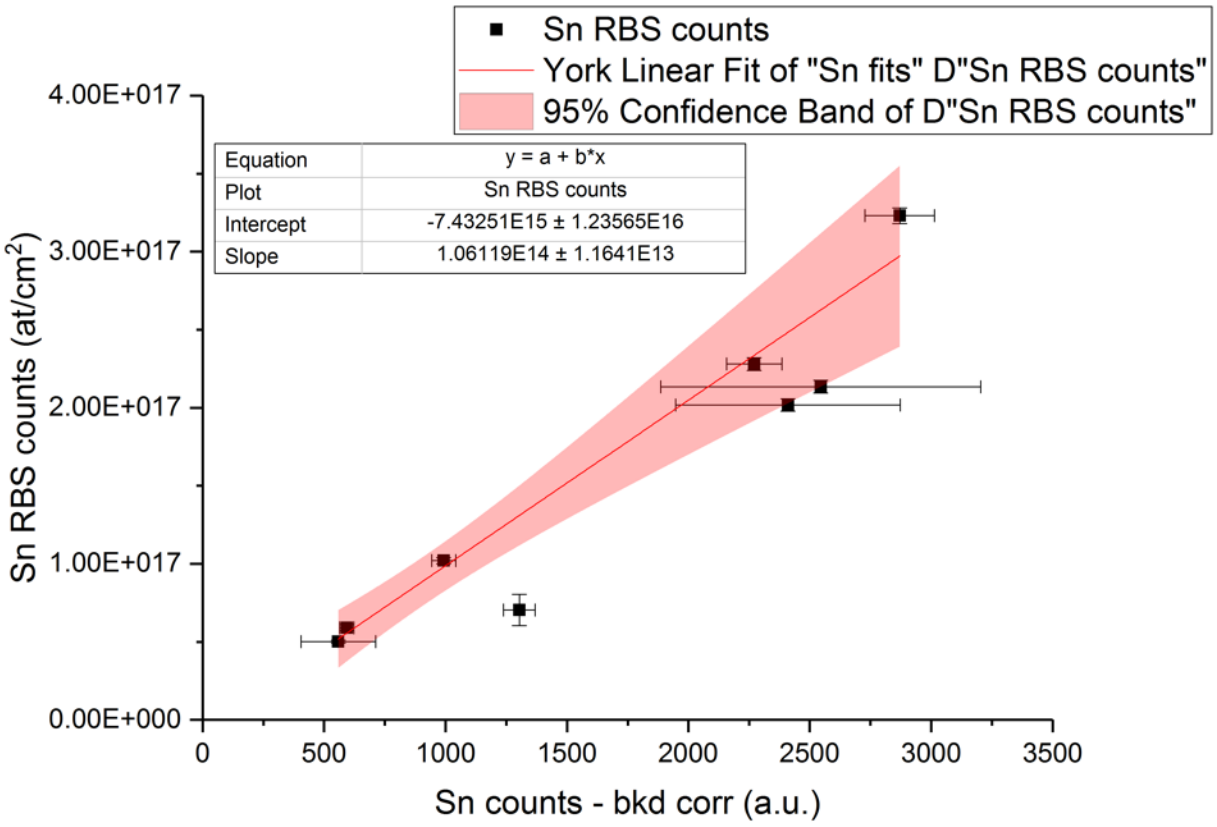

Figure 3.3.3 XRF-RBS calibration curve for Sn. The line represents a weighted linear regression of Sn at/cm^2 (RBS) vs Sn counts/5 min (XRF), and the shaded region depicts the 95 % confidence interval. The fit equation was determined to be: XRF counts = $1.06119 \times 10^{14} \times$ RBS counts - 7.43251×10^{16}.

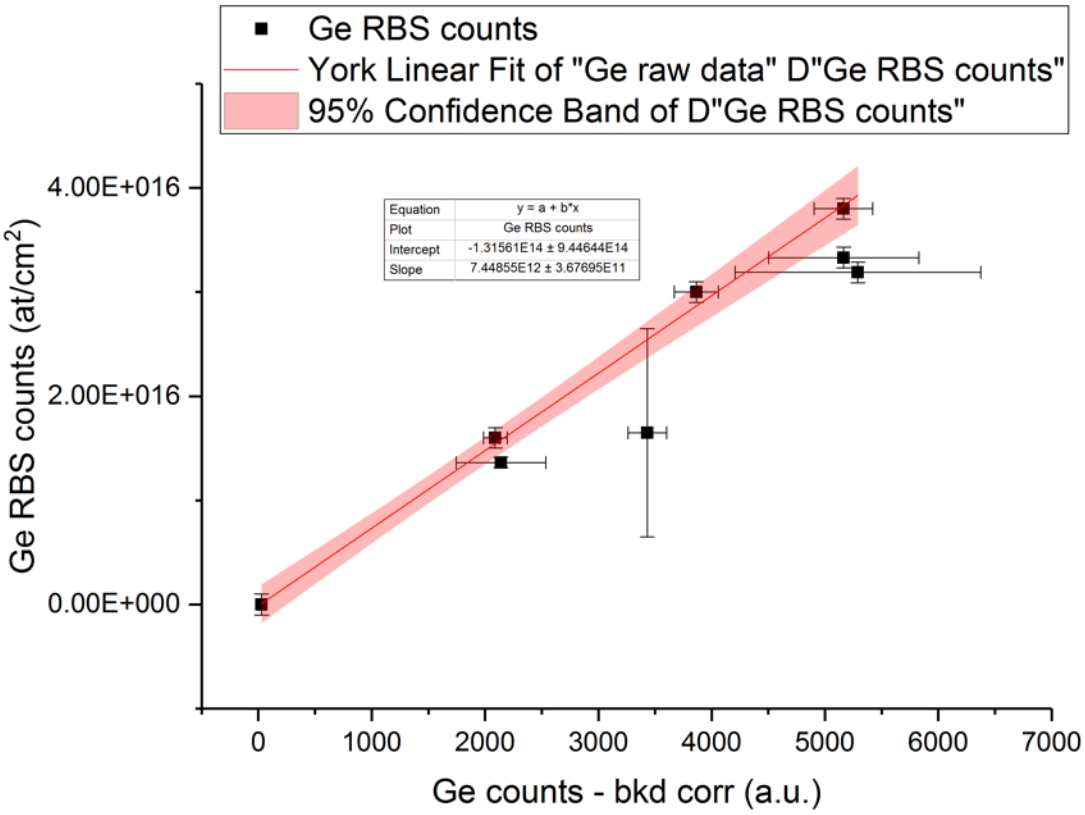

Figure 3.3.4: XRF-RBS calibration curve for Ge. The line represents a weighted linear regression of Ge at/cm^2 (RBS) vs Ge counts/5 min (XRF), and the shaded region depicts the 95 % confidence interval. The fit equation was determined to be: XRF counts = $7.44855 \times 10^{12} \times$ RBS counts – 1.31561×10^{14}.

After establishing a method to estimate the composition based on calibration curves and XRF data, it was necessary to determine the spatial uniformity of the composition for the samples used for electronic and band structure measurements. The (Sn,Ge)O_2 deposition method used sometimes produces samples with spatial variations in germanium composition up to several atom percent over ca 3-4 inches. The spot size of the employed characterization techniques varies from 1 cm (Hall) to 0.4 mm (XPS) in diameter, as illustrated in Figure 3.3.5. To ensure that the different measurements were conducted on regions of equivalent composition, the spatial uniformity of the samples were determined.

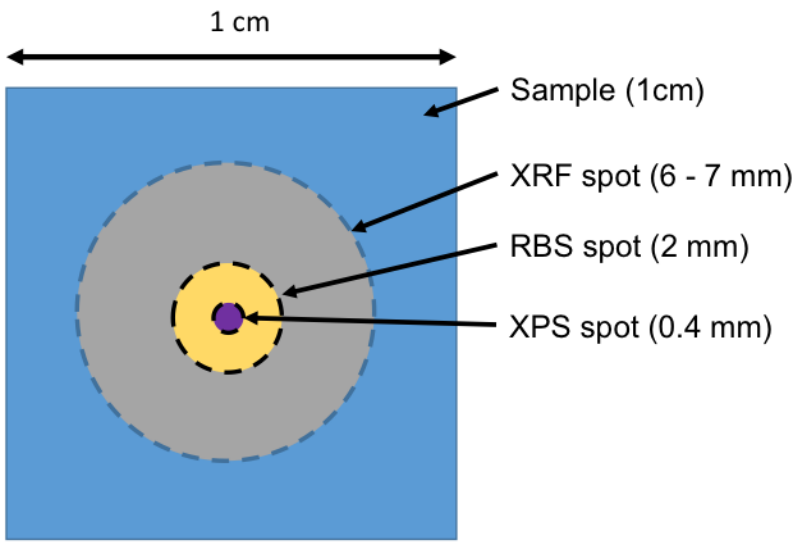

Figure 3.3.5: Illustration of the spot size of XRF, RBS, and XPS compared with the sample size. Hall measurements used the full sample area of 1 cm^2.

The 0.3 at. % Ge sample is below the accurate detection limit for XPS, so RBS measurements were performed on an array of 5 spots (at a spot in the center of the sample, and ca. 1 mm from each corner) covering the 1 cm^2 Hall measurement area. For the 2.1 and 7.1 at. % Ge samples, 9 sets of high-resolution XPS surface scans were performed such that the test spots formed a 6 mm × 6 mm square array surrounding the center of the sample. For speed, convenience, and preservation of the sample for future measurements, no sputtering was performed during this measurement. From the composition data (atom/cm^2 for RBS, and at. % for XPS), the tin to germanium ratio at different locations was determined. Using the Sn:Ge ratio excludes carbon contamination (always present in XPS surface scans of air-exposed samples) from consideration. Total germanium compositions were estimated by assuming that metal cations (tin and germanium) comprise 33 at. % of the material. This assumption is supported by XPS and RBS results for numerous films, within the error of each measurement type. The reported composition error for 2.2 and 7.1 at. % Ge samples is the standard deviation of the 9

compositions obtained for each sample. The resulting XPS germanium compositions were plotted against the composition predicted by XRF measurements of the sample. A weighted linear regression using y-error was performed, and since samples with low germanium concentrations could not be quantified by XPS, the fit was constrained to pass through (0,0) to add a physically relevant constraint in this region of the fit. Figure 3.3.6 displays the XPS data and the line of best fit. This regression line was used to convert the error reflected in the XPS

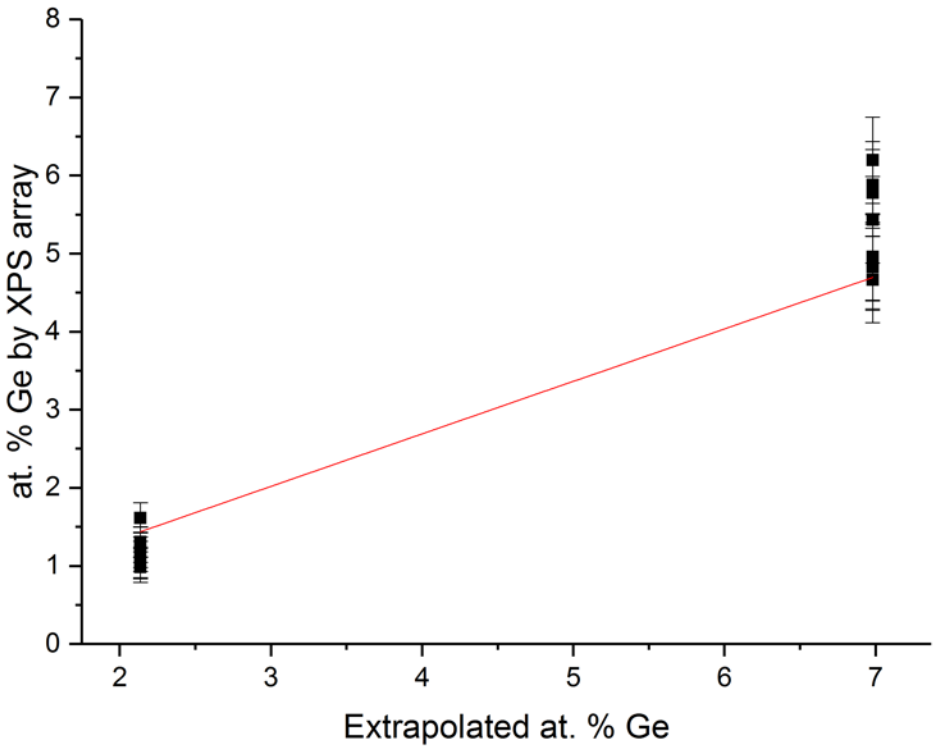

Figure 3.3.6: Germanium compositions estimated for 9 locations on three samples. The red line indicates the line obtained by weighted linear regression using the y-errors. The extrapolated at. % Ge assumes the sum of Ge and Sn is 33 at. %. The fit equation was determined to be: Ge at. % from XPS = 0.67256 × (Ge at. % from XRF).

compositions to an estimate of XRF-based composition error for these two samples. The 5.2 at. % sample was destroyed before uniformity could be assessed, so the XPS composition variation of the 7.1 at. % sample was used in conjunction with the XPS-XRF fit to estimate the

compositional variation. The composition error of 3 at. % sample were determined using the error of the RBS-determined germanium composition of the sample. These composition errors are used in all subsequent plots listing germanium concentration.

XPS high-resolution element scans were used to determine the variation in film composition with depth. The instrumentation and methodology will be described in Section 3.3.4, along with other XPS measurements. X-ray diffraction patterns were collected using a θ-2θ scan on a Bruker D8 Discover in XRR/HRXRD mode. Scans were performed using Cu Kα (λ = 1.542 Å) radiation, a dwell time of 1 second, an increment of 0.03 degrees, and a minimum scan range of 20 to 60 degrees. Crystallite size was calculated by the Debye-Scherrer equation,

$$\tau = \frac{K\lambda}{\beta \cos\theta} \qquad [3.3.1]$$

where τ is the effective crystallite domain size, K is the shape factor (0.9), β is the line broadening at full width half maximum (approximated by the FWHM), and θ is the Bragg angle. Errors were calculated via error propagation.

3.3.3 Electrical properties

The mobility, carrier concentration, and resistivity of films were determined by AC Hall Effect measurements on a custom system built by Dr. Oki Gunawan of IBM and Dr. Tai Kong Fai of Nanyang Technological University. Details of the system design and performance are available through a publication[28] and Dr. Fai's thesis.[29] Unlike DC Hall effect measurements, which require the researcher to collect current-voltage (IV) curves at different discrete magnetic polarizations, the magnetic field varies sinusoidally during the AC Hall measurement, allowing data to be collected continuously at different magnetic polarizations. A reasonably uniform magnetic field (± 5 % over a 1 cm^2 sample) is produced between two

rotating electromagnets. By varying the coil current, the strength of the magnetic field can be smoothly varied between an established maximum and minimum. Magnetic field has a known periodicity, permitting amplification of the Hall signal and reduction of background signals via a specialized data analysis technique called lock-in analysis (LIA). The AC Hall method offers improved signal to noise ratio, permitting measurement of films with low mobility and low carrier concentration. Before the Hall measurement is performed, a series of IV curves are measured between the different contacts; a linear IV plot indicates that the contacts are ohmic. Once the contact quality is verified, the Hall measurement is performed to determine carrier concentration, mobility, and sheet resistance. Because protruding surface features are not expected to contribute to conduction in the Hall measurement, calculations were performed with modified thickness values: the measured film thickness minus half the estimated roughness. Scans were conducted for 2800 seconds at a magnet field frequency of 3 rpm.

Films were prepared on insulating substrates (SiO_2 or quartz), and a square 1 cm × 1 cm region of interest was electrically isolated on each using a diamond scribe. The sample size was chosen to provide a balance between maximizing magnetic field uniformity (which decreases with increasing sample size) and allowing for consistent shape and size of the analysis area and more repeatable and accurate contact positioning (which becomes significantly easier as sample size increases).[iv] Contact pads for Hall measurements were placed in the extreme corners of the isolated region. Thin slices of 1 mm diameter indium wire were placed on either side of the copper Hall probes, then pressed into the sample surface to establish ohmic contact. Indium is malleable at room temperature, and thin cross-sections of indium wire can be adhered to a

[iv] Resistivity, carrier concentration, and mobility measurements were in agreement for a 1 cm^2 indium oxy-sulfide sample tested with this system and an established system at MIT.

sample surface with moderate, even pressure (the back of a diamond scribe was used here). This method of attaching Hall leads proved substantially faster, more repeatable, and more accurate in contact placement than indium soldering or wire bonding. Adhesion is sufficient for Hall measurements (the contacts passed the "tape test"), and after testing is finished, the indium can be removed cleanly from the surface by pulling firmly on the contact wires. Note that for samples with poor film-substrate adhesion (not the case for $(Sn,Ge)O_2/SiO_2$, but observed by Rachel Heasley for CuI/SiO_2), removing contacts can damage or de-laminate the film.

3.3.4 Band structure

Evaluating $(Sn,Ge)O_2$ alloy as a tunable electron transport layer (ETL) requires determining the variation in electronic band structure with increasing Ge incorporation. Ideally, an ETL can be tuned through a range of conduction band minima (CBM) by altering deposition parameters (and thus the composition) to achieve the optimum conduction band offset (CBO) from an absorber layer of interest. The ideal doping level must be optimized for each absorber material, but one can assess the applicability of the ETL for a range of absorber materials by determining the absolute positions of the valence band maximum (VBM), Fermi level, and CBM. While the CBM cannot be measured directly by XPS, it can be indirectly determined by adding the valence band maximum to the optical gap (described in section 3.3.4.2), as shown in Figure 3.3.7.

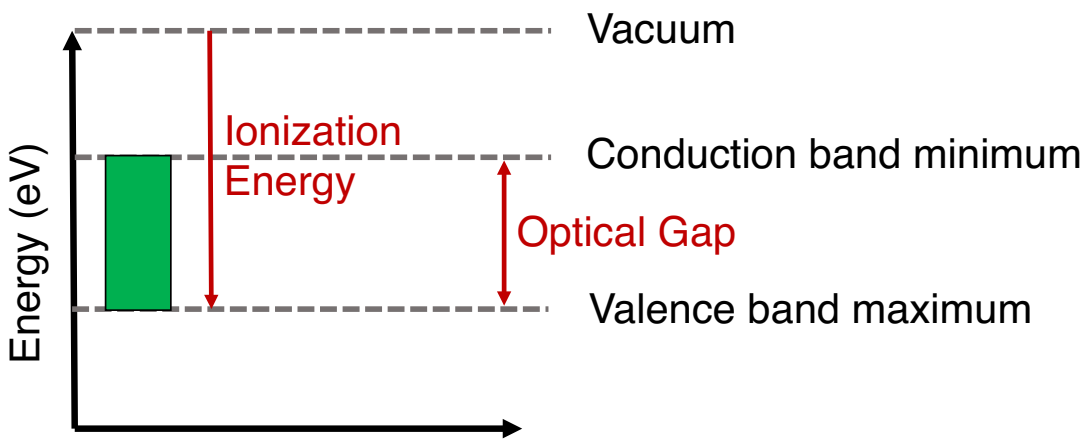

Figure 3.3.7: Schematic of the band structure of a semiconductor. The ionization energy and band gap are indicated by red arrows.

3.3.4.1 Determination of optical gap

The optical gap of a material can be determined by fitting an appropriate model to the absorption edge of the absorption spectrum of the material in the range of ultraviolet to visible light. Optical reflectance and transmittance spectra were collected between wavelengths of 200 and 1100 nm on an Agilent Cary 7000 Universal Measurement Spectrophotometer, using the integrating sphere attachment. An aperture was used to limit the effective sample size to 1 cm in diameter. Calibration for 100 % transmission and 0 % reflectance were performed with no sample or substrate in the analysis chamber. Calibration for 0 % transmission was performed by blocking the beam at the entrance to the integrating sphere. 100 % reflectance was calibrated using a diffuse reflective standard (Spectralon) with > 99 % diffuse reflectivity.

While the collection of UV-Vis spectra is relatively straightforward, the data processing and modeling required to obtain a reliable optical gap can be fraught with challenges. First, the absorption coefficient of the sample must be calculated from transmittance and reflectance data. Absorption data collected in this manner often show evidence of interference fringes due to

reflections from the back surface of the film or substrate. These fringes can distort, or at a minimum add uncertainty to, the linear fit necessary to deduce the optical gap. By relating the absorption coefficient to the absorbance (and hence T and R) through a ratio of A/T, one can neglect all terms with a phase dependence. This effectively eliminates the impact of interference fringes on the absorption coefficient. The final form of this approximation, advanced by Ritter and Weiser[30], is as follows:

$$\alpha = \frac{1}{d}\ln\left\{\frac{1}{2}(1-R_2)\left(\frac{1-R}{T}\right) + \left[(1-R_2)^2\left(\frac{1-R}{T}\right)^2 + 4R_2\right]^{1/2}\right\} \qquad [3.3.2]$$

where α is the absorption coefficient, d is the film thickness, T is the transmittance, R is the reflectance of the front surface of the film, and R_2 is the reflectance of the film-substrate interface. This treatment assumes a non-absorbing substrate. If R_2 can be neglected due to a very thick or highly absorbing film, this expression simplifies to:

$$\alpha = \frac{1}{d}\ln\left\{\left(\frac{1-R}{T}\right)\right\} \qquad [3.3.3]$$

Using these assumptions, one can evaluate equation 3.3.3 by substituting the measured reflectance and transmittance of a film on a substrate for R and T, respectively.

If a non-absorbing substrate cannot be assumed, but back surface and interface reflections can be neglected, the data can be corrected by dividing the measured transmittance by the transmittance of the bare substrate and leaving the reflectance unaltered. This correction method is frequently used for measurements of photovoltaic absorber materials. Because (Sn,Ge)O_2 films are weakly absorbing, the substrate-film interface reflections, substrate absorbance, and back surface reflections cannot be neglected. Indeed, performing the "standard" correction on this material yields a non-physical negative absorbance in the visible range. The process of fully accounting for these infinitely propagating reflections and subsequent absorptions using the

transmittance and reflectance formulae is time-consuming, tedious,[v] and ultimately unnecessary for $(Sn,Ge)O_2$. The complete equations for transmittance and reflectance of the film-substrate system and bare substrate have 5 unknowns, and only 4 measurements (T and R for the film-substrate pair and the bare substrate) can be made. These equations and the relevant film schematics are contained in Figure 3.3.8. By instead calculating effective absorption coefficients for the film-substrate and bare substrate, an appropriate substrate correction can be applied using only the four measurements mentioned. This correction technique is hereafter referred to as the Cesaria correction.[31]

Equation 3.3.4 describes the primary assumption of the Cesaria correction: that the absorption coefficients of the film and substrate can be related to an effective absorption coefficient calculated from the measurements of the film-substrate system. The film and substrate thickness are d_{film} and d_{sub}, respectively. The absorption coefficient of the film-substrate system is denoted by α_{tot}, whereas α_{film} and α_{sub} refer to the absorption coefficient of the free-standing film and substrate, respectively. Approximating the sum of the film and substrate thicknesses as equal to the substrate thickness and solving for α_{film} yields equation 3.3.5.

$$e^{\alpha_{tot} d_{tot}} = e^{\alpha_{film} d_{film} - \alpha_{sub} d_{sub}} \qquad [3.3.4]$$

$$\alpha_{film} = \frac{d_{sub}}{d_{film}} (\alpha_{tot} - \alpha_{sub}) \qquad [3.3.5]$$

To apply this correction, reflectance and transmittance measurements on the film-substrate system and the bare substrate are used to calculate the absorption coefficients according to the Ritter-Weiser approximation. Each of these samples are treated as free-standing films, which is true in the case of the bare substrate, and valid for the film-substrate combination provided that

[v] The relevant academic prose is replete with descriptors such as "depressingly complex" (see Heavens, O. S., *Optical Properties of Thin Solid Films*. 1991: Courier Corporation.)

equation 3.3.4 holds. Figure 3.3.8 is a schematic of the substrate and film-substrate system.

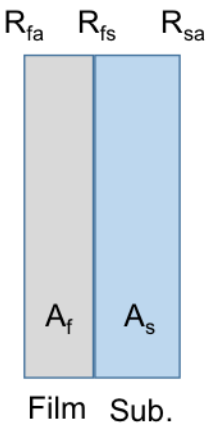

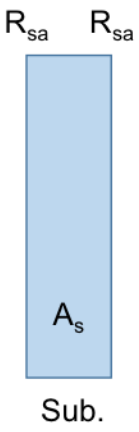

Sample measurement

$$T_{tot} = T_{tot}(R_{fa}, R_{fs}, R_{sa}, A_f, A_s)$$
$$R_{tot} = R_{tot}(R_{fa}, R_{fs}, R_{sa}, A_f, A_s)$$

Bare substrate measurement

$$T_{sub} = T_{sub}(R_{sa}, A_s)$$
$$R_{sub} = R_{sub}(R_{sa}, A_s)$$

Figure 3.3.8: A schematic of the key material properties and equations relevant to comprehensive substrate correction.

The Cesaria correction accounts for the presence of a substrate. Next, a suitable model of the electronic transition must be applied to locate the absorption edge. The functional form shown in equation 3.3.6 is assumed to apply at the absorption edge;

$$(\alpha h\nu) = A(h\nu - E_g)^r \qquad [3.3.6]$$

here h is Planck's constant, ν is the frequency of the transmitted or reflected light, A is a fitting parameter, and E_g is the optical gap. The value of r is expected to be 2 for direct, crystalline transitions, and ½ for direct, amorphous or indirect, crystalline transitions. Solving for a form of equation 3.3.7 that is more amenable to fitting, one obtains

$$(\alpha h\nu)^{\frac{1}{r}} = B(h\nu - E_g) \quad [3.3.7]$$

where B is a fitting parameter. Using the Cesaria-corrected absorption coefficient to plot $(\alpha h\nu)^{\frac{1}{r}}$ versus hν, fitting a least-squares regression to the linear portion, and extrapolating to an

absorption coefficient of zero, one can calculate the optical gap of a material. Figure 3.3.9 a and b show example transmittance and reflectance spectra, and the uncorrected, "standard"-corrected, and the Cesaria-corrected absorption coefficient. Figure 3.3.9 c and d show a direct/crystalline and direct/amorphous fit, respectively.

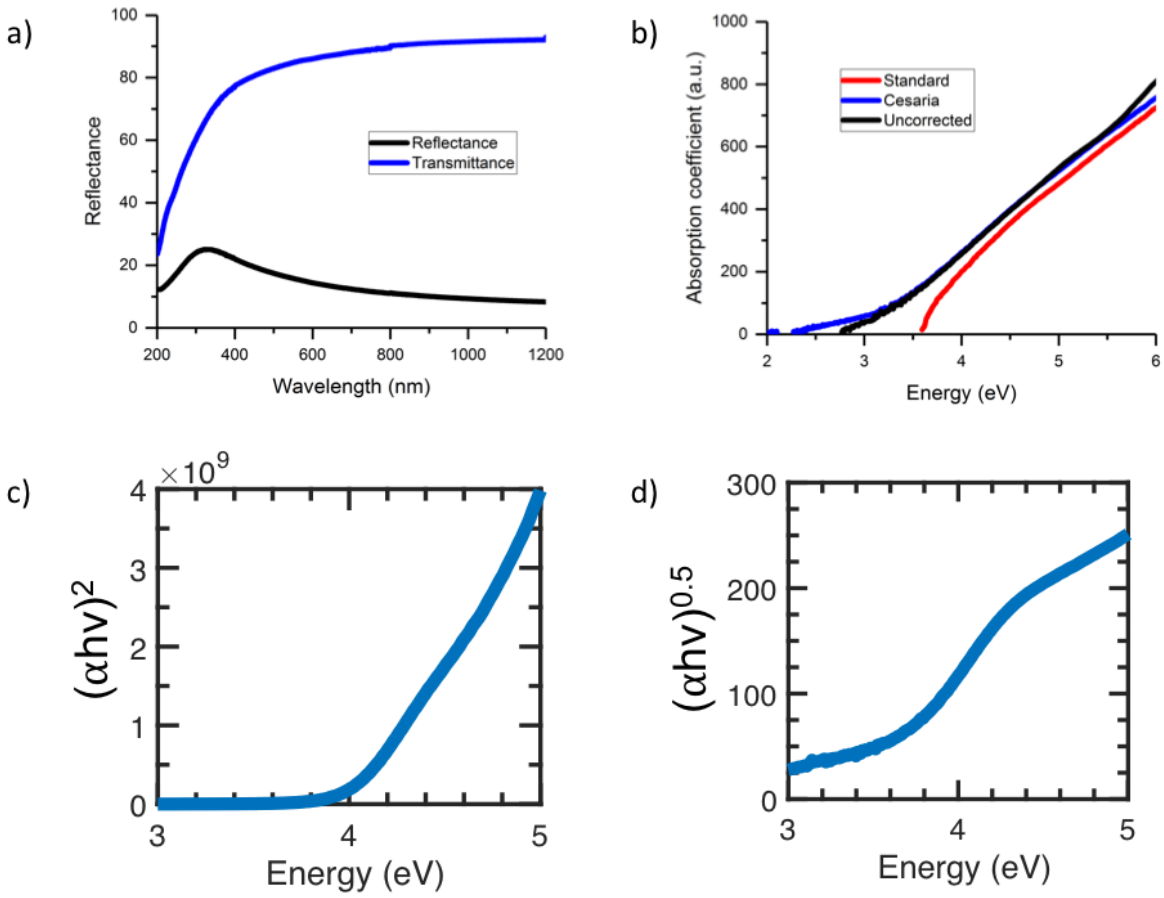

Figure 3.3.9: Data processing sequence required to obtain the optical gap from transmittance and reflectance data. a) transmittance and reflectance data for neat SnO_2, b) a comparison of the uncorrected Ritter-Weiser absorption coefficient, the "standard" correction applied by many researchers, and the Cesaria correction used in this work, c) absorption coefficient model assuming a direct, crystalline transition, d) absorption coefficient model assuming a direct, amorphous or indirect, crystalline transition.

There are two steps to determining the optical gap from the absorption coefficient: first, one must select and apply the appropriate transition model, and second, one must extract the band gap by determining the "most linear" region of the fit. Perhaps because the fitting task

seems straightforward, there do not appear to be any widely-shared criteria for determining either the most appropriate model or the most linear region. Most often, literature reports will initiate the calculation of a material's optical gap by plotting the absorption data using different transition models, and distinguishing by eye both the "best" model (i.e., which appears to produce a "more linear" region) and the appropriate portion of that plot to fit. Some list the results of both models and leave it to the reader to evaluate the fit quality. When the expected transition type is known, a surprising degree of uncertainty in the location of the appropriate fitting region remains. For example, a systematic re-fitting of ZnO band gaps from over one hundred papers shows substantial variability in the fitting region selected by the original authors, which gave rise to substantial variations—and in some cases inaccuracies—in the reported band gap.[32] In the case of unknown transition types, a) additional evidence should be collected to support the choice of transition model, and b) care should be taken to define and systematize the process of finding a linear region. In the absence of complementary measurements, conclusions regarding the type of transition should be treated with caution, as the fitting process, particularly for amorphous materials, can be highly subjective.

In order to minimize the aforementioned uncertainty, this work adopts a modified version of the systematic fitting process used in ref. [32] to determine the appropriate model and region for fitting $(Sn,Ge)O_2$ absorption coefficient data. Band structure and crystallinity data are used to support the choice of the transition model. Rather than fitting a single region with a given number of data points, for a set of increment sizes (e.g., 6, 11, 21, 41, 61, and 81 data points), series of linear fits were calculated by stepping through the absorption coefficient curve (i.e, the $(\alpha h\nu)^r$ vs. $h\nu$ plot, where r = 0.5 or 5), shifting the midpoint of the fit by one data point at a time. Using the correlation coefficient, R^2, as an indicator of linearity, a plot of R^2 vs. midpoint of fit

can be used to discover the most linear region of the absorption coefficient curve. Figure 3.3.10 shows such a sequence of plots. The more linear portions of the absorption coefficient model in Figure 3.3.10 a (the red and green circles) correspond with midpoints with higher R^2 values in Figure 3.3.10 b. Provided that the number of data points is sufficient to average out the effects of measurement noise, using fewer data point tends to produce higher R^2 values. In Figure 3.3.10 c, the plot in b is reproduced and overlaid for a variety of increment sizes.

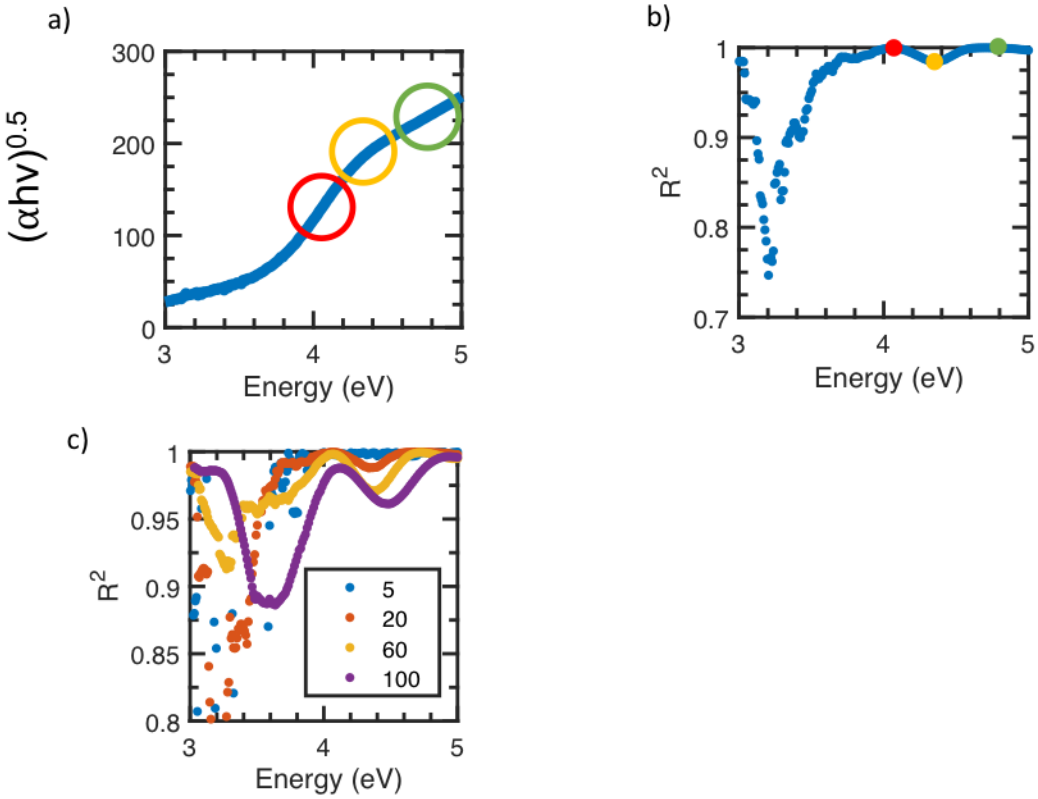

Figure 3.3.10: Plots of a) sample absorption coefficient curve, modeled as an amorphous-direct/crystalline-indirect transition, overlaid with circles indicating regions with different functional behavior, b) an R^2 plot, with the midpoints of those same regions labeled, and c) A series of R^2 vs. midpoint of fit plots, varying the number of data points included in the fit.

The approach of ref. [32] is to examine by eye a plot equivalent to Figure 3.3.10 c and a plot of R^2 vs. the calculated band gap (from the fits in plot c) to determine the appropriate band gap. To further systematize the selection method in the present work, a minimum R^2 value of 0.995 was set, and regions that yield improbably low optical gaps (e.g., 2 eV) were not

considered. By finding the curve (associated with a certain data point increment size) that produces the largest continuous range of data points above the minimum R^2 value, the boundaries of the most appropriate fitting range were established. The data were then fit using a y-error-weighted linear regression and the optical gap was calculated by extrapolating to an absorption coefficient of zero. Standard methods for calculating slope and intercept error were employed, and the error was propagated to the optical gap calculation.

Viezbicke's analysis method is useful in determining the best region to fit for a particular absorption coefficient model. Selecting the appropriate model is a distinct challenge that merits further discussion. Ideally, the data will yield a clear linear trace with one transition model, and a clearly non-linear (e.g., curved or oscillating) trace with all others. This was not the case with every sample considered in this work, and visual inspection of plots with different transition models did not lead to a clear choice. The underlying source of this difficulty became clear upon setting a uniform standard for "sufficiently linear" beforehand, in the manner described above—both models have some regions of high linearity. Figure 3.3.11 shows a sample with 7.1 at. % germanium, modeled as a crystalline-direct transition. Figure 3.3.12 models the same data as an amorphous-direct or crystalline-indirect transition. For samples in which the preferred model remained unclear from the absorption coefficient model plots, band structures were interpreted in light of corroborating evidence, especially the measured Fermi level of the material.

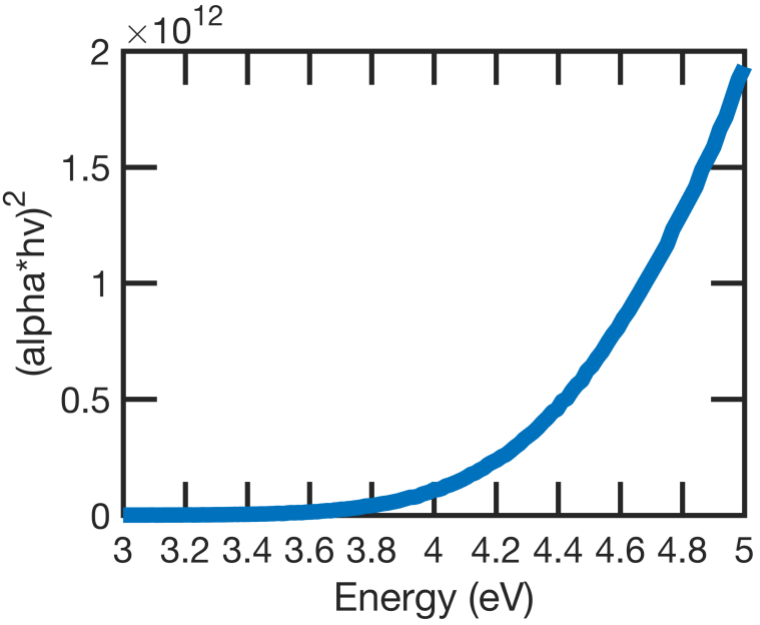

Figure 3.3.11: A sample with 7.1 at. % Ge, modeled as a crystalline-direct transition, or $(\alpha h\nu)^2$ vs. $h\nu$.

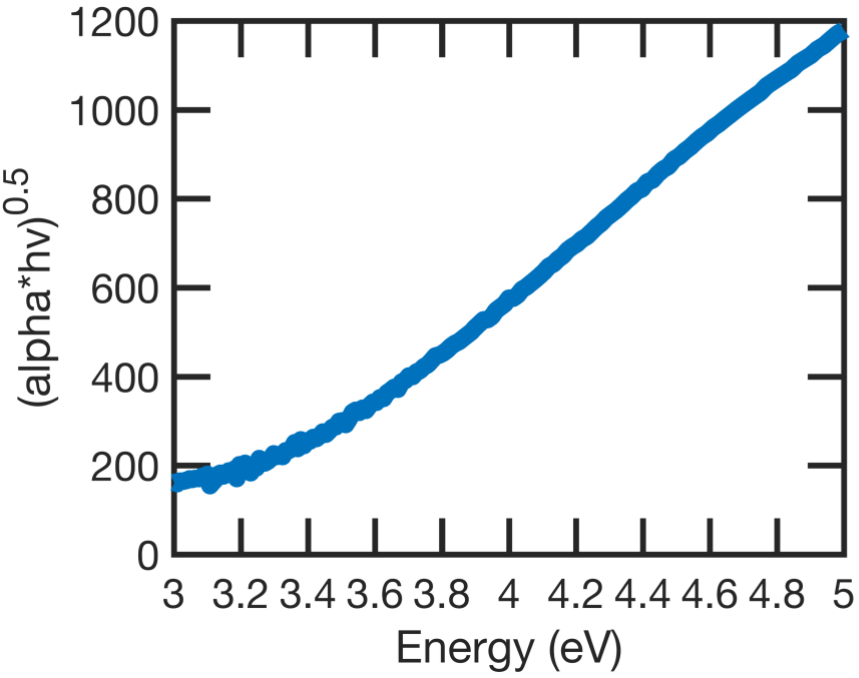

Figure 3.3.12: The same sample as the previous figure, but modeled as an amorphous-direct or crystalline-indirect transition, or $(\alpha h\nu)^{0.5}$ vs. $h\nu$.

A generalized error propagation formula of the form of equation 3.3.8 where y is the dependent variable, z_i is the ith independent variable, and σ_{z_i} is the error of z_i was used to propagate error from the Ritter-Weiser approximation (equation 3.3.3), where an extra 2 % error was added to the propagated value to account for the error of the approximation itself.

$$\sigma_y = \sqrt{\sum_{i=1}^{n} \left(\frac{\partial y}{\partial z_i}\right)^2 \left(\sigma_{z_i}\right)^2} \quad [3.3.8]$$

Next, error propagation was applied to the Cesaria correction (Equation 3.3.5) using the aforementioned film thicknesses and errors, as well as the absorption coefficient errors from the preceding step. For the direct-crystalline and direct-amorphous transition models, Equation 3.3.8 was applied to the transition model formulae, and the resulting error was used to weight the linear fit. Slope and intercept errors were determined by equations 3.3.9 and 3.3.10, where e_i and x_i are the error and x-value of the ith data point.

$$\sigma_{slope} = \sqrt{\frac{\left(\sum \frac{1}{e_i^2}\right)}{\left(\sum \frac{x_i^2}{e_i^2}\right)\left(\sum \frac{1}{e_i^2}\right) - \left(\sum \frac{x_i}{e_i^2}\right)^2}} \quad [3.3.9]$$

$$\sigma_{intercept} = \sqrt{\frac{\left(\sum \frac{x_i^2}{e_i^2}\right)}{\left(\sum \frac{x_i^2}{e_i^2}\right)\left(\sum \frac{1}{e_i^2}\right) - \left(\sum \frac{x_i}{e_i^2}\right)^2}} \quad [3.3.10]$$

The resulting errors were used to calculate the uncertainty of the optical gap.

3.3.4.2 Determination of valence band maxima and Fermi levels of (Sn,Ge)O_2 alloys

VBM and Fermi levels for films were measured using a Thermo Scientific K-Alpha spectrometer with a 12 kV electron beam and a monochromatized Al Kα X-ray source (1486.7 eV). Surface cleaning was performed in situ with an argon sputtering gun in monatomic (single atom) or cluster (2000 atoms) mode. Sputtering energies were 2 keV (monatomic) and 2 keV

(cluster), unless otherwise noted. The energy resolution was 0.05 eV for VBE, cut-off, and Fermi-to-VBE scans, and 0.1 eV for element scans. A pass energy of 50 eV was used for the Fermi-to-VBE scans, 10 eV for cut-off scans,[vi] and 50 eV for element scans. To establish electrical contact between the sample stage and the film, a copper clip pressed onto the surface of the film was used to hold the sample in place. The center of each sample was targeted for analysis, and the clip was placed as near as possible to the region of interest. Elemental compositions were determined using high resolution scans performed in the energy ranges relevant to elements of interest. The C1s, O1s, Si2p, Sn3d, and Ge2p3 peak areas were fitted with a "Smart" background and the built-in instrument calibrations were used for element quantification.

The VBM of a given film was established by measuring the secondary electron cut-off (SEC) and the valence band edge (VBE). A scan of the secondary electron cut-off region, shown in Figure 3.3.13 for a SnO_2 film, reveals the energy of the most tightly bound electrons that reach the detector. To prevent the overlap of the inelastically scattered electrons from the film with those of the detector, a bias of -30 V is applied during the SEC and VBE scans. This method shifts the secondary electron signal below that of the film, allowing for an accurate measurement of the SEC.[vii] A least-squares regression is performed on the flat background region at lower energy (marked in green in Figure 3.3.13) and the linear portion of the cut-off edge at higher energy (marked in blue). The value of the SEC is calculated by finding the intersection of these

---

[vi] Lower energy was used for cut-off scans due to instrument requirements. The method has been validated by CNS staff at these settings.

[vii] Please see the tutorial prepared by Dr. Rudy Schlaf of the University of South Florida for a concise explanation of sample biasing during work function measurements. (http://rsl.eng.usf.edu/Documents/Tutorials/PEScalibration.pdf)

two lines.

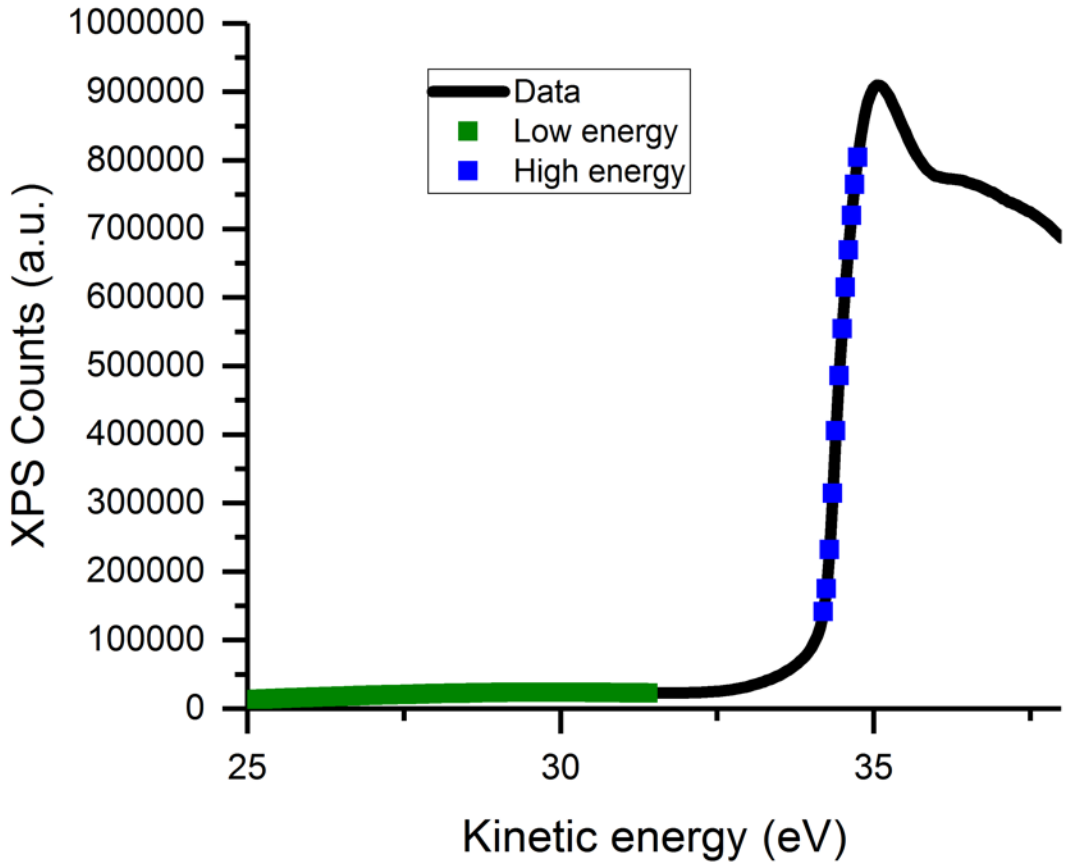

Figure 3.3.13: The secondary electron cut-off of a (Sn,Ge)O_2 film with 0.3 at. % Ge sample (described in Table 3.4.1), determined by XPS. The regions selected for the linear fits used to compute the cut-off energy are marked in blue and green.

The Valence Band Edge (VBE) marks the highest-kinetic energy electrons that reach the detector; for a semiconductor, this region is populated by electrons at the highest occupied levels of the valence band. A typical data set for SnO_2 is shown in Figure 3.3.14. As with the SEC, the location of the VBE is determined by the intersection of linear fits to the higher energy background signal (marked in green in Figure 3.3.14), and the lower energy linear portion (marked in blue). Keeping in mind that the SEC is, by definition, 1486.7 eV below vacuum (i.e., the energy of the exciting X-rays), the absolute valence band position, or Valence Band

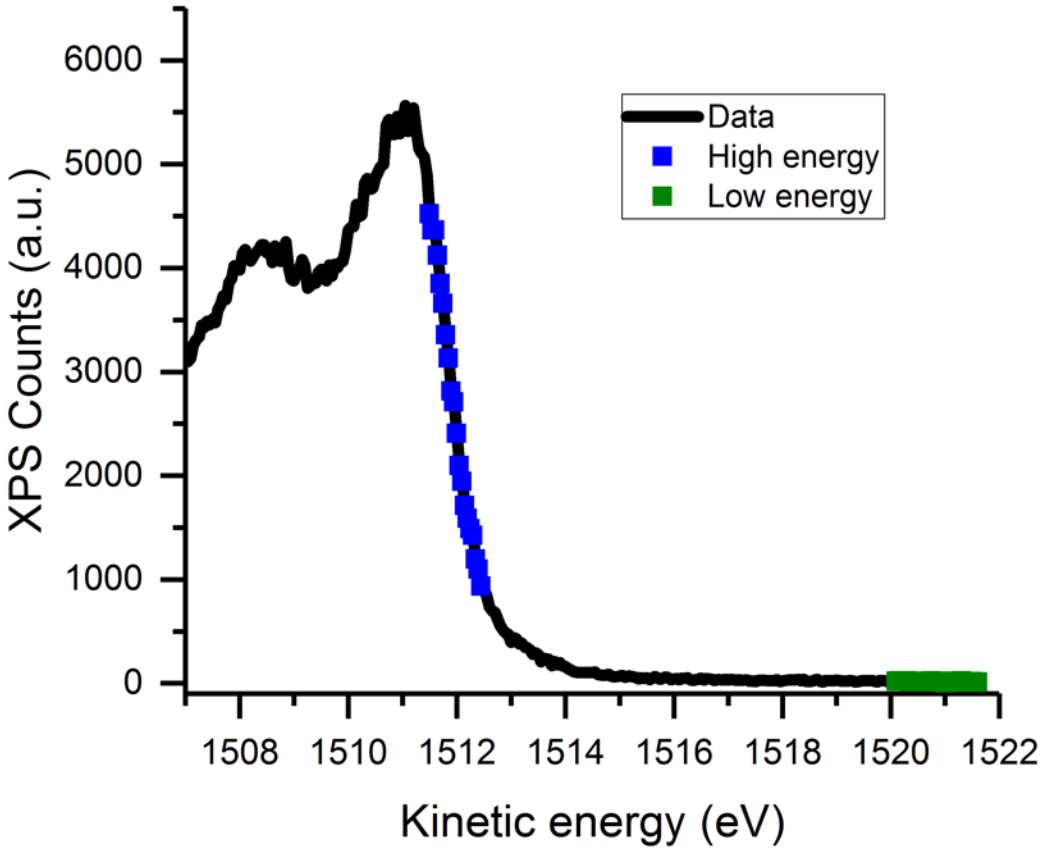

Figure 3.3.14: The valence band edge of a (Sn,Ge)O_2 film with 0.3 at. % Ge sample (described in Table 3.4.1), determined by XPS. The regions selected for the linear fits used to compute the valence band edge energy are marked in blue and green.

Maximum, can be determined by subtracting the spectrum width (VBE minus SEC) from the energy of the impinging photons. The negative of the VBM is the ionization energy, or the energy required to excite an electron from the top of the valence band to vacuum.

The location of the Fermi level can also be determined by XPS. When good electrical contact is made between the sample, the sample holder, and a reference gold film, the Fermi levels of these materials will be in equilibrium. The kinetic energy value of the Fermi edge of the gold reference was determined automatically with the XPS software. Given that the gold Fermi level is in equilibrium with the sample Fermi level, the energy difference between the sample Fermi level and sample VBM can be ascertained. By subtracting from the photon energy (1486.7

eV) the difference between the Fermi edge of gold and the SEC of the sample, the position of the sample Fermi level (i.e., the negative of the sample work function) can be computed.

3.3.4.3 Minimizing the impact of surface contamination on XPS measurements

XPS is a surface-sensitive technique, hence surface contamination due to exposure to ambient conditions complicates the accurate determination of the position of the Fermi level. Helander, et al.[33] observed a 0.25 eV reduction in the work function (energy gap between the Fermi level and vacuum) of otherwise identical fluorine-doped tin oxide ($SnO_2(F)$) samples with higher amounts of organic surface contamination (i.e., with at. % Sn:at. % C ratios of 12.5 vs. 2.6). A similar effect has been observed with $SnO_2(F)$ produced in this work. As Figure 3.3.15 shows, $SnO_2(F)$ subjected to cluster sputtering shows an increase in the measured work function,

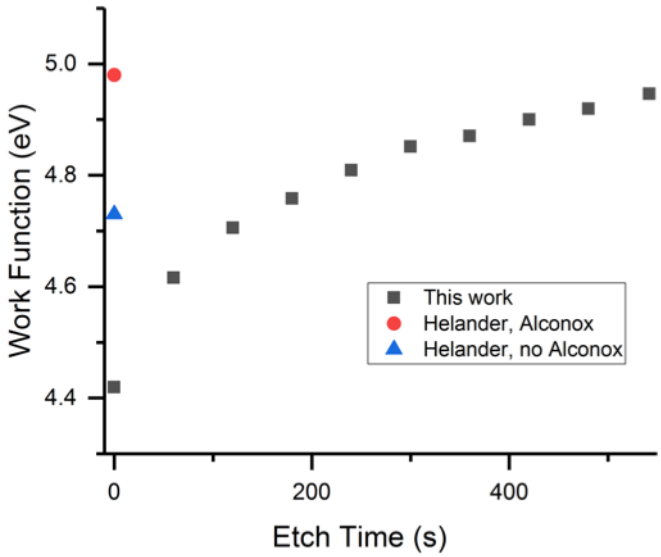

Figure 3.3.15: A comparison of $SnO_2(F)$ work function measurements from ref [33] and this work. Sample was subjected to 60 seconds cluster sputtering in between work function measurements.

presumably as carbon is removed from the surface. Points marked in orange and gray are taken from ref. [33]; these have Sn:C ratios of 12.5 and 2.6, respectively. The measured work function

approaches that of the relatively clean SnO_2(F) surface as sputtering proceeds.

Two techniques were employed to remove surface contamination: argon sputtering in situ and solvent cleaning before loading the sample. The first method is commonly used for composition depth profiles. In monatomic sputtering mode, a beam of single argon atoms is driven towards the film surface, removing weakly bound surface contaminants, and at sufficient energies, removing layers of film. While this method is effective at removing carbon, surface damage is a common consequence[viii] Even at the lowest available sputtering energy (200 eV) a scan of the valence band edge of SnO_2 showed the appearance of a shoulder peak associated with Sn^{4+} reduction to Sn^{2+}.[1] The presence of the shoulder in the sputtered sample and its absence in the untouched film suggest that the vast majority of the Sn atoms are in the 4+ oxidation state until sputtering induces a change to the 2+ state. Modification of the oxidation state of the material is clearly undesirable, hence the more gentle cluster sputtering mode was used. During cluster sputtering, the surface is bombarded by weakly charged, weakly bound groups of argon atoms, rather than individual atoms. By reducing the energy imparted by each sputtering atom, cleaning is ideally achieved with little or no damage to the surface. One drawback of cluster sputtering is that some carbon contamination is often left behind. In this work, avoiding surface damage and modification of the chemical state of the surface was prioritized over removing all carbon.[ix] The second technique for minimizing the surface carbon contamination during measurements was solvent cleaning. Samples were cleaned with solvents and detergents before loading into the instrument—the desire to leave the surface chemically unaltered discourages the

---

[viii] Please see information provided by the XPS manufacturer: https://xpssimplified.com/magcis_ion_system.php

[ix] At the very least, the carbon surface contamination can be tracked by XPS.

use of harsher chemical cleaning methods such as UV-ozone. To ascertain the optimal cleaning procedure for XPS samples, a commercial FTO sample was split into four pieces, each was subjected to one of the following solvent cleaning protocols: a) no cleaning (as received); b) sonication for 30 minutes each in acetone, then isopropanol; c) sonication in a mixture of Alconox and de-ionized water for 30 minutes, rinsing thoroughly with water, followed by procedure b; and d) rinsing in acetone, then isopropanol. All acetone and isopropanol were semiconductor grade. Upon completion of the final rinse or sonication bath, samples were dried with compressed nitrogen. The FTO is expected to be highly uniform in composition and surface morphology, thus any measured differences in surface composition, VBE, or cut-off are thought to be due to differences in cleaning. Figure 3.3.16 shows the XPS composition of these samples at the surface, and after cleaning with cluster sputtering for 2290 sec at 2 keV.

The carbon composition at the surface decreases as an increasingly aggressive cleaning method is employed, and the most intensive cleaning method, Alconox/acetone/isopropanol sonication, has the lowest carbon surface concentration after cluster sputtering. For exceptionally clean samples, cluster sputtering can remove much of the surface carbon, but for samples that have been exposed to air for an extended period of time, additional cleaning is necessary. Accordingly, samples were cleaned by sonication in Alconox, acetone, isopropanol before XPS measurements. The carbon composition at the surface decreases as an increasingly aggressive cleaning method is employed, and the most intensive cleaning method, Alconox/acetone/isopropanol sonication, has the lowest carbon surface concentration after cluster sputtering. For exceptionally clean samples, cluster sputtering can remove much of the surface carbon, but for samples that have been exposed to air for an extended period of time, additional cleaning is necessary. Accordingly, samples were cleaned by sonication in Alconox,

acetone, isopropanol before XPS measurements.

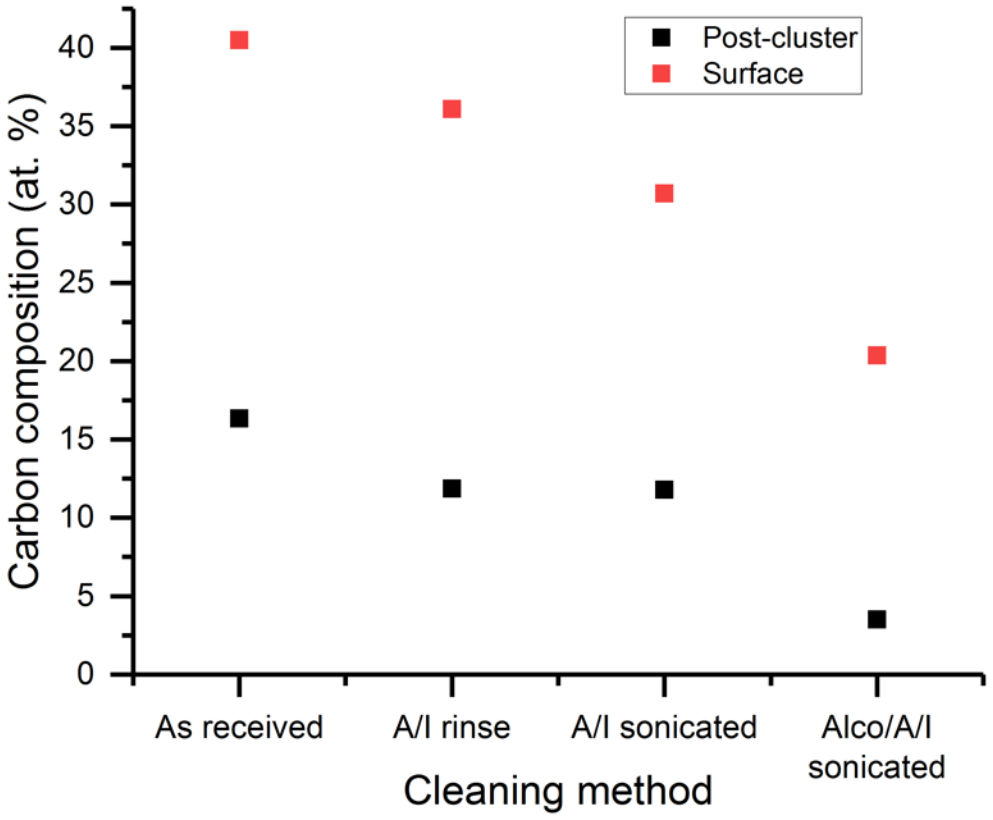

Figure 3.3.16: Comparison of carbon composition measured at the surface and after cluster sputtering for 2290 seconds for $SnO_2(F)$ subjected to 4 different cleaning procedures.

3.3.4.4 Error estimates for VBM and Fermi level measurements

The error in the VBE, cut-off, VBM, and Fermi level measurements was ascertained through a sensitivity analysis of each set of fits. By intentionally fitting an excessively broad or narrow range of data points in the linear, sloped portion (marked in blue in Figure 3.3.13 and Figure 3.3.14) of the data, an upper and lower bound on the value can be can be established. The reported value is the average of these two fits and an intermediate "best" fit. The measurement

error is defined as half of this range. When one of these values was unreasonable or unphysical, the average of the remaining two values was taken. The VBE, cut-off, and Fermi-to-VBE energy errors were estimated as described. The VBM error was estimated by propagating the error of the VBE and cut-off through the calculation. The error estimate method for the elemental composition of samples is described in section 3.3.2.

3.4 Results and discussion

Thin films of APCVD (Sn,Ge)O_2 were evaluated as photovoltaic electron transport layers. After optimizing the deposition procedure, the band structure and electrical properties were studied for 5 films representing a range of germanium concentrations. For each, thickness was determined by FIB cross-section, composition by XRF, electrical properties by Hall measurement, crystal structure by XRD, and band structure through XPS and UV-Vis spectroscopy.

3.4.1 Deposition of (Sn,Ge)O_2

Films of (Sn,Ge)O_2 were deposited by atmospheric pressure CVD, with germanium concentrations of up to 8 at. % . Deposition patterns generally resembled those of SnO_2 and SnO_2(F), described in Chapter 1, with interference fringes indicating decreasing thickness away from the center of deposition. As the tetramethylgermanium:tetramethyltin (TMG:TMT) molar ratio is increased, a transition between two distinct film growth regimes occurs. At lower TMG:TMT (ca. 0.12), films exhibit a growth rate comparable to that of SnO_2(F) in Chapter 1 (ca. 10 nm/min) and limited incorporation of Ge in the film composition (< 1 at. % Ge). At higher TMG:TMT (ca. 0.24), films show much lower growth rates (< 0.4 nm/min) and film compositions are enriched in Ge (6-8 at. % Ge). The transition between these growth regimes is

not dictated solely by the TMG:TMT ratio, but is also sensitive to the temperature and absolute concentrations. For example, a deposition with a TMG:TMT of ca. 0.13, but having double the amount of TMT, showed ca. 2-6 at. % Ge and a growth rate of ca. 1-10 nm/min. As a result of the sensitivity of the growth to these conditions, films often contained regions of disparate compositions. Commonly, a central region of lower germanium concentration is surrounded by a (relatively) radially symmetric transition to higher germanium concentrations at the edges of a 3″ × 3″ or 4″ × 4″ sample, as if a transition between these growth regimes happens within the reactor during growth.

TMG appears to act as a growth suppressant, resulting in quite low growth rates as the delivery ratio of TMG:TMT increases. The reaction of tetramethyltin with oxygen to form SnO_2 depends on intermediate gas phase reactions enumerated by Borman and Gordon.[34] When the Sn-C bonds of TMT are cleaved, a branching chain of free radical reactions is initiated, subsequently attacking oxygen. When bromotrifluoromethane is added to the reaction, the radical cleavage of this molecule generates additional free radicals, accelerating the overall reaction.[34] In contrast, bromine, t-butyl bromide, t-butyl fluoride, and the C2-C4 alkenes have a demonstrated retarding effect on film deposition.[34] If tetramethylgermanium acts as a free radical scavenger, much like these other retardants, the intermediate gas phase reactions that control the kinetics of deposition may be suppressed. At temperatures near the "turn-off temperature" for this thermally initiated deposition (the lowest reported substrate temperature for SnO_2 growth from TMT is 350 °C),[34] where the reactions are sluggish, this effect may cause growth to cease entirely. This view is supported by 1) the observation of growth rate reduction with increasing TMG delivery, and 2) the disappearance of extremely sharp changes in growth rate when the nominal deposition temperature is increased from 475 to 520 °C. Based on

temperature calibrations detailed in Chapter 1, a nominal deposition temperature of 475 °C corresponds to a substrate temperature ca. 387 °C. A higher deposition temperature improved the thickness uniformity somewhat, but substantial gradients in the thickness and composition were still observed (e.g., ca. 1 at. % to 6 at. % Ge on a single 4″ × 4″ sample).

By selecting 1 cm^2 regions of reasonable compositional and thickness uniformity from different depositions, it was possible to assemble a set of 5 suitable samples spanning the observed range germanium concentrations. While potentially extensive modification[x] would be required for coating large samples uniformly, the selected samples can serve, to some extent, as a proxy for evaluation of (Sn,Ge)O_2 as an electron transport layer without further optimization of the deposition procedure. By using the same samples for each type of characterization, the challenge of finding a number of comparable samples (and verifying that they are comparable) was eliminated. Table 3.4.1 displays the following, for each sample: thickness (by FIB, unless otherwise noted), composition (by XRF or RBS, as available), and key deposition parameters. All samples were deposited under a flow of 780 µmol/min oxygen with added nitrogen to reach a

Table 3.4.1: Composition, thickness, and deposition parameters of the 5-sample set representing a range of germanium concentrations.

Ge (at. %)	Sn (at. %)	O (at. %)	C on surface (at. %)	Thickness (nm)	Subst. Temp. (°C)	TMG Delivery Rate (µmol/min)	TMT Delivery Rate (µmol/min)
0	33	67	4.6	130 ± 15	520 ± 2	0	4.1
0.3	33	67	3.6	340 ± 30	520 ± 3	0.5	4.1
2.2	31	67	3.3	160 ± 20	520 ± 2	1.1	8
5.5	28	67	1.3	14 ± 14	520 ± 2	1.1	8
7.1	26	67	7.8	31 ± 5	521 ± 1	1.1	4.5

[x] This point is addressed in the conclusions section.

total flow rate of ca. 100 sccm.

To investigate the compositional uniformity through the thickness of each film, XPS composition studies were conducted in regions just outside of the 1 cm^2 sample area, which have similar compositions. By sputtering fully through these film regions, composition vs. thickness data closely approximating the sample area is produced without damaging the selected area. These studies suggested possible germanium enrichment at the film-substrate interface for the 0.3 and 2.2 at. % Ge samples, while the 7.1 at. % Ge sample appeared uniform. Interestingly, the best-fitting RBS models for the 0.3 and 2.2 at. % Ge sample were also bi-layer. The former was modeled as a ca. 20-30 nm layer of 2.7 at. % Ge with a 0.3 at. % Ge overlayer. The latter was modeled as a ca. 50 nm layer of 4 at. % Ge with a 1 at. % Ge overlayer (ca. 100 nm). The 5.5 at. % Ge sample was destroyed before a sputter-through experiment was possible. A sample of similar composition (by XRF) to the 5.5 at. % Ge sample was therefore used as a substitute. RBS modeling indicated a ca. 10 nm layer of 7 at. % Ge with a 5 at. % Ge overlayer. These RBS models do not provide conclusive evidence of bi-layer films, but suggest the possibility. The existence of a thin layer at the film-substrate interface is not expected to impact the band structure studies, as XPS is highly surface sensitive, and the modeled layers are too thin to substantially impact optical absorption. A surface layer, however, could impact the measured valence band position and Fermi level. The impact of a bi-layer film on Hall measurements is harder to quantify. The geometry of the Hall measurement eliminates contact resistance, but if the thin underlayer is much less resistive than the primary later, it may reduce the measured resistance. Because the existence of bi-layered depositions cannot be confirmed with certainty, average compositions and errors are listed as described in the preceding paragraphs. In all discussions, films are assumed to be one uniform layer.

Films showed evidence of structural and morphological changes with increasing germanium incorporation. The morphology of films remains similar from zero to 2.2 at. % Ge, characterized by large relatively closely-packed grains. Higher germanium concentration samples have much smaller grains. Figure 3.4.1 illustrates this trend via plan-view SEM micrographs of a subset of the samples.

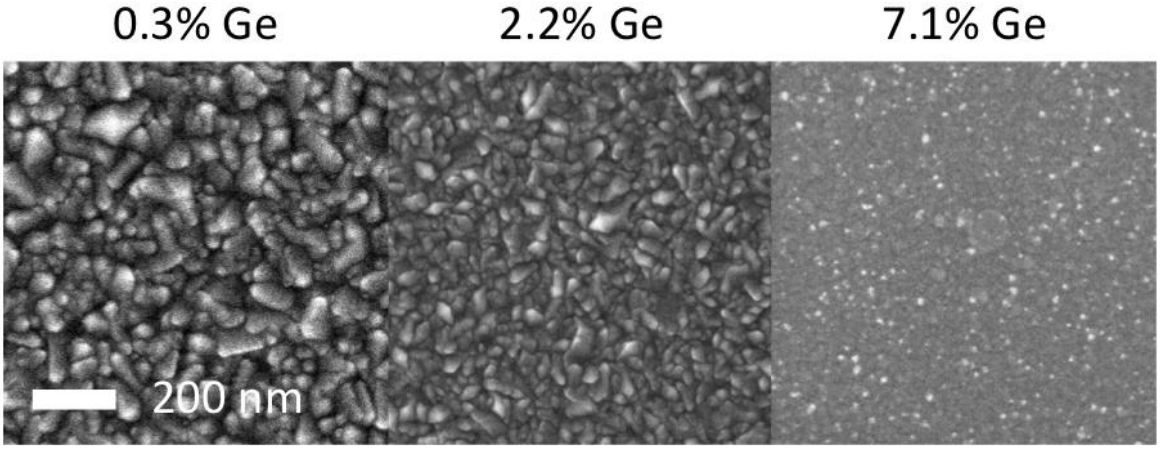

Figure 3.4.1: SEM micrographs of a subset of the 5-sample set: 0.3, 2.2, and 7.1 at. % Ge.

Powder XRD patterns identified a textured crystalline rutile SnO_2 phase (PDF 00-041-1445) in the films of neat SnO_2, as well as the 0.3 and 2.2 at. % Ge samples, with no visible diffraction peaks for the 5.5 and 7.1 at. % Ge samples. The transition from large to small grains is matched by the disappearance of the (110), (101), and (220) rutile SnO_2 peaks. These scans for the sample set are plotted in Figure 3.4.2.

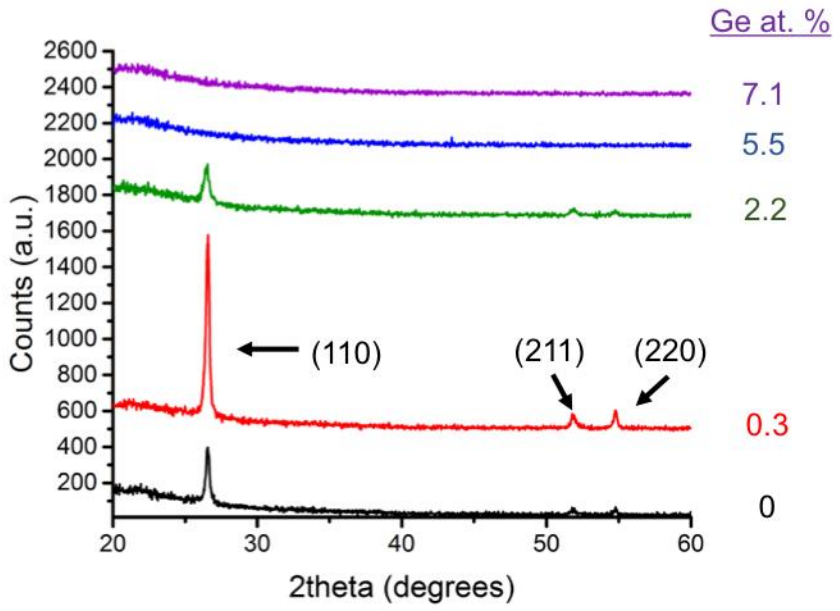

Figure 3.4.2: Powder XRD patterns for $(Sn,Ge)O_2$ for the 5-sample set. Labeled peaks correspond to rutile SnO_2.

No peaks associated with other SnO_2 or GeO_2 phases were observed. The 0.3 at. % Ge sample likely has the highest peak intensities because it is much thicker than the other films. Conversely, the 5.5 and 7.1 at. % films are very thin, and unlikely to produce significant signal intensity even if crystalline. Crystallite size estimated from the Debye-Scherrer equation trends from 26 ± 5 nm, to 30 ± 6 nm, to 16 ± 5 nm for neat SnO_2 and $(Sn,Ge)O_2$ with 0.3 and 2.2 at. % Ge, respectively. These values are smaller than the apparent grains observed by electron microscopy, indicating the presence of defects that reduce the effective crystallographic grain size, as is commonly observed. The two most Ge-rich samples showed no peaks above the detection limit of the instrument and cannot be conclusively labelled crystalline or amorphous; the films are quite thin (ca. one tenth the thickness of the 0.3 at. % Ge film) and likely also have smaller grains than the other films. These two effects reduce the peak intensity and broaden the peaks, respectively.

3.4.2 Electrical properties

Hall measurements were conducted on the 5-sample set to study the impact of germanium incorporation on the electrical properties of $(Sn,Ge)O_2$. Resistivity values for different $(Sn,Ge)O_2$ concentrations are plotted in Figure 3.4.3. Once germanium is incorporated into the film, the resistivity decreases with increasing germanium incorporation. The first addition of germanium to the film, however, does induce a small increase in the resistivity. As discussed below, these changes can all be attributed to changes in the carrier concentration.

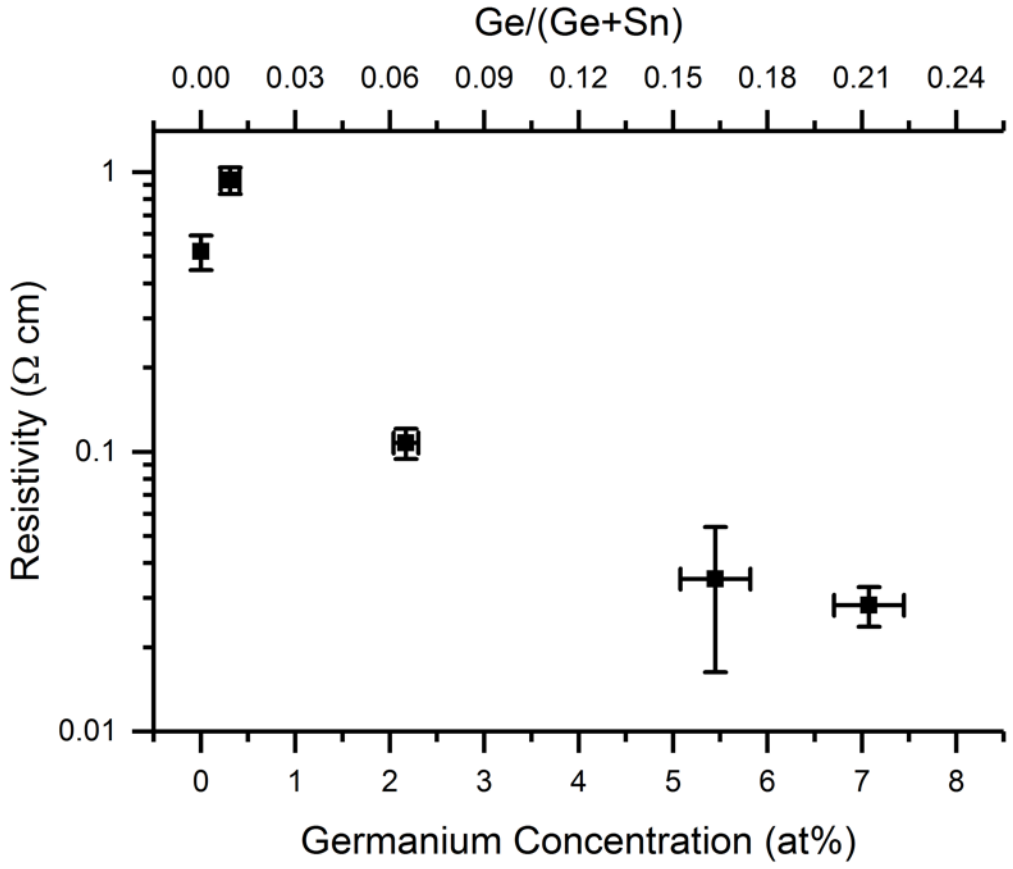

Figure 3.4.3: Resistivity vs. germanium concentration for samples deposited at 520 °C. Deposition conditions are given in Table 3.4.1.

Equation 3.4.1 indicates the relationship between resistivity, carrier concentration, and mobility,

$$\rho = \frac{1}{ne\mu_e} \qquad [3.4.1]$$

where ρ is the resistivity, n is the carrier concentration, e is the charge of an electron, and μ_e is the electron mobility. The observed reduction in resistivity is due to an increase in the carrier concentration as the mobility remains stable within measurement error. These two trends are shown in Figure 3.4.4. The mobility is low for degenerately doped SnO_2,[22] but consistent with

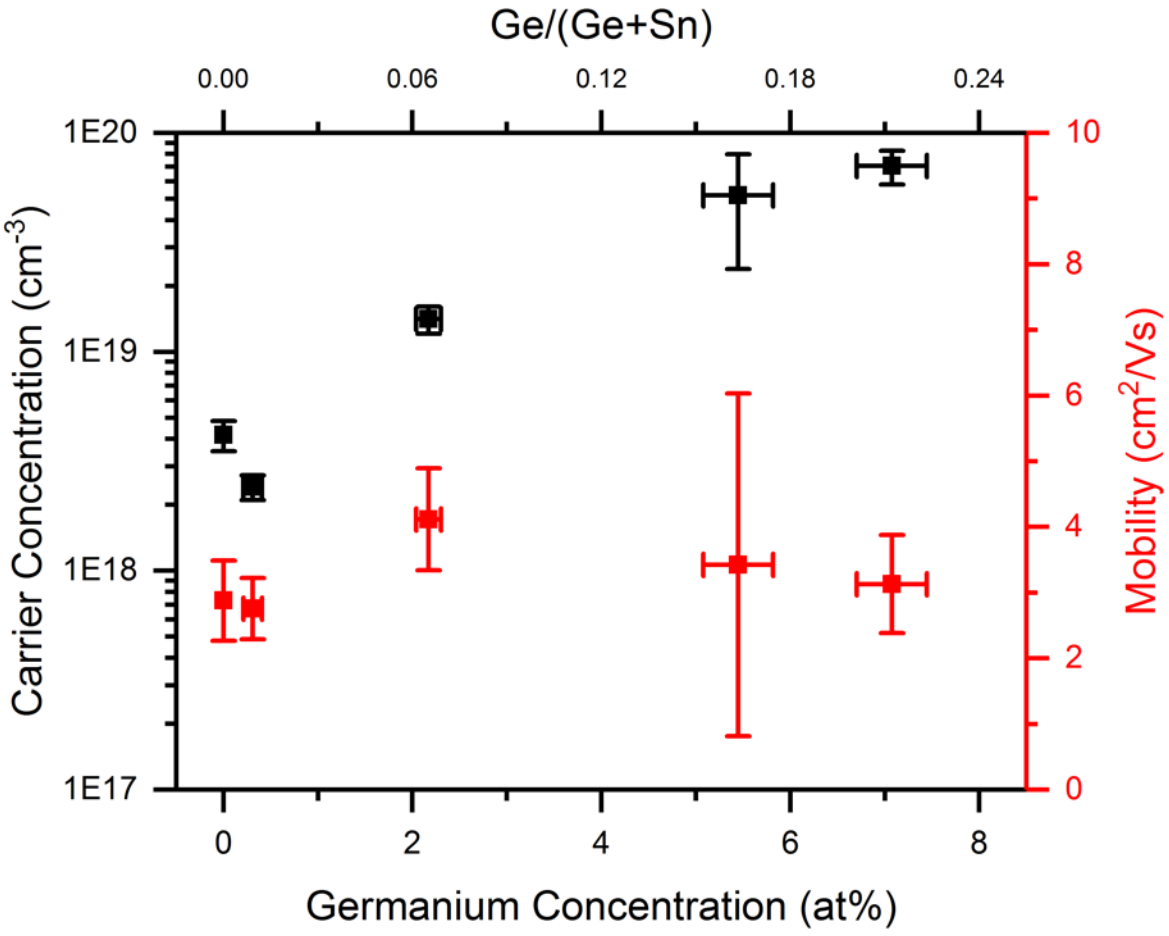

Figure 3.4.4: Carrier concentration and mobility values for (Sn,Ge)O_2 with various germanium concentrations.

literature values for SnO_2 films with crystallite sizes $\leq$ 50 nm.[35] The mobility could be limited by the small grain size of these materials, or by electron scattering in the conduction band due to the introduction of germanium.[10] This behavior is consistent with the creation of oxygen

vacancies, perhaps owing to tetramethylgermanium interfering with the completion of the tetramethyltin reactions.[xi] This view is consistent with the observed growth suppression trend. It should be noted that such high carrier concentrations might be problematic for certain absorbers—an excess of carriers can drive recombination at the absorber-ETL interface. Modeling and device testing is necessary to determine whether this material falls within an acceptable carrier concentration range for a given absorber.

3.4.3 Band structure

Changes in the band structure of $(Sn,Ge)O_2$ with increasing germanium incorporation were studied. The optical gap was measured by UV-Vis spectroscopy, the valence band maximum and Fermi level were determined by XPS, and the conduction band minimum was estimated by combining these results. Together, the valence band maximum and optical gap determine the conduction band minimum, and thus, the degree of conduction band tuning allowed by germanium incorporation. The change in the position of the Fermi level within the band gap gives a sense of the degree of doping. As described in the methods section, the optical gap of each sample was determined by applying a chosen transition state model to a plot of the measured absorption coefficient vs. photon energy. First the results of direct-crystalline and direct-amorphous[xii] modeling are presented. Next, these results are interpreted together with data on the film crystallinity, valence band maxima, carrier concentrations, and Fermi levels.

[xi] A carrier concentration increase of ca. 1×10^{19} cm^{-3} corresponds to a 0.1 % change, assuming 10^{22} atoms/cm^3. This quantity is too small to affect XPS oxygen composition.

[xii] While this fit applies to amorphous-direct or crystalline-indirect films, a transition from direct to indirect is thought to be less likely than crystalline to amorphous. For simplicity's sake, the relevant models and calculated optical gaps will be referred to as amorphous-direct only.

Figure 3.4.5 displays plots of crystalline-direct (r = 2) and amorphous-direct (r = 0.5) transition models for the 5-sample set. The fitting regions determined by the methods described in Section 4.3.4.1 are circled in red. Figure 3.4.6 shows the calculated optical gaps resulting from the two models. The values from the two models differ by as much as an electron volt, and affect

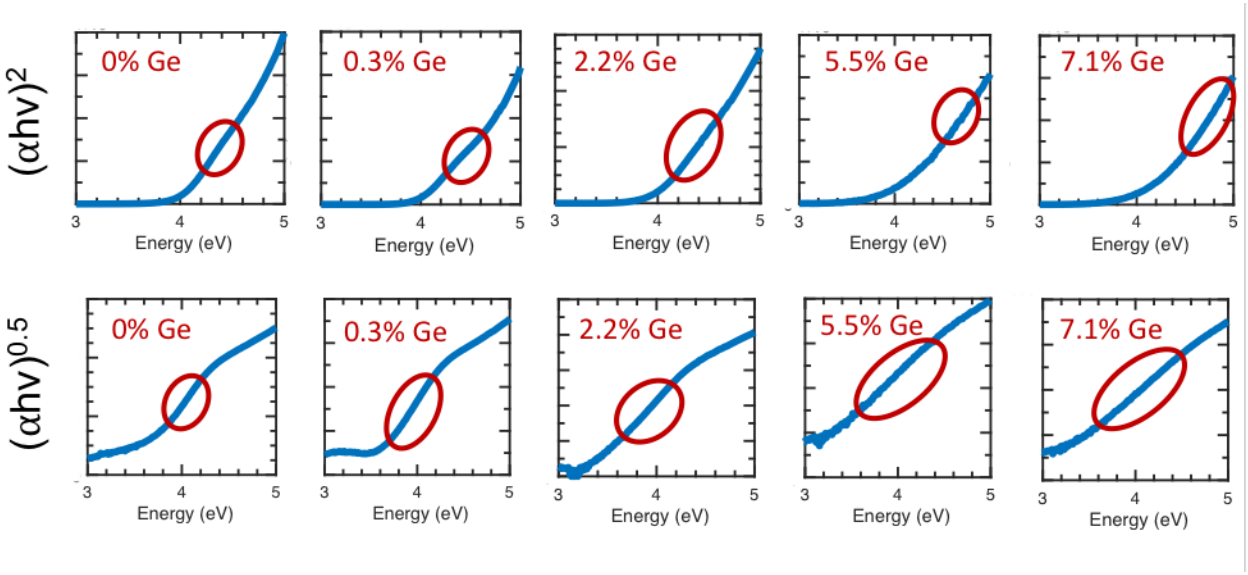

Figure 3.4.5: A comparison of direct-crystalline (top row) vs. direct-amorphous models (bottom row) applied to absorption coefficient data from samples with differing amounts of germanium.

the band structure in dramatically different ways. The plots displayed in Figure 3.4.5 are most consistent with increasing germanium incorporation causing disruption to the long-range order of the crystalline phase. XRD results, for example, are consistent with shrinking grain size with increasing germanium content. As germanium incorporation increases, the increasing curvature in the crystalline-direct model of the data near 4 eV is consistent with the appearance of an Urbach tail.[16] This tailing effect is associated with disordered or amorphous materials, and particularly with the associated localized states in the band tails. The amorphous-direct model (and the crystalline-direct model) used here assumes parabolic bands—it is expected to be less

accurate in the presence of significant band tailing and sub-conduction band defect states.[36][xiii]

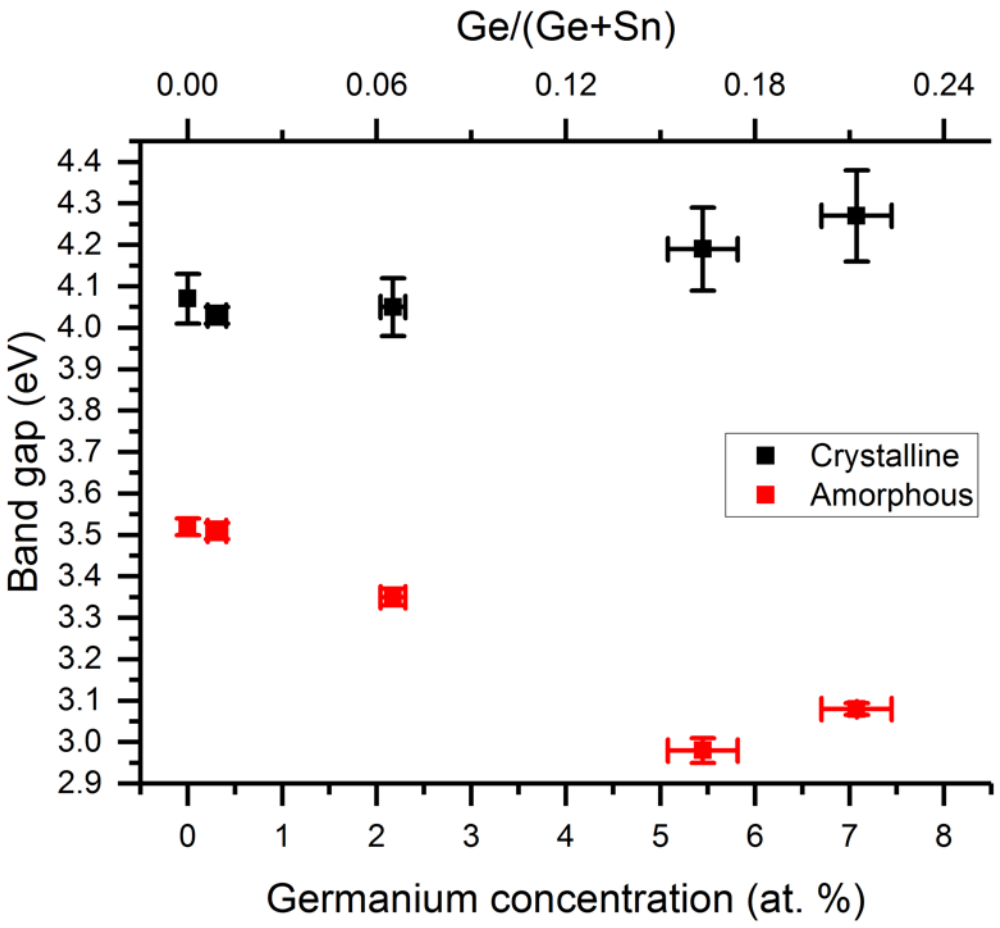

Figure 3.4.6: Calculated optical gaps for the 5-sample set described in Table 3.4.1. Composition error bars are representative of the spatial uniformity of each sample, and optical gap errors are determined by error propagation. These procedures are described in the materials and methods section.

The challenges of modeling the optical gap of these (Sn,Ge)O_2 films are likely due to a somewhat ill-defined nature of the optical gap in these materials. That neither transition model is obviously superior (i.e., more consistently linear) for a given sample is a reflection of this fact.

[xiii] The modeling of band tails and localized states is controversial. Ibrahim, et al. summarizes the different approaches succinctly. Essentially, there are no agreed-upon methods for amorphous semiconductors, and the variability in band tails, defects, and band shapes may preclude a single model that applies to all, or even a large subset, of materials.

The optical gap calculations of the considered samples should be interpreted circumspectly. Although neat SnO_2 is crystalline, even in this case a reasonable amorphous-direct transition can be extracted from the data. Similar features have been observed in literature for SnO_2 and SnO_2(F).[37] As germanium is alloyed into the material, the extent to which an amorphous model can be faithfully applied increases; however, even at the highest germanium concentrations obtained, a reasonable crystalline-direct transition can be extracted from the data. Taken together, the XRD and optical data suggest crystalline materials with extensive tailing into the bandgap, with greater tailing at higher germanium concentrations.

The crystalline-direct model applied here yields an optical gap consistent with degenerately doped SnO_2.[8, 15, 16] As will be discussed further below, the carrier concentrations measured using the Hall effect are also consistent with degenerate doping. The crystalline-direct optical gaps shown in Figure 3.4.6 increase slightly at higher germanium concentrations, and are in between literature values for neat SnO_2 and rutile (4.68 eV) or glassy GeO_2 (5.6 eV).[17, 18, 38][xiv] Although it is reasonable to expect that the band gap of the mixed alloy would lie between those of the binary oxides, another explanation is more likely. As discussed below, the changes in the bandgap track the changes in the measured carrier concentration, suggesting the changes in the bandgap result primarily from the Moss-Burstein effect.

The amorphous optical gaps of the considered samples decrease with increasing germanium incorporation: 3.5 to 3.1 eV for neat SnO_2 through 7.1 at. % Ge. Melsheimer, et al. report similar changes (specifically, a decrease from 3.72 to 3.07 eV) in the amorphous optical gap of SnO_2 with a transition from crystalline to amorphous films.[16] Other authors using an

[xiv] Hexagonal GeO_2 (5.54 eV) is also stable at room temperature.

absorption model with r = 0.5 report optical gaps in agreement with the range observed in this dissertation.[8, 15] Note that amorphous-direct fits are not necessarily performed or reported for SnO_2, likely because materials are assumed to have similar band structure to pure, single crystals of SnO_2, which have neither allowed indirect transitions nor any amorphous material.[39]

A note regarding the Moss-Burstein effect: degenerate doping of an n-type material can have the effect of increasing the optical gap by filling states in the conduction band, raising the energy required for an electronic transition from a filled valence band state to a vacant conduction band state. This effect is counter-balanced to some extent by the lowering of the conduction band and raising of the valence band due to carrier-carrier and carrier-impurity interactions. For degenerately doped SnO_2 (6×10^{19} cm^{-3}), Sanon, et al., predicted a Moss-Burstein-induced optical gap widening of ca. 0.6 eV and a narrowing effect of ca. 0.3 eV.[37]

Operating on the assumption that an increasing carrier concentration drives the increase in the crystalline-direct optical gap, one can use the carrier concentration to predict the expected energy difference between the conduction band minimum and Fermi level. The following equations were used,

$$N_C = 2\left[\frac{2\pi m_e^* kT}{h^2}\right]^{1.5} \quad [3.4.2]$$

$$E_C - E_F = -kT\left[\ln\left(\frac{n_0}{N_C}\right) + \frac{1}{8}\frac{n_0}{N_C} - \left(\frac{3}{16} - \frac{\sqrt{3}}{9}\right)\left(\frac{n_0}{N_C}\right)^2\right] \quad [3.4.3]$$

where N_c is the effective density of states in the conduction band, m_e^* is the electron effective mass (0.3 times the mass of an electron)[xv][1], k is the Boltzmann constant, T is the temperature in Kelvin, h is Planck's constant, and n_0 is the electron carrier concentration. Equation 3.4.3 is

[xv] The error in the energy difference is determined by calculating the energy difference using an effective mass of 0.2 and 0.6, and using half the range as the error.

valid for degenerately doped semiconductors, where the Fermi level is less than 3 kT away from the conduction band minimum.[40] Since the top of the optical gap is coincident with the Fermi level in degenerately doped materials (whereas the fundamental band gap is unaffected by degenerate doping), a negative value for Equation 3.4.3 indicates that the fundamental band gap is smaller than the optical gap, and the "fundamental" conduction band position is in fact below the Fermi level. Using Equations 3.4.2 and 3.4.3, fundamental band gap predictions were made for all considered samples. These values are compared with the measured crystalline-direct optical gap in Figure 3.4.7. The fundamental band gap is essentially flat, consistent with a stable fundamental gap and an optical gap that increases with increasing carrier concentration.

Given the relatively constant optical and fundamental gaps, the valence band position determines the degree of conduction band tuning possible in this material. As shown in Figure 3.4.8, the valence band maximum of the neat SnO_2 sample is higher than that of the $(Sn,Ge)O_2$ samples, ranging from half an eV for the 0.3 at. % Ge sample, to ca. 0.3 eV for the 7.1 at. % Ge sample. The upward trend in the valence band position between 0.3 and 7.1 at. % Ge indicates that the incorporation of germanium has increased the energy of the highest occupied electron energy levels. In degenerately-doped SnO_2, electron-electron and electron-impurity interactions are thought to raise the energy of the valence band.[22][xvi] The upward shift in energy may also be due to the addition of states above the valence band as the long-range order of the material is disrupted.

[xvi] This same effect lowers the conduction band energy—there is some compensation between these effects, which narrow the bandgap, and the Moss-Burstein effect, which raises the conduction band position.

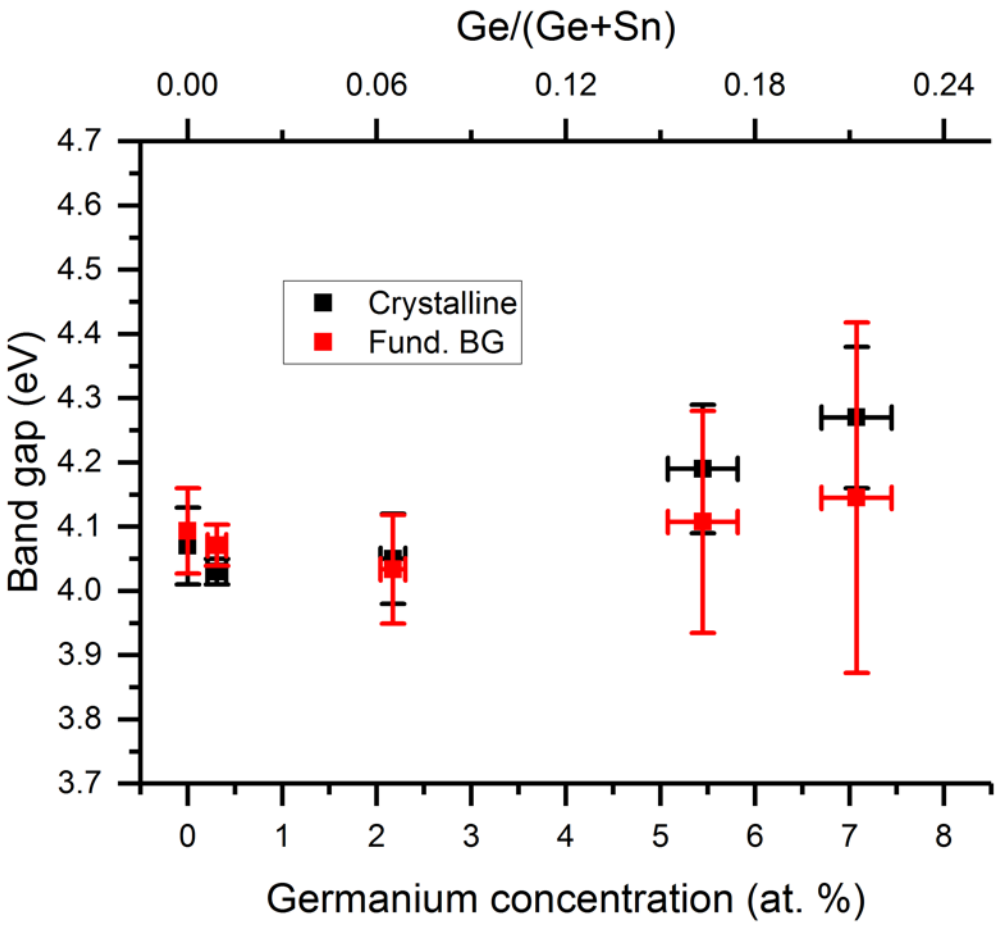

Figure 3.4.7: A comparison of the measured crystalline-direct optical gap and the calculated fundamental band gap. Composition error bars are representative of the spatial uniformity of each sample, and optical gap errors are determined by error propagation. These procedures are described in the materials and methods section.

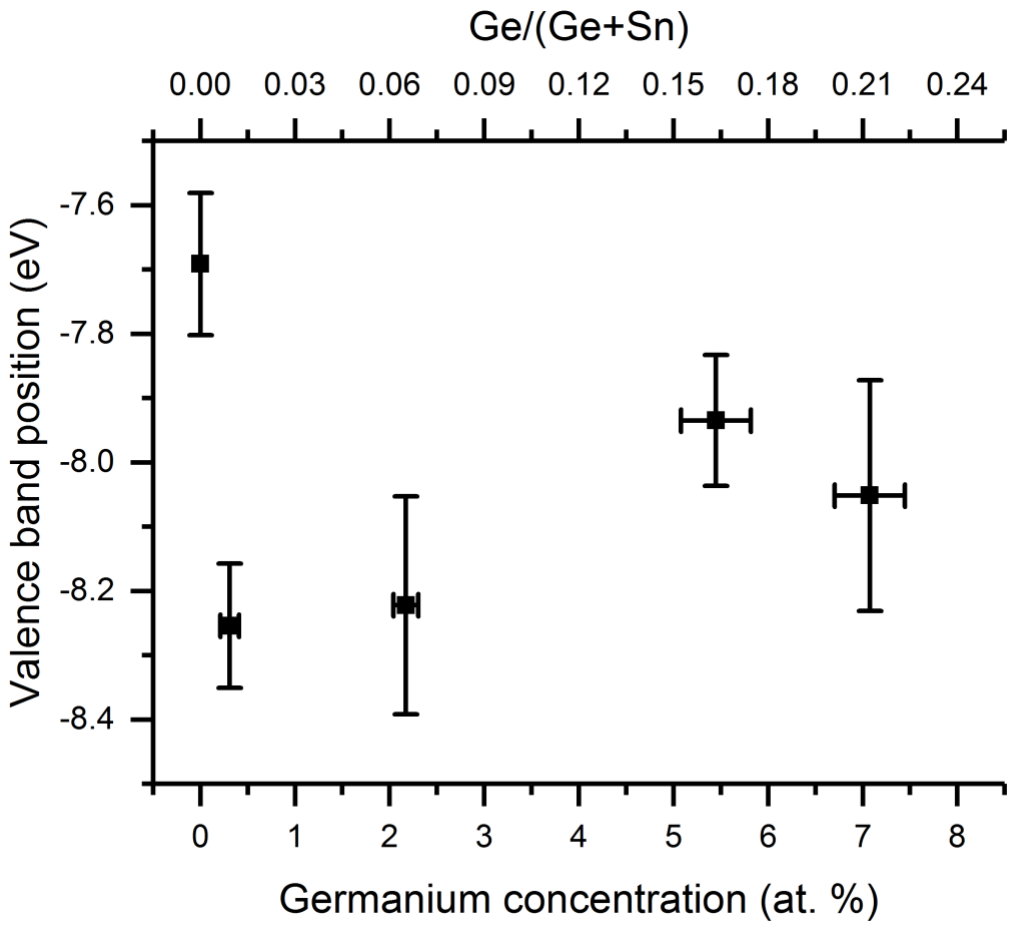

Figure 3.4.8: Valence band maxima vs. germanium concentration, measured for the 5-sample set. Composition error bars are representative of the spatial uniformity of each sample, and valence band position errors are determined by error propagation of the linear fits for the secondary electron cut-off and valence band edge. These procedures are described in the materials and methods section.

Figure 3.4.9 displays the valence band maxima, and conduction band minima based on the crystalline-direct or amorphous-direct model. The crystalline-direct fit reflects primarily the increase in valence band maximum with germanium incorporation from 0.3 at. % to 7.1 at. % Ge. Neat SnO_2 and 7.1 at. % Ge have essentially the same conduction band position, and the greatest difference in energy lies between neat SnO_2 and the 0.3 at. % Ge sample: 0.6 eV. This range may permit modest conduction band position tuning: the structural disruption due to germanium incorporation is smallest in this concentration range, at least as assessed by the

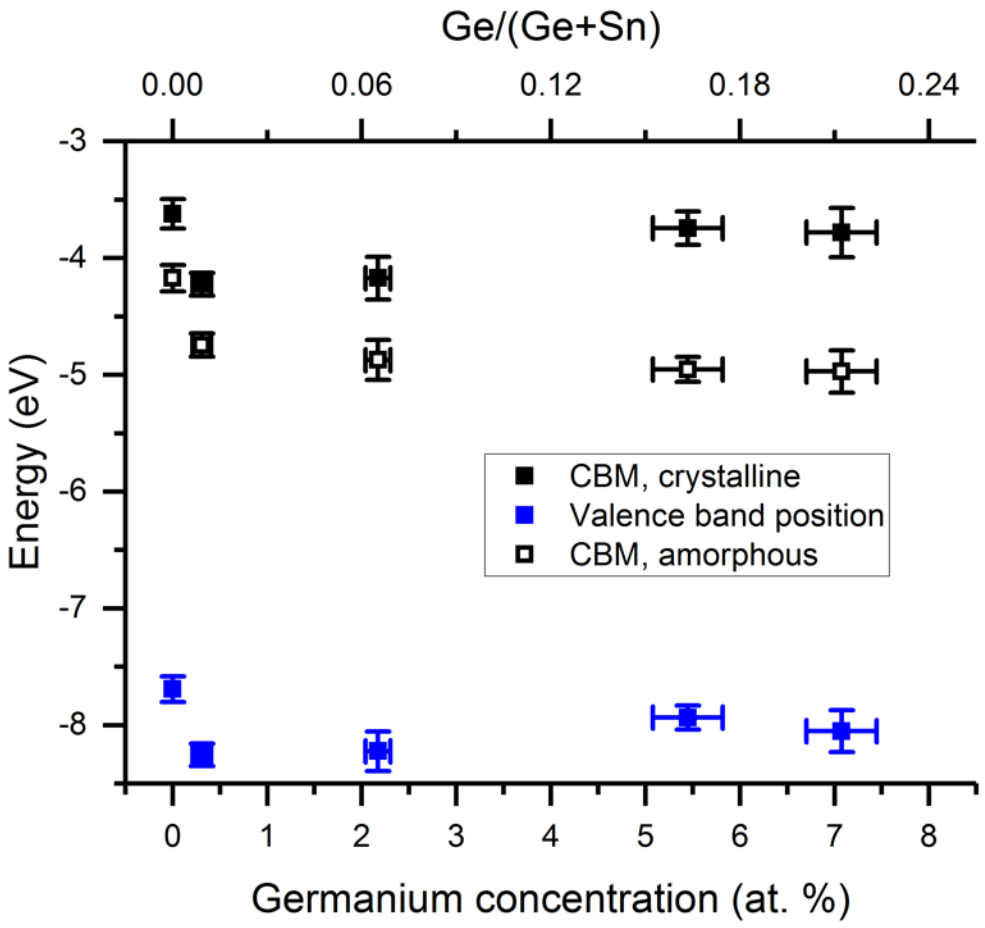

Figure 3.4.9: Valence band maxima, and conduction band minima based on a crystalline-direct, or amorphous-direct fit, measured for the 5-sample set. Composition error bars are representative of the spatial uniformity of each sample, and valence band position errors are determined by error propagation of the linear fits for the secondary electron cut-off and valence band edge. These procedures are described in the materials and methods section.

degree of Urbach tailing. The amorphous-direct fit shows a change of nearly one electron volt from neat SnO2 to 5.5 at. % Ge, as localized states penetrate further into the gap at higher germanium concentrations. It should be noted that some properties of SnO2 vary with thickness, [22]which could impact these interpretations.

The increased doping indicated by the carrier concentration trend suggests that the material ought to be more degenerately doped as germanium incorporation increases. As shown in Figure 3.4.10, the Fermi level measured by XPS appears essentially constant with increasing

germanium content, and is roughly half an electron volt higher for neat SnO_2. Figure 3.4.11

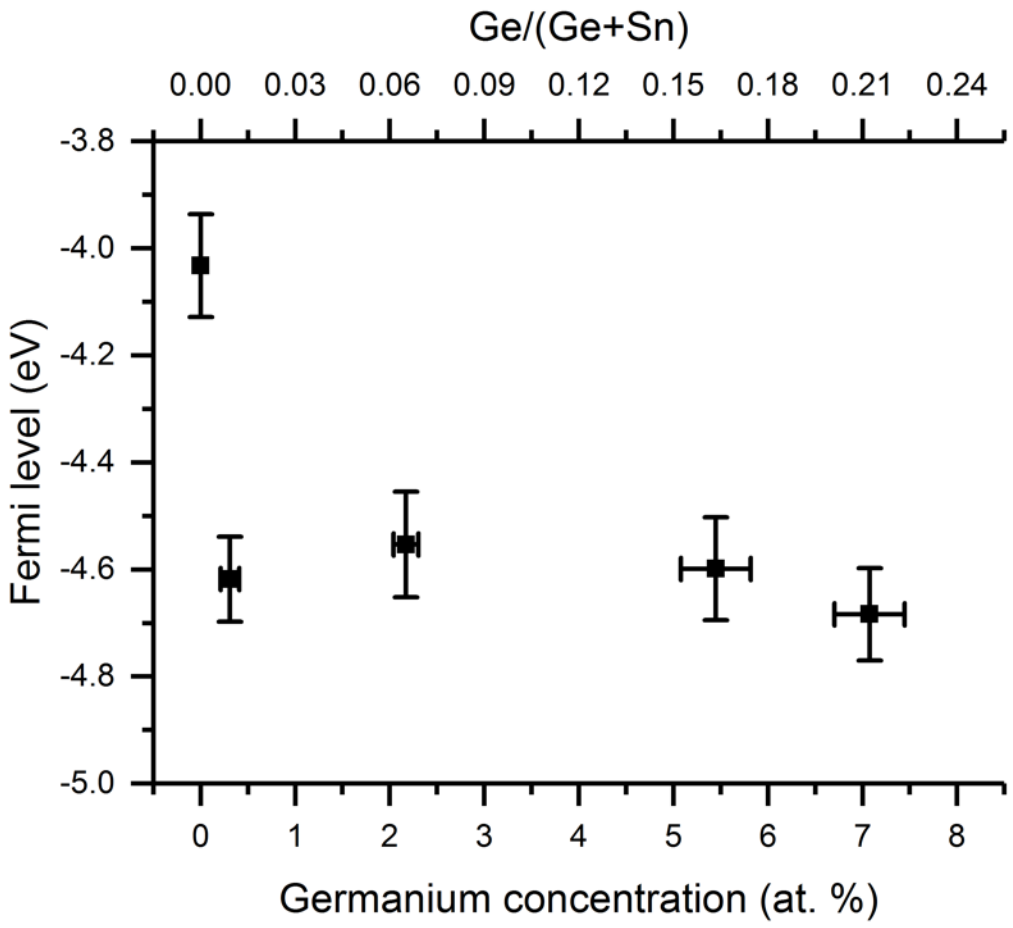

Figure 3.4.10: Fermi levels measured for the 5-sample set, as measured by XPS. Composition error bars are representative of the spatial uniformity of each sample, and Fermi level errors are determined by error propagation of the linear fits for the secondary electron cut-off. These procedures are described in the materials and methods section.

displays the XPS-measured Fermi levels, as well as the conduction band minima calculated using either the crystalline-direct optical gap, or the amorphous-direct optical gap. As Figure 3.4.11 shows, the XPS-measured Fermi levels do not reflect degenerate doping, in contrast with the Hall data and the discussion above related to a Moss-Burstein effect. The energy difference between the XPS-measured Fermi level and the crystalline-direct conduction band minimum is ca. 0.4 eV for neat SnO2, and increases to ca. 1 eV for the highest two germanium concentrations. Given that XPS is a surface-sensitive technique, the valence band and Fermi

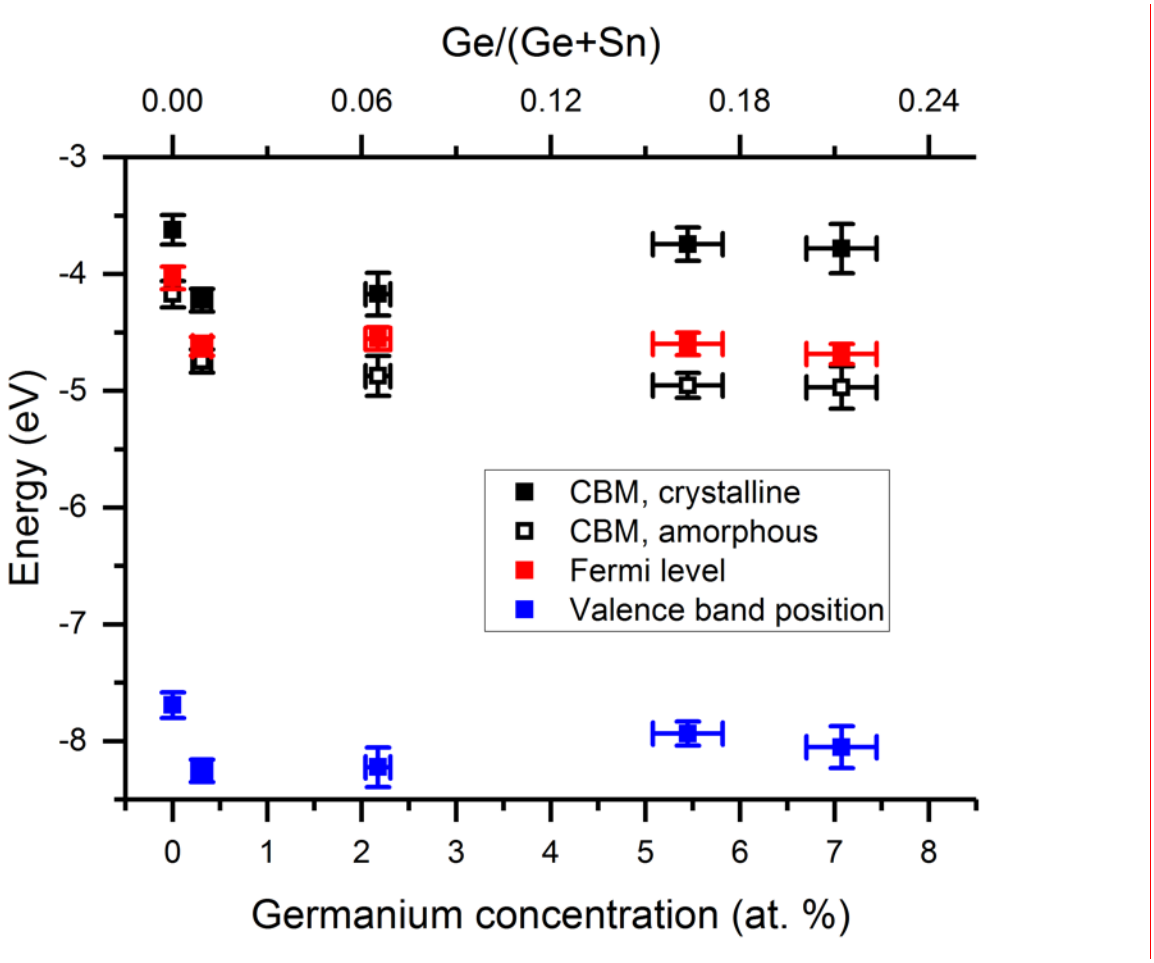

Figure 3.4.11: The band structure of (Sn,Ge)O_2, including the conduction band position (black), surface (XPS) Fermi level (red), and valence band position (blue). The conduction band position is calculated using a crystalline-direct (black filled squares) or amorphous-direct (black open squares) optical gap fit. Composition error bars are representative of the spatial uniformity of each sample, and conduction band position and Fermi level errors are determined by error propagation of the linear fits for the secondary electron cut-off, valence band edge, and the band gap, where relevant. Valence band position errors are determined by error propagation of the linear fits for the secondary electron cut-off and valence band edge. These procedures are described in the materials and methods section.

level measurements are expected to be those of the surface of the considered films. If significant surface band bending is present, due, for example, to defects or surface dipoles, then the Fermi level measured at the surface may not accurately report on the value deeper in the film. For neat tin oxide, Weidner observed band bending of 0.3 eV or less, due to surface structure on clean SnO_2. However, for tantalum- or antimony-doped tin oxide, the Fermi level is pinned at the

surface—perhaps owing to surface segregation of some of the dopant—to a level a few tenths of an eV below the conduction band minimum. For these degenerately doped samples, the Fermi level pinning leads to band bending of 0.8 to 1.1 eV.[1] The conduction band minimum calculated with the amorphous-direct optical gap is similar to the measured Fermi level, suggesting that the surface Fermi level may be pinned to states in the band tail at or near these energies.

Assembling observations regarding the predicted fundamental conduction band position, the surface and bulk Fermi levels, and the valence band maximum, one arrives at Figure 3.4.12. The fundamental conduction band minimum, derived from a crystalline-direct transition, shows modest tuning, primarily owing to changes in the valence band. The Fermi level in the bulk material rises above the fundamental conduction band minimum as germanium concentration increases, consistent with the degenerate doping indicated by the rising carrier concentration. Band bending at the surface pushes the XPS-measured Fermi level down to roughly the same position as germanium incorporation increases, suggesting that the cause of bending may be the same across the germanium-containing films.

As an electron transport layer, $(Sn,Ge)O_2$ shows modest conduction band tuning at low germanium concentrations. However, the likely existence of defects in the gap, which can act as traps and recombination centers, and the high carrier concentration, which can drive recombination, present substantial limitations for this application. As it stands, only $(Sn,Ge)O_2$ films with the lowest concentrations of germanium are potential ETL candidates. Further experimental and computational investigation, e.g., to determine acceptable defect and carrier concentration levels, could recommend or reject the use of these films with a particular absorber

As an electron transport layer, $(Sn,Ge)O_2$ shows modest conduction band tuning at low

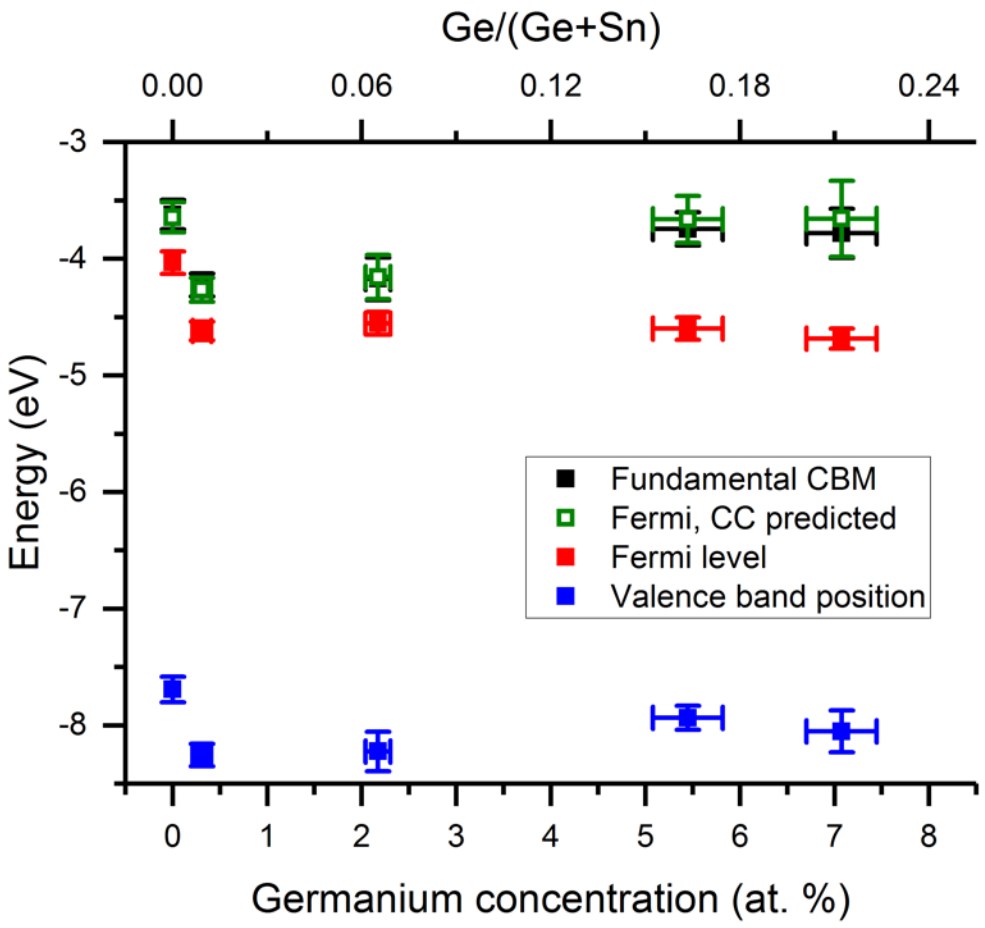

Figure 3.4.12: The band structure of (Sn,Ge)O_2, including the fundamental conduction band position (black), XPS-measured Fermi level (red), the carrier concentration-predicted Fermi level (green), and valence band position (blue). The conduction band position is calculated using an crystalline-direct optical gap fit. Composition error bars are representative of the spatial uniformity of each sample, and conduction band position and Fermi level errors are determined by error propagation of the linear fits for the secondary electron cut-off, valence band edge, and the band gap, where relevant. The error of the Fermi level predicted from the carrier concentration is half the range of predicted Fermi levels for a range of effective masses. Valence band position errors are determined by error propagation of the linear fits for the secondary electron cut-off and valence band edge. These procedures are described in the materials and methods section.

germanium concentrations. However, the likely existence of defects in the gap, which can act as traps and recombination centers, and the high carrier concentration, which can drive recombination, present substantial limitations for this application. As it stands, only (Sn,Ge)O_2 films with the lowest concentrations of germanium are potential ETL candidates. Further

experimental and computational investigation, e.g., to determine acceptable defect and carrier concentration levels, could recommend or reject the use of these films with a particular absorber material. The carrier concentration might be lowered to a workable level by a deposition process that reduces oxygen vacancy creation. One option is a more reactive germanium precursor, (e.g., germane or dimethylgermane) which might not suppress the tin oxide reaction, and hence would produce fewer oxygen vacancies. Co-sputtering tin and germanium targets can also produce $(Sn,Ge)O_2$ films at a range of concentrations.[14] No optical gap measurements were performed, so it is unclear whether the band structure is preferable with this method.

3.5 Conclusions

An APCVD method was developed for $(Sn,Ge)O_2$, using tetramethyltin, tetramethylgermanium, and oxygen at nominal deposition temperatures between 475 and 520 °C. Germanium incorporation of up to 8 at. % was achieved, representing ca. 25 % of the cations in the film. Tetramethylgermanium appeared to act as a retardant to the free radical reactions which drive SnO_2 deposition, resulting in negligible film growth for germanium incorporation over 8 at. %. A set of samples with 0, 0.3, 2.2, 5.5, and 7.1 at. % Ge were selected for band structure and electrical characterization. XRD patterns showed peaks consistent with rutile SnO_2 for neat SnO_2, as well as 0.3 and 2.2 at. % Ge films. The 5.5 and 7.1 at. % Ge samples were too thin to diffract. Resistivity decreased with increasing germanium incorporation, consistent with stable mobility and increasing carrier concentration. Based on the measured carrier concentrations, all samples are expected to be degenerately doped. The optical absorption spectrum showed patterns consistent with crystalline-direct and amorphous-direct optical transitions, suggesting a crystalline material with a fraction of less well-ordered material that grows with increasing

germanium concentration. The increase in the optical gap with germanium incorporation is thought to be due to the increasing carrier concentration, via the Moss-Burstein effect. The valence band decreases by ca. 0.5 eV from neat SnO_2 to 0.3 at. % Ge concentration, then gradually rises as more germanium is incorporated. The conduction band position essentially mirrors this pattern, showing modest tuning of ca. 0.5 eV from neat SnO_2 to 0.3 at. % Ge. The XPS-measured Fermi level was substantially lower than the value predicted for the bulk: ca. 0.4 eV for the 0-2.2 at. % Ge samples, and ca. 1 eV for the 5.5 and 7.1 at. % Ge samples. This discrepancy is thought to be caused by band bending at the surface of the material—XPS is a highly surface sensitive measurement, and probes primarily the first few nanometers of a material. Surface band bending effects have been observed on clean and doped SnO_2 surfaces. While the exact mechanism cannot be ascertained, the Fermi level is relatively stable as germanium incorporation increases—raising the possibility that the mechanism may be the same across the considered germanium-containing samples. Further study is required to ascertain whether high carrier concentration and the likely presence of near-band defects precludes the use of this method to deposit $(Sn,Ge)O_2$ electron transport layers.

References

1. Weidner, M., *Fermi level determination in tin oxide by photoelectron spectroscopy*. 2015, TU Darmstadt. p. 1-428.

2. Vaughan, A. *Time to shine: Solar power is fastest-growing source of new energy*. The Guardian [Online], Oct 4, 2017. https://www.theguardian.com/environment/2017/oct/ 04/ solar-power-renewables-international-energy-agency. (accessed April 4, 2018)

3. Shanthi, E., et al., *Electrical and optical properties of undoped and antimony-doped tin oxide films*. Journal of Applied Physics, 1980. **51**(12): p. 6243-6251.

4. Batzill, M. and U. Diebold, *The surface and materials science of tin oxide*. Progress in Surface Science, 2005. **79**(2-4): p. 47-154.

5. Mani, R., K. Vivekanandan, and K. Vallalperuman, *Synthesis of pure and cobalt (Co) doped SnO_2 nanoparticles and its structural, optical and photocatalytic properties*. Journal of Materials Science: Materials in Electronics, 2016. **28**(5): p. 4396-4402.

6. Muramba, V.W. and M. Mageto, *Electrical and structural properties of aluminium doped tin oxide codoped with sulphur for solar energy*. Energy Procedia, 2016. **93**: p. 39-45.

7. Heo, J., et al., *$(Sn,Al)O_x$ films grown by atomic layer deposition*. Journal of Physical Chemistry C, 2011. **115**(20): p. 10277-10283.

8. Reddy, S.R. and A.K. Mallik, *UV absorption studies of undoped and fluorine-doped tin oxide films*. Thin Solid Films, 1986. **143**(2): p. 113-118.

9. Maruyama, T. and K. Tabata, *Fluorine-doped tin dioxide thin films prepared by chemical vapor deposition*. Journal of Applied Physics, 1990. **68**(8): p. 4282-4285.

10. Proscia, J. and R.G. Gordon, *Properties of fluorine-doped tin oxide films produced by atmospheric pressure chemical vapor deposition from tetramethyltin, bromotrifluoromethane and oxygen*. Thin Solid Films, 1992. **214**(2): p. 175-187.

11. Rakhshani, A.E., Y. Makdisi, and H.A. Ramazaniyan, *Electronic and optical properties of fluorine-doped tin oxide films*. Journal of Applied Physics, 1998. **83**(2): p. 1049-1057.

12. Vidhya, S.N., O.N. Balasundaram, and M. Chandramohan, *Structural and optical investigations of gallium doped tin oxide thin films prepared by spray pyrolysis*. Journal of the Saudi Chemical Society, 2016. **20**(6): p. 703-710.

13. Nozaki, C., K. Tabata, and E. Suzuki, *Synthesis and characterization of homogeneous germanium-substituted tin oxide by using sol–gel method*. Journal of Solid State Chemistry, 2000. **154**(2): p. 579-583.

14. Arita, M., et al., *Effects of protium introduction on electrical and optical properties of tin-germanium oxide thin films*. Materials Transactions, 2002. **43**(11): p. 2670-2672.
15. Spence, W., *The UV absorption edge of tin oxide thin films*. Journal of Applied Physics, 1967. **38**(9): p. 3767-3770.

16. Melsheimer, J. and D. Ziegler, *Band gap energy and Urbach tail studies of amorphous, partially crystalline and polycrystalline tin dioxide*. Thin Solid Films, 1985. **129**: p. 35-47.

17. Papazian, H.A., *Energy gap and electrical conductance of hexagonal germanium dioxide*. Journal of Applied Physics, 1956. **27**(10): p. 1253-1254.

18. Stapelbroek, M. and B.D. Evans, *Exciton structure in the UV absorption edge of tetragonal GeO_2*. Solid State Communications, 1978. **25**(11): p. 959-962.

19. Heo, J., A.S. Hock, and R.G. Gordon, *Low temperature atomic layer deposition of tin oxide*. Chemistry of Materials, 2010. **22**(17): p. 4964-4973.

20. Heo, J., S.B. Kim, and R.G. Gordon, *Atomic layer deposition of tin oxide with nitric oxide as an oxidant gas*. Journal of Materials Chemistry, 2012. **22**(11): p. 4599-4602.

21. Baliga, B.J. and S. Ghandhi, *The preparation and properties of tin oxide films formed by oxidation of tetramethyltin*. Journal of the Elecrochemical Society, 1976. **123**(6): p. 941-944.

22. Sanon, G., R. Rup, and A. Mansingh, *Influence of thickness and substrate on the properties of SnO_2 films deposited by CVD*. Physica Status Solidi A, 1991. **128**(1): p. 109-116.

23. Molloy, K.C., *Precursors for the formation of tin (IV) oxide and related materials*. Journal of Chemical Research, 2008(10): p. 549-554.

24. Kita, K., et al., *Direct evidence of GeO volatilization from GeO_2/Ge and impact of its suppression on GeO_2/Ge metal–insulator–semiconductor characteristics*. Japanese Journal of Applied Physics, 2008. **47**(4S): p. 2349-2353.

25. Lorenz, H., et al., *Preparation and structural characterization of SnO2 and GeO2 methanol steam reforming thin film model catalysts by (HR) TEM*. Materials Chemistry and Physics, 2010. **122**(2-3): p. 623-629.

26. Reich, S., H. Suhr, and B. Waimer, *Plasma-enhanced chemical vapour deposition of thin GeO_2, SnO_x, GeO_2-SnO_x, and In_2O_3 films*. Thin Solid Films, 1990. **189**(2): p. 293-302.

27. York, D., *Least-squares fitting of a straight line*. Canadian Journal of Physics. **44**(5): p. 1079-1086.

28. Gunawan, O., Y. Virgus, and K.F. Tai, *A parallel dipole line system*. Applied Physics Letters, 2015. **106**(6): p. 062407.

29. Fai, T.K., *Investigating the open-circuit voltage deficit in $Cu_2ZnSn(S,Se)_4$ solar cells*. 2015, Nanyang Technological University. p. 1-165.

30. Ritter, D. and K. Weiser, *Suppression of interference-fringes in absorption-measurements on thin-films*. Optics Communications, 1986. **57**(5): p. 336-338.

31. Cesaria, M., A.P. Caricato, and M. Martino, *Realistic absorption coefficient of ultrathin films*. Journal of Optics, 2012. **14**(10): p. 105701.

32. Viezbicke, B.D., et al., *Evaluation of the Tauc method for optical absorption edge determination: ZnO thin films as a model system*. Physica Status Solidi B, 2015. **252**(8): p. 1700-1710.

33. Helander, M.G., et al., *Work function of fluorine doped tin oxide*. Journal of Vacuum Science and Technology A, 2011. **29**(1): p. 011019.

34. Borman, C.G., *Reactive pathways in the chemical vapor deposition of tin oxide films by tetramethyltin oxidation*. Journal of the Electrochemical Society, 1989. **136**(12): p. 3820-3828.

35. Jousse, D., *Transport properties of highly doped polycrystalline and amorphous films*. Physical Review B, 1985. **31**(8): p. 5335-5342.

36. Ibrahim, A. and S. Al-Ani, *Models of optical absorption in amorphous semiconductors at the absorption edge: a review and re-evaluation*. Czechoslovak Journal of Physics, 1994. **44**(8): p. 785-797.

37. Sanon, G., R. Rup, and A. Mansingh, *Band-gap narrowing and band-structure in degenerate tin oxide (SnO_2) films*. Physical Review B, 1991. **44**(11): p. 5672-5680.

38. Pajasová, L., *Optical properties of GeO_2 in the ultraviolet region*. Czechoslovak Journal of Physics, 1969. **19**(10): p. 1265-1270.

39. Arlinghaus, F.J., *Energy bands in stannic oxide (SnO_2)*. Journal of Physics and Chemistry of Solids, 1974. **35**(8): p. 931-935.

40. Joyce, W.B. and R.W. Dixon, *Analytic approximations for the Fermi energy of an ideal Fermi gas*. Applied Physics Letters, 1977. **31**(5): p. 354-356.